# Biophysical investigations of single cells with optically actuated microtools

## PhD Thesis

**Tamás Fekete**

**Biological Research Centre, Institute of Biophysics**

**Supervisor:**

**Dr. Lóránd Kelemen**

**Doctoral School of Multidisciplinary Medical Sciences**

**Szeged**

**2021**

## Publications related to the subject of the thesis:

**I.** **Tamás Fekete**, Mária Mészáros, Zsolt Szegletes, Gaszton Vizsnyiczai, László Zimányi, Mária A. Deli, Szilvia Veszelka, Lóránd Kelemen; Optically manipulated microtools to measure adhesion of the nanoparticle targeting ligand glutathione to endothelial cells; *ACS Applied Materials & Interfaces*; 13:39018-29, (2021); IF: 9.23

**II.** István Grexa, **Tamás Fekete**, Judit Molnár, Kinga Molnár, Gaszton Vizsnyiczai, Pál Ormos, Lóránd Kelemen; Single-Cell Elasticity Measurement with an optically Actuated Microrobot; *Micromachines*; 11(9) Paper 882 (2020); IF: 2.89

## Manuscripts not related to the thesis:

**I.** Gaszton Vizsnyiczai, András Búzás, Aekbote Badri Lakshmanrao, **Tamás Fekete**, István Grexa, Pál Ormos, Lóránd Kelemen; Multiview microscopy of single cells through microstructure-based indirect optical manipulation; *Biomedical Optics Express* 11(2): 945-962 (2020); IF: 3.73

**II.** Aekbote Badri Lakshmanrao, **Tamás Fekete**, Jacak Jaroslav, Gaszton Vizsnyiczai, Pál Ormos, Lóránd Kelemen**;** Surface-modified complex SU-8 microstructures for indirect optical manipulation of single cells**;** *Biomedical Optics Express* 7(1): 45-56 (2016); IF: 3.34

# Contents

# I.   Introduction

In order to target biological barriers such as the blood brain barrier (BBB) it is crucial to understand its behavior and its function. This cumbersome task would be easier if we had more knowledge about its physicochemical and mechanical properties. In my thesis I demonstrate the possibility to utilize optical tweezers-based (OT) micromanipulation techniques to obtain information on BBB constituent endothelial cells. For this, I introduce a new measurement technique that utilizes tailor-designed, task-specific microtools as probes, fabricated with two-photon polymerization (TPP) and actuated with optical tweezers as well as cells cultured on vertical surfaces. The use of microtools provides various advantages over simple trapped microbeads, for instance of preventing the cells from photodamage.

First, I demonstrated that the optically actuated microtools can help measure the Young's modulus as a physical characteristics of living hCMEC/D3 human brain endothelial cells with high precision. I have found that the OT-based method is especially suitable for measuring the elastic properties of the cell membrane without any viscous effects, and that the obtained Young's modulus values are highly comparable to those published in the literature.

Second, I investigated the binding efficiency of the highly effective nanoparticle targeting ligand glutathione onto the surface of endothelial cells with simple two-photon polymerized microstructures and I measured its adhesion force with more complex micromanipulator structures on live hCMEC/D3 cells and primary rat brain endothelial cells (RBEC). We validated our OT-based cell adhesion results with parallel AFM experiments.

In the following sections I introduce the materials and techniques I used throughout my work, such as the SU-8 photopolymer and the functionalization possibilities including our method, the optical tweezers, and the cells that we tested with the introduced methods.

# 1. SU-8 photopolymer

SU-8 (Microchem ltd.) is a negative tone photoactive polymer, which is biocompatible, chemically inert and has high refractive index and relatively high mechanical strength (the Young's moduli of SU-8 vary between 0.9 to 7.4 GPa (J. Gao, 2010)), what makes it ideal for optical trapping applications. The resist composed of 3 major ingredients: monomers, photoinitiator, these two are shown on *Figure 1.*, and solvent. The solvent component serves *(gamma-butyrolactone)*, as a thinner what makes easier to coat glasses, but it must be evaporated from the thin layer to make solidified SU-8 (this process called soft-bake). There are several series of SU-8 (e.g., SU-8 2000, 3000, 6000 series) the major difference between them is dry matter content.
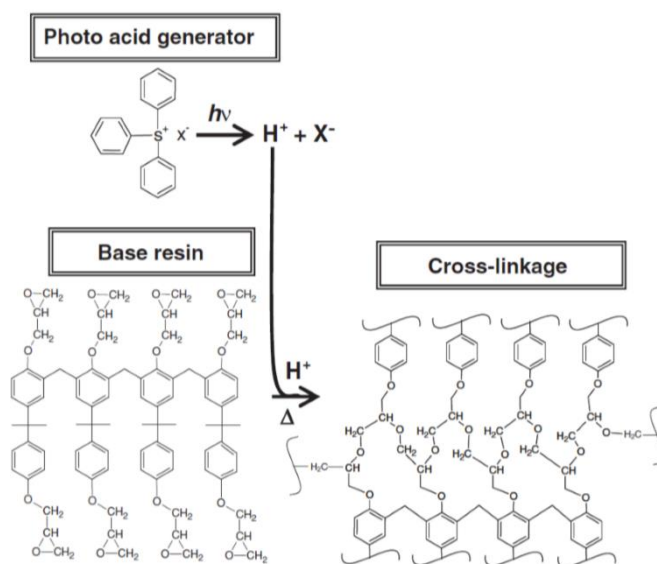


*Figure 1. Process of polymerization and the constituents of the SU-8 resin: photoinitiator (up), an SU-8 monomer (lower left), and the cross-linked polymer (lower right)*

An SU-8 monomer unit is composed of four *bisphenol-A* derivative scaffold, where one epoxy-ring is connected to each phenol ring. The SU-8's photoinitiator is *triarylsulfonium hexaflouroantimonic acid's* (*sodium*) salt, is containing a large number of delocalized electrons, thus has high photon-absorption capability. When it absorbs UV-photons it will turn the molecule to excited state which can form epoxonium-radicals from nearby monomer's epoxy groups in SU-8. The polymerization occurs only when a local threshold intensity (Teh, Dürig, Drechsler, Smith, & Güntherodt, 2005) is reached via the used light source, which can already activate the photoinitiators in that volume thereby creating monomer radicals. If the threshold intensity is not reached then the solute oxygen species in the photopolymer could deactivate the activated initiators through a process called oxygen scavenging (Kawata, Sun, Tanaka, & Takada, 2001); the same reaction could happen if the polymerization is too close to

air-SU-8 interface. If the intensity is enough to excite the photoiniciators, they can transfer their energy to form epoxonium-radicals. These radicals will start the photopolymerization-chain reaction when enough activation energy is available; this step would be realized in the thermal treatment called post exposure bake (PEB) after the illumination. The polymerization process ends when there is no more free polymer end or available monomers nearby. So, this reaction would only be accomplished at illuminated and baked areas. After the polymerization, all the unpolymerized SU-8 can be removed from around the polymerized structure; this step, called development, is carried out with *propylene glycol methyl ether acetate* (PGMEA) washing. Further information of SU-8 thin layer processing and development are in the protocol section (*protocol no. 4*).

## 2. SU-8 surface modification possibilities and applications

There are several possibilities to obtain modification of the surface of SU-8 either to tune its own physical characteristics (wettability, surface charge,) or to bind polymers, nanoparticles or even with proteins to it. Since SU-8 is highly inert in most applications an aggressive treatment has to be done to achieve covalent modification of its surface.

In the following section I present the modification methods most relevant for my work through applications and solutions found in the literature. Usually, the functionalization begins with an oxidative treatment to open the surface epoxy-rings. These could be oxygen plasma treatment (Tseng, Lin, Hsu, & Chieng, 2004); concentrated acid treatment or nitration compound (Lu, Wu, Peng, & Wu, 2008). If the epoxy ring is opened, a linker molecule can bind to it covalently. The linker's other, unanchored end can be tailored to the target molecule of interest to connect covalently. These covalent modifications can be applied in MEMs, in microfluidic systems or in optical tweezer measurements.

In the first example Tao and his coworkers demonstrated amine-groups can generated on SU-8 surface with *3-aminopropyltriethoxy silane* (APTES) treatment. As a first step they applied hot sulfuric acid to form hydroxide-groups on SU-8 which followed by the silanization ~APTES can bind to surface-OH groups (Tao, Popat, & Desai, 2006), thus an aminated surface were made. The importance of this research was that the authors showed the possibility of immobilization a variety of molecules: based on a wide spectrum of commercially available silane-compounds. Similar method was used in the following work, where the authors were able to immobilize antibody on SU-8 surface covalently (Joshi, Pinto, Rao, & Mukherji, 2007);

3

furthermore, silicon-based AFM cantilevers can be functionalized this way (Andrade, et al., 2020).

Not only silane compounds can be used as linker molecule but various *polyethylene glycol* (PEG) derivatives as well. In the following example the authors used hot sulfuric acid treatment, followed by PEGylation step. Here PEG-silicate (PEG-O-SiCl₃) was bond to SU-8, wherewith the SU-8's surface -OH-groups could react with it to form, O-Si-O bonds (Tao S. , Popat, Norman, & Desai, 2008). Similarly, to the silane compounds a very wide variety of PEG linkers are available as linker molecules: homo- or hetero-bifunctionalized ones or with more than two arms.

In the experiment of Yeh and co-workers, the main goal was to demonstrate that SU-8 can be combined with *dimethylpolysiloxane* (PDMS) to fabricate microfluidic channels; the ulterior is a material commonly used as structural element of microfluidic channels. In some cases, protein can bind to native SU-8 in a non-specific manner; to avoid this effect an appropriate surface treatment has to be done. As a first step, *3-aminopropyltrimethoxysilane* (APTMS) treatment was applied on the PDMS surface to achieve good adhesion between the SU-8 and PDMS elements of the microfluidic channel by adding primary amine-groups on the surface of PDMS. This step was crucial in order to create a closed microchannel system. Then, already inside the microfluidic channel, the authors applied *ethylene diamine* (EDA) treatment to create a confluent amine-functionalized layer on the SU-8 as well.  It was followed by a *mPEG-N-hydroxysuccinimide* (mPEG-NHS) immobilization with peptide bonds on both constructive layers of the channel. The authors showed that if the whole inside surfaces of the microchannel is PEGylated this way, the nonspecific adhesion of *bovine serum albumin* (BSA) can be decreased by ~60% relative to the case when PEG was not present on the surface (Yeh, Zhang, Lin, & Cao, 2012). In recent years, our laboratory has developed a number of methods for coating SU-8 surfaces, which have greatly expanded the possibilities of using SU-8 microdevices. I also became involved in this work, and I would present the main results of these works:

In almost all of our microstructure coating protocols we use nitration compound treatment to open the epoxy rings formed by *nitric acid* and *cerium ammonium nitrate* (CAN) as catalyst, instead of the other type of ring opening methods mentioned before. The reason for this is that our preliminary experiments showed that sulfuric acid treatment has a greater damaging effect on the fine, sub-micrometer sized details of SU-8 microstructures.

It is possible to immobilize gold nanoparticles (AuNP) to SU-8's surface with strong electrostatic interaction. The driving force of this reaction is that the AuNP's has a negatively charged surface that can bind to a positively charged surface generated by amino groups. To cover SU-8's surface with primary amines either 3-*Aminopropyl-triethoxysilane* (APTES) (Aekbote, et al., 2012) or PEG-*bisamine* can be used on preliminary CAN-treated samples. When a AuNP-covered microtool is positioned near to fluorescent streptavidin coated glass, the intensity of the fluorescence increased 6 times; this method enables the observation of weakly fluorescent signals difficult to image otherwise (Aekbote, Schubert, Ormos, & Kelemen, 2014).

Furthermore, our research group showed that it is possible to cover SU-8 surfaces with silver nanoparticles (AgNP) in a localized manner via photoreduction from *silver-nitrate* solution. For this, the substrate holding the SU-8 microtools was immersed into the silver nitrate solution where the focused beam of a 532 nm laser illuminated a well-localized part of each structure. The AgNP-coated part of the microtools, in combination with the surface-enhanced Raman scattering (SERS) technique, was used to detect ~µM concentrations of emodin molecules in an aqueous solution. Only when the Raman excitation laser were positioned onto an AgNP coated area, was the emodin spectrum clearly measurable, because of the presence of the plasmonic amplification (Vizsnyiczai, et al., 2015).

Our laboratory elaborated a method to immobilize whole living cells to SU-8 microtools for indirect optical micromanipulation (Aekbote, et al., 2016). Thus, the target cell could be held far away from the trapping beams with the proper design of the micromanipulator, which avoids the potential photodamage. To obtain a linkage between the cell and the manipulator, an adequate functionalization has to be made, which starts with opening the epoxy-rings with CAN-treatment, followed by a PEG-*bisamine* linker forming a peptide-bond between them. Afterwards a *sulfo-NHS-biotin* linker is bound to the PEG-linkers free amine group via amide-bond. This step makes it possible to anchor streptavidin (STA) as a final step of the microstructure functionalization protocol ([strept]avidin-biotin linkage is one of the strongest noncovalent bonds in nature ~200 pN/bond (Piramowicz, Czuba, Targosz, Burda, & Szymoński, 2006)) With this protocol the preliminary *sulfo-NHS-biotin* functionalized cell can be attached to a STA coated microstructure. The only drawback of this method; the cells must be treated with *sulfo-NHS-biotin* to obtain streptavidin-biotin linkage. In our micromanipulation article published in 2020, I modified this protocol to save the cells from the extra stress caused by the biotinylation (Vizsnyiczai, et al., 2020). This modification

was inspired by a method used in atomic-force microscopy (AFM) where the whole cells were attached to silica nitride cantilevers (Végh, et al., Adhesion and stress relaxation forces between melanoma and cerebral endothelial cells, 2012). As a last step, *biotinylated-ConcanavalinA* (bConA) was deposited on the STA coated SU-8 microstructures. ConA is a lectin what can bind *α-D-glucosyl/mannosyl* (Brewer, Brown, & Koenig, 1983) sugars which are present in eukaryote cell's glycocalyx. In both the streptavidin based and the ConA based applications the binding force between the cell and the micromanipulator is greater than the trapping forces achievable in our system, so the cell cannot be removed via optical forces from the SU-8 structures.

# 3. Two-photon-polymerization (TPP)

Lithography techniques were developed with the increasing need of fast PCB and microelectronic device fabrication. The key component of this method is a light sensitive photoresist which contains monomers and photoiniciators, which hardens if illuminated with UV-light, based on single-photon absorption (SPA) by the initiator. In mask lithography, a fine-detailed 2-dimensional light pattern can be transferred onto the photoresist-coated wafer (substrate) with a photomask which hardens the photopolymer within its overall thickness. There was a need to realize lithography in 3 dimensions, with lithography using SPA only relatively thin layer can be solidified precisely at once, which means that the structures have to be built up layer by layer similarly to the recently popular Fused Deposition Modeling (FDM) (Crump, 1989) or resin based stereolithography (SLA) (Kodama, 1981) type 3D printing techniques. To obtain complex fine-detailed photoresist microstructures in 3 dimensions, a two-photon polymerization technique was developed (TPP) (Cumpston, et al., 1997) which eliminates the aforementioned problems. The method is based on two photon-absorption (TPA) where two near infrared (NIR) photons are absorbed nearly at the same time to activate the photoiniciators in the illuminated volume. Thus, the NIR photons' wavelength should be twice as the linear excitation wavelength of the initiator, to provide similar amount of energy than one UV-photon. TPA requires the spatial and temporal focusing of the photons, therefore high NA objectives are used to focus the illuminating laser beams into a spot smaller than a micrometer, and at the same time only lasers operating in ultrashort-pulsed mode (pulse length ~ 100 fs) can provide high enough photon flux in each pulse for the simultaneous absorption in the focal spot. TPP eliminates the basic problem of SLA technique, since the polymer being only in the focal volume is polymerized during or after the illumination. The smallest

polymerizable unit is called voxel, which is usually shaped like an ellipsoid; the voxel typically has ~100 nm lateral and ~500 nm axial size. The simplest number to describe the voxel is its aspect ratio, which is the longitudinal length divided by the axial length; it typically has a 3-5:1 value (Sun, Tanaka, & Kawata, 2002). There are several possibilities to decrease the aspect ratio, thereby to increase the resolution along the optical axis, for instance with the use of higher numerical aperture objectives or with photoinhibition. In the latter case a special, so-called Laguerre-Gaussian beam is used for the depletion of the excited electronic state of the initiator together with the excitation beam to decrease the activated volume (Wollhofen, Katzmann, Hrelescu, Jacak, & Klar, 2013). Thus, there is a possibility to reach 1:1 aspect ratio. The feature size of the polymerized structures can be influenced by several process parameters, but for practical reason the exposure time and laser intensity are the most common ones to control the voxel's size. To fabricate 3 dimensional micro-objects, either the focal spot of the polymerizing beam can move relative to the stationary sample or vice versa like in the predecessor technique, the micro-SLA. The focal spot scanning can be realized with reflective (Obata, El-Tamer, Koch, Hinze, & Chichkov, 2013) or refractive (Vizsnyiczai, Kelemen, & Ormos, Holographic multi-focus 3D two-photon polymerization with real-time calculated holograms, 2014) optical elements. The 3D sample translation is carried out with piezo or air-bearing stages (Ricci, et al., 2017). It's worth noting that the technique of TPP became popular enough in the laser microfabrication field during the last decade that commercial systems can already be purchased (Nanoscribe GmbH).

Microstructures fabricated with TPP can be used in a wide spectrum of fields. The following are just a few examples: there is a possibility to use TPP made photopolymer structures for master replica molding (LaFratta, et al., 2004) or micro-Transfer Molding (µTM) (Busche, Starke, Knickmeier, & Dietzel, 2020) techniques. With these two techniques it is possible to reproduce a design for several tens of times via molding, therefore they are widely used for instance in the production of microfluidic systems. Furthermore, with TPP one can produce even moving microfluidic devices such as micron sized pumps (Maruo & Inoue, 2006), or bacteria powered micromotors (Vizsnyiczai, et al., 2017). In addition, periodically repetitive structures can be made via TPP, like photonic crystals (Haske, et al., 2007), but micro-electronical devices such as micro wires, resistors or inductivities (LaFratta, Fourkas, Baldacchini, & Farrer, 2007) can also be fabricated.

In *Figure 2.* additional examples, made with TPP are shown: part **a)** the structure is made of *polyethylene-glycol diacrylate* (PEGDA), which is a soft biocompatible polymer whereby

hydrogel cell-scaffolds can be made from it to form tissues from cell cultures (Accardo, et al., 2018); part **b)** shows a biomimetic device inspired by the blood-brain barrier (BBB), and it is possible to grow co-cultured cells both in and outside of the vessel-like structure (Marino, et al., 2018); part **c)** shows an innovative idea to polymerize soluble supports for delicate objects similar to the 3D printing fields so more complex objects can be prepared (Gross & Bertoldi, 2019).
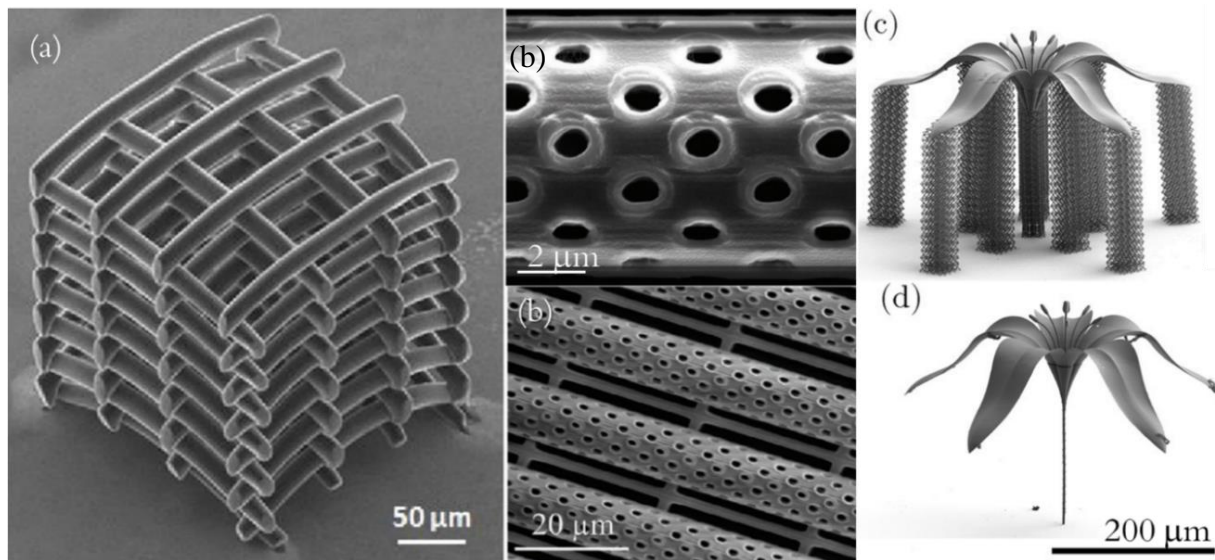


*Figure 2. Examples for two-photon polymerized microstructures. **a)** PEGDA tissue scaffold, **b)** micro vessel, as part of a biomimetic device, **c)** supported flower with soluble supports, **d)** developed flower without supports, a state-of-the-art example for multi-material TPP*

# 4. Optical Traps and applications

## A: Optical traps

If a laser beam is focused down with a high numerical aperture objective, small dielectric particles can be trapped in the focal spot. The first optical trap was developed by Arthur Ashkin (Ashkin, Dziedzic, Bjorkholm, & Chu, 1986), who observed that a few micrometer-sized particles, which have greater refractive index than the surrounding media and negligible absorption at the applied laser wavelength, can be immobilized by the focused laser beam. In midst of trapping, the object is held by the focal spot and stabilized by the sum of gradient and scattering forces. The gradient forces, that originate from the momentum change of the beam due to its refraction on the trapped object itself, are pushing the object towards the focal volume, whereas the scattering forces push the particle away from the focus due to the radiation pressure, usually parallel with the direction of the beam. In order to obtain solid trapping, the gradient forces must be grater then the scattering forces. As a result, the particle

is fixed in the trapping beam's focus with dampened Brownian fluctuation (K. C. Neuman, Optical Trapping, 2004). The force $F$, acting on the trapped object when moved out of the focus with $\Delta x$ is proportional to this displacement, with the coefficient called trap stiffness ($k$): $F = -k \cdot \Delta x$. In most of the cases, the optical force is larger for displacements perpendicular to the optical axis (lateral force) than along the optical axis (axial force).

Optical traps can be built in several different ways, the most common being the single beam trap, where the objective focuses only one beam. It is also possible to build a counter-propagating trap with two slightly divergent beams emerging from two opposing optical elements (fibers or objectives) (Guck, et al., 2005), where the lateral stabilization is due to the gradient forces and in the axial direction the counter-balancing scattering forces stabilize the object. Also, there are possibilities to generate multiple focal spots, for instance with a spatial light modulator (SLM) (Leonardo, Ianni, & Ruocco, 2007), digital light processors (DLP) (Palima, et al., 2012) or acusto-optical deflectors (AOD) (Brouhard, Schek, & Hunt, 2003). With these instruments the focal spot's position can be manipulated in two (DLP and AOD) or even all three dimensions (SLM). The SLM stands out in terms of flexibility from these pieces of equipment. The trapping method based on the SLM is called holographic optical tweezers, or HOT. In a HOT optical system, the SLM acts as a diffractive optical element, which can introduce phase shift to the trapping laser beam, similarly to a grating or a lens, but the SLM can do it in a reconfigurable way. Without going into details, the SLM can easily create multiple beams and it can steer or even focus them. In our HOT system we use an SLM which can change its refractive pattern (the hologram) with 60 Hz refresh rate and split the beam into dozens of foci via altering the hologram displayed on its reflective surface.

In all the above arrangements, it is crucial to know the optical traps stiffness in order to be able to measure optical forces. There are two popular techniques to measure them; one is based on the Brownian-fluctuation where the position of the trapped object is recorded preferably with a few nanometer precision, and the trap stiffness $k$ is calculated from the variance $<\Delta x^2>$ of the displacement from the equilibrium position: $\frac{1}{2} k_B \cdot T = \frac{1}{2} k \cdot <\Delta x^2>$, where $k_B$ is the Boltzmann constant and $T$ is the absolute temperature. The other is a Stokes drag-based method when a trapped object is moved in the surrounding medium with a stationary speed and the object displacement from the focus will be proportional with the drag force which exerted on the trapped object.

<u>B: Optical traps applications</u>

The optical traps have a broad range of application possibilities exploited in several disciplines, and numerous articles have been published about this method. In the following I introduce some that are relevant to the work described in my thesis.

The precision of positioning of the optically trapped object allows for position and force determination related to biological materials or processes at the nanometer and pico Newton levels. One of the most studied biological molecules is DNA: the stretch modulus of a single strand was measured to be 800 pN also the persistence length was determined by (Smith, Cui, & Bustamante, 1996). With a similar arrangement, where an actin filament was extended between two optically trapped beads and brought to the proximity of a myosin coated, bigger, surface-attached bead, the step size of myosin and their interaction forces were determined to be 11 nm and 3-4 pN respectively (Finer, Simmons, & Spudich, 1994). Even DNA motion-sequencing is possible with lower than resolution 4 Å (base pair distance in DNA); this was based on that the polymerase has distinguishable transcriptional position versus time behavior on the different nucleotides (Greenleaf & Block, 2006).

Especially relevant to my work is that of Phillips and co-workers, who showed that, with optically trapped complex microtools, it is possible to measure surface topology in 3 dimensions with ~100 nm resolution (Phillips, et al., 2012). The method was enabled with the precise measurement of the 3-dimensional position of the extended tool, carried out with a stereo-observation method. In the case of an extended microtool, the trap stiffness becomes a matrix instead of a single number, where the matrix elements describe the translational as well as the rotational stiffness of the trapped tool.

Trapping live cells has also been carried out with optical tweezers in the past for simple translocation purposes (Wang, et al., 2011) or to investigate cell-cell interactions (McNerney, Hübner, Chen, & Huser, 2010). From the point of view of direct cell trapping it is important, that water has relatively small absorption in the NIR region. Since biological samples consist high amount of water, in order to protect the cells from photodamage, usually NIR-emitting lasers are used. Since the trapping force is highly dependent on the refractive index difference between the trapped object and the surrounding solution, the direct trapping of cells of high-water content can be realized with only small trap stiffness. In order to achieve stiffer trapping, it can be useful to attach transparent intermedier objects, such as polymer beads to the cells, with much greater refractive index and trap them as handles for the cells (indirect trapping) (Lim, Dao, Suresh, Sow, & Chew, 2004). Our research group has extended the indirect cell

manipulation technique, when we used laser-microfabricated, functionalized micromanipulators as handles to actuate k562 cells (*Figure 3.*) in order to observe the 3D structure of its mitochondria with multiview microscopy. The manipulator consisted of two main functional parts: three spheres of about 4 μm diameter to be trapped by the focused laser beams, and a dish-like part to which the cell can be attached; it also consisted of rods connecting these parts. The manipulator served two major purposes: one was to manipulate the attached cell with 6 degrees of freedom (translation along 3 axes and rotation around 3 axes), and secondly, the shape of the tool prevented the cell from the possible photodamage during the measurement, keeping the trapping beams more than ten micrometers away from the probed cell (Vizsnyiczai, et al., 2020). *Figure 3.* shows the main steps of the cell manipulation for the multiview microscopy.
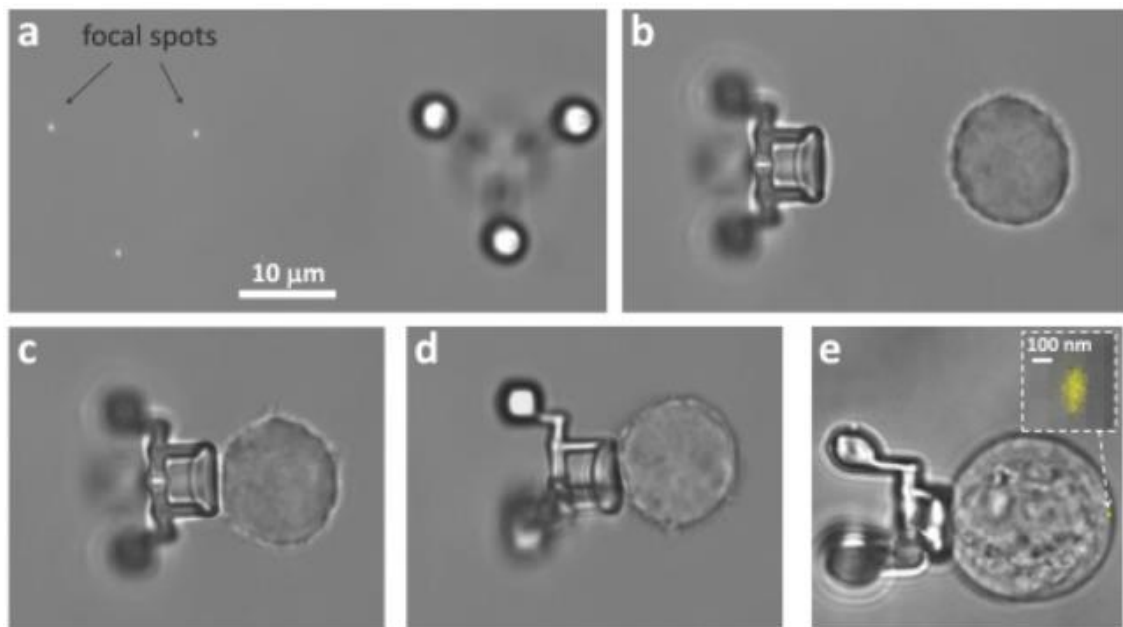


*Figure 3. Indirect cell manipulation with optically actuated microtools. The process of cell attachment to a microtool: (**a**) image of the three trapping foci and one untrapped microtool, (**b**) the microtool trapped and oriented with its disk towards the cell, and (**c**) the cell is attached to the microtool and elevated from the supporting glass surface. (**d**) The indirectly trapped cell is rotated by 90 degrees relative to its earlier orientation on panel c. (**e**) The insert shows the positional distribution of a given point on a fluctuating trapped cell.*

## 5. Measuring cells mechanical properties and membrane adhesion with AFM and OT

From diagnostic point of view, it can be important to better understand the cell's mechanical properties since the cellular activities/functions can be coupled, for example with the elasticity of the cell's membrane. The elasticity can provide information about the membrane composition or the cytoskeleton's structure. These properties, among others, could

be investigated with microprobes provided by atomic force microscopy (AFM) or optical traps. The AFM is capable of measuring forces from several ~pN up to the ~nN regime, while with optical traps the range is ~fN to several hundreds of pN; consequently, the two technique can complement to each other. The work of Nawaz and co-workers (*Figure 4.*) is quite unique, since they directly compared the two techniques with the observation of the rigidity of 3T3 mouse fibroblast cells (Nawaz, et al., 2012): in case of the AFM measurements, they attached a 2 μm diameter bead to AFM cantilever's end and pushed it against the cell and retracted, while recording the applied force and the indentation of the cell. With the optical tweezers they trapped an ~0.8 μm diameter bead and pushed to cell's surface and retracted, and the bead position was determined with a position sensing diode, thus the applied force could be calculated. Their AFM results showed that when grater forces are applied, a hysteresis-like difference is present between the indentation and the retraction curves. With AFM the maximal pushing force was almost 600 pN, while with optical tweezer just 10 pN. From their observations it was concluded that if the applied indentation force was small, then the Young's modulus, which determines the cell's stiffness, was around ~100 Pa, determined with both techniques (*Figure 4.*). In case of higher applied indentation forces or faster pushing speeds with AFM, the intracellular viscosity and the cytoskeletal rigidity are authoritative.
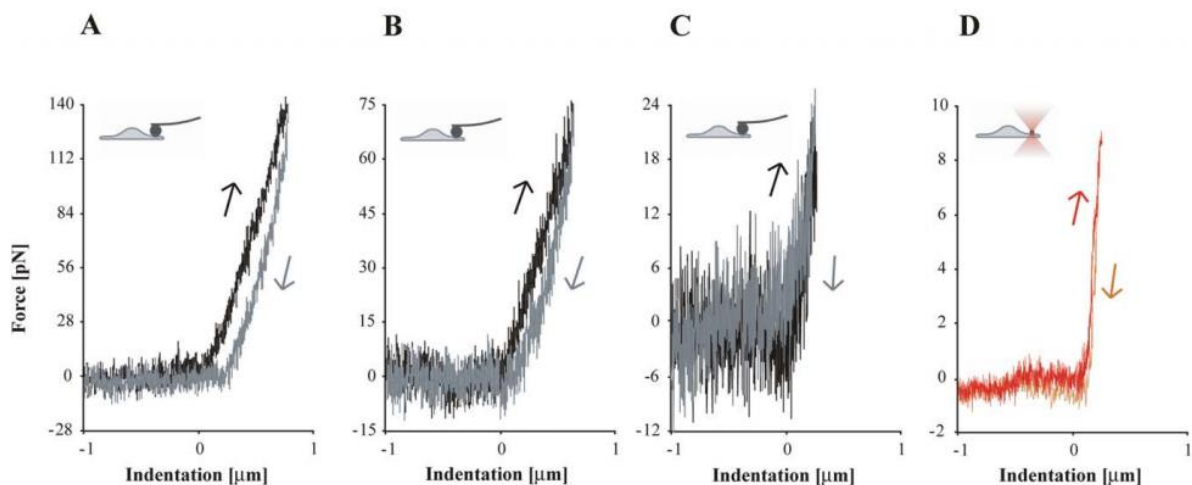


*Figure 4. Indentation force effect on cell stiffness measurement; AFM indentation (black) and retraction curves (grey); (**A**): the indentation force was limited to 140 pN; (**B**): indentation force was limited to 75 pN; (**C**): the applied force was minimalized to 25 pN; (**D**): optical measurement with less than 10 pN applied force, red curve is the indentation, and the orange cure is for the retraction. (Nawaz, et al., 2012)*

The adhesion of simple- or macromolecules or nanoparticles (NP) to the cell membrane can also be characterized with AFM or OT. For this, the AFM tip or the trapped object needs to be previously functionalized with these molecules or NPs (Lamprecht, Hinterdorfer, & Ebner, Applications of biosensing atomic force microscopy in monitoring drug and

nanoparticle delivery, 2014). Such measurements find especially interesting application in drug research, where the drug is encapsulated into NPs that are labeled with targeting molecules that facilitate the NP uptake by the cells. In the literature the binding force between the targeted NPs or ligands and the cell surface is observed in the regime of 20-60 pN (Oliveira, et al., 2011), (Gomes, et al., 2017). Again, OT can measure adhesion forces in a lower regime more reliably, as shown by Shergill and co-workers with cells expressing Delta-like1 receptors and beads covered with the ligand of this receptor and pushed against the cell membrane (Shergill, Meloty-Kapella, Musse, Weinmaster, & Botvinick, 2012).

As I detailed above, OT techniques can serve with valuable information about the cell membrane properties, either mechanical or biochemical. In the vast majority of these cases however, surface-adhered cells are measured with microbeads manipulated with the optical trap in the axial direction, because the apical membranes are perpendicular to the optical axis, since the cells are cultured on a adhesion promoter coated glass substrate (Nawaz, et al., 2012), (Vargas-Pinto, Gong, Vahabikashi, & Johnson, 2013). However, the optical forces are usually about a factor of 5 times minor in the axial direction relative to the ones in the lateral direction (K. C. Neuman, Optical Trapping, 2004). Partly to overcome this, and to avoid the illumination of the investigated, horizontal cell layer on the substrate with the trapping beam, we modified this arrangement by introducing vertical walls into the sample chamber and culture the cells on these walls. Our new experimental arrangement, which is in the center of my presented work, makes it possible to measure mechanical and adhesion forces on living cells still perpendicular to their membrane, but at the same time with the optically manipulated microtool moving perpendicular to the optical axes (Grexa, et al., 2020), (Fekete, et al., 2021). In both type of measurements, the technique allows us to exert greater optical force on the microtool and a more precise position determination.

## 6. Blood-brain barrier targeting

### A. Structure and function of blood-brain barrier

In our body one of the most important barrier protecting the central nervous system (CNS) is the blood-brain barrier (BBB), that helps to sustain the brain's microenvironment (Abbott N. , 2002), and keeps pathogens, toxic compounds out of the brain. BBB is one of the tightest barriers in the vascular system, formed by brain capillary endothelial cells which are connected

with junction proteins forming the tight junctions (TJ). TJ are closing tightly the paracellular gaps and linked to the actin cytoskeleton (Haseloff, Dithmer, Winkler, Wolburg, & Blasig, 2015). The BBB's endothelial cells are highly interacting with astrocytes and pericytes, via a shared basal lamina; this formation is called the BBB (*Figure 5/A.*). Only small lipophilic molecules such as sugars, nicotine, or blood gases can pass the BBB without carrier via transcellular lipid-mediated diffusion. In contrast, most polysaccharides, peptides, or proteins are blocked from CNS by the BBB; apart from the BBB, the negatively charged glycocalyx also participates in the exclusion of many molecules (Lockman, Koziara, Mumper, & Allen, 2004).
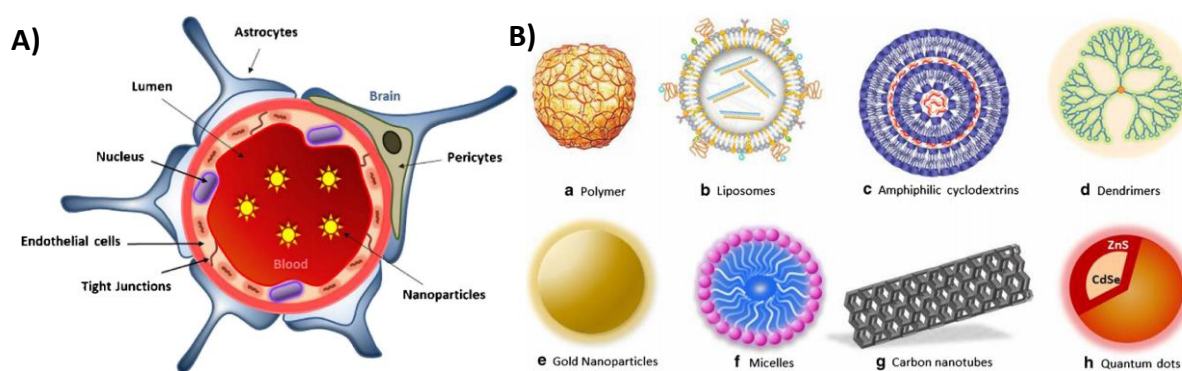


*Figure 5. (**A**) illustration of BBB, (**B**) several types of possible BBB targeting nanoparticles.*

The most important ways for naturally occurring molecules to pass through BBB with carriers are the following. Solute carriers (SLCs) are membrane coupled proteins (Tihanyi, et al., 2018), which can facilitate bi-directional transport of minerals and nutrients (exchangers or ion-coupled transporters) (Campos-Bedolla, Walter, Veszelka, & Deli, 2014). Also, there are co-transporters such as 2 $Na^+$ / hexose (glucose in most case) which can sustain gradient-dependent bidirectional transport (César-Razquin, et al., 2015). Vitamins, amino-acids, proteins can pass the BBB in ATP dependent ways via vesicular transcytosis, or receptor mediated endocytosis.

From therapeutic point of view, BBB means a burden for many drug molecules trying to reach the CNS, but there are three mayor ways to facilitate the transport of these molecules through BBB: modification of BBB's functions, circumvention of BBB, or modification and encapsulation of the drug molecules. For my thesis, the method of drug encapsulation with nanoparticles (NPs) is relevant, so in the next chapter I describe it shortly.

B. Approaches to target BBB

The field of nanomedicine can supply several types of NP shown in *Figure 5/B*. (Carthy, Malhotra, O'Mahony, Cryan, & O'Driscoll, 2015); these colloidal systems cover a very broad range both in terms of size (1-1000 nm) and composition. The NPs can carry imaging compounds as well as therapeutic agents; if they deliver both, they are called theranostics (Saraiva, et al., 2016). The most important required properties of these NPs are biocompatibility, and biodegradability, but they have to have the capability of loading with or coupling to hydrophilic or lipophilic molecules (Kreuter, 2014).

In terms of composition/formulation, NPs can be classified into two major types: a solid nanoparticle (SNPs) and vesicular NPs. Three of the most described solid NPs are made from gold, semiconductor nanocrystals (quantum-dots, QDs) and plastic. Gold NP-s have plasmonic-resonance, which feature makes them ideal for imaging, and at the same time, their surface can be easily conjugated with oligonucleotides or antibodies (Yeh, Creran, & Rotello, 2012). The QDs (<50 nm) can be separated into 3 groups based on composition: core-type, shell-type, and alloyed core-shell-type. They are ideally used as fluorescent labels, based on their great photostability, and broad absorption spectra (Probst, Zrazhevskiy, Bagalkot, & Gao, 2013). QDs are often used for visualizing cellular uptake in real time. On the other hand, the applications are controversial because, in most of the cases those are composed of toxic heavy metals (Te, Cd, Zn, As) (Lim, Shen, & Gao, 2015). A great variety of biocompatible plastics are used to form NPs, such as *polystyrene* (PS) (Loos, et al., 2014), *polylactic acid* (PLA), *polylactic-co-glycolic acid* (PLGA), or even gelatin; the latter three are also biodegradable. These polymers can be mixed with therapeutics or imaging compounds to form a polymer matrix.

One of the most studied NPs are the lipid-based vesicular ones. Their biggest advantage is that they can deliver hydrophilic molecules in an aqueous core, and lipophilic ones in their membranes, what can be uni-, bi- or multilamellar. The composition and size can vary a lot between hundreds of nanometers (Bragagni, Mennini, Ghelardini, & Mura, 2012), (Woods, et al., 2020), In most cases they contain *cholesterol* because sterol derivatives are stabilizing the integrity of the membrane (Masserini, 2013). Another important type of vesicular NPs are made from non-ionic surfactants, and named niosomes. They are more stable than the conventional lipid vesicles, also keeping their advantages even, the production is cheaper (Gharbavi, Amani, Kheiri-Manjili, Danafar, & Sharafi, 2018). This uni or multilamellar niosomes are usually

made from fatty acid ester or ethers such as Span or Tween (Abdelkader, Alani, & Alany, 2014).

Our collaborator used alanine, glucopyranose and glutathione mono/bi-functionalized niosomes to increase their uptake for them in BBB (Mészáros, et al., 2018). They encapsulated Evans-blue coupled albumin (EBA) in their inside hydrophilic cavity to visualize their permeability on BBB model via fluorescent microscopy. The glucopyranose and alanine decorated one's uptake could be facilitated via SLC transporters GLUT1 (SLC2A) and SLC38A/SLC1A, the latter one can also transport other neutral amino acids like serin and cysteine. Unfortunately, the GSH's carrier didn't discovered yet, but the two abovementioned transporter families could facilitate the uptake (SLC38A/SLC1A), in addition GSH contains a glutamate part which has also dedicated transporters. The main goal was to demonstrate that all the three targeting ligands increase the mono-functionalized niosomes uptake, nevertheless the combination of those ligands could increase further the engulfed EBA's permeability.

# II.    Aims of my study

In my thesis I demonstrate the possibility to utilize optical tweezers-based (OT) micromanipulation techniques to obtain information on BBB constituent endothelial cells. For this, I rely on tailor-designed, task-specific microtools as probes, which I fabricated with two-photon polymerization (TPP) and actuated with the optical tweezers.

1. First, I measure the Young's modulus of living human cerebral microvascular endothelial cells (hCMEC/D3) with high precision and examine that the OT-based results are comparable to those published in the literature.
   - Designing a task-specific microtool for cell indentation experiments
   - Creating an arrangement for the measurements where the cells located on a vertical wall
   - Determination the Young's moduli for hCMEC/D3 cells with our new OT-based measurement method using optically actuated microtools

2. Second, I investigate the highly effective nanoparticle targeting ligand glutathione adhesion force onto the surface of living endothelial cells
   - Creation of an effective PEG-meditated functionalization protocol to immobilize GSH on SU-8 surfaces
   - Determination of the GSH coverage with fluorescent microscopy
   - Characterization of binding probability of GSH-functionalized, optically trapped microstructures to four different types of cells
   - Measuring adhesion forces of GSH-covered SU-8 surface towards endothelial cells via our new OT-based method

# III. Materials and methods

## 1. SU-8 structures and TPP

### A: Preparation of SU-8 thin layers

I used thin SU-8 layers to fabricate SU-8 structures, both with UV mask lithography and two-photon polymerization where the thickness of the prepared SU-8 layer depends on the structure's height. In all cases, first I cleaned 24x40 mm soda-lime glass coverslips (Type 1#, Techlab France ltd.) which acted as a substrate for the microstructures. The choice of the type of the glass was important in order to obtain a good adhesion between the fabricated objects and the substrate. I cleaned the coverslips with a two-step procedure: first, $Cr_2O_{12}{}^{2-}$ *-ion* treatment was applied, to remove most of the oxidable contaminations; then, an *aqua-regia* bath was used which cleans all remaining contaminations and etch the surface of the glass which improves the adhesion of the polymerized microstructures (Wilmad-LabGlass, 2008). Next, I baked the substrates for 10 minutes at 110 C° to remove the surface adhered water molecules. This step was followed by the spin-coating of the substrate with SU-8 (for details see *Protocol 4.*). After the coating, a pre-exposure bake is applied, which removes the solvent from the resin. After this step, the SU-8 layer was illuminated either with UV light or with the ultrafast laser, as described below.

### B: Preparation of cell-growing SU-8 walls

In order to grow cells vertically for our side-approached optical micromanipulation method mentioned in the Introduction, I used a supporting wall for both the cell stiffness and the adhesion force measurements. I prepared approximately 100 μm tall, 50 μm, wide and 10 mm long SU-8 walls with UV mask lithography on the center of a circular, 24 mm diameter cover slip out of SU-8, formulation 2075 resin. The illumination was carried out through a chromium mask with the transparent region same as the size of the required wall size using a photolithography flood exposure source (λ=365 nm, dose: 5000 mJ/cm², model 97435, Newport, USA). After illumination, a two-step post-exposure bake (PEB) was used in order to reduce the development of thermally-induced stress inside the long walls: the sample was heat-treated on a hot plate for 10 minutes at 70 °C followed by another 10 minutes at 105 °C; after baking, the substrates were allowed to cool to room temperature naturally on top of the

hotplate to further reduce the chance of stress development. Finally, the walls were developed with a 2 times 5 minutes bath in PGMEA, washed with ethanol thoroughly and were eventually dried with a nitrogen blow.

After developing, these coverslips were bond to the bottoms of Petri dishes with Norland 68 optical glue (NOA68, Thorlabs Inc. USA); the dishes were previously drilled to have an approximately 20 mm opening in their centers. Also, I glued a 10 mm inner diameter and 10 mm tall acrylic tube insert around the SU-8 cell growing walls before adding the cells to decrease the final volume of the culturing media. During the adhesion force experiments it also helped the micromanipulators to stay nearby the cells. We had to prepare each Petri dish in the according to the abovementioned protocol, because of the PGMEA, the developer of the SU-8 attacked the *polystyrene* (PS) material of the commercially available glass bottomed Petri dishes. Until usage of the dishes those were kept in 70 % ethanol.

In case of stiffness measurements, similarly made smaller cell-growing walls were erected and used, the main difference was the size of those: 5 mm long and 100 µm respectively.

## C: SU-8 microstructures for optical tweezers measurements:

All the following microstructures were made into an approximately 20 µm thin SU-8 (formulation 2007) layer with our TPP system described in the next chapter. The post process of the TPP made microstructures detailed in the protocol section (*protocol 4.*).

To prove that GSH can be bond covalently onto an SU-8 surface, I polymerized two different types of test blocks: the small type was 25 by 25 by 5 µm without frame, the other type was 60 by 60 by 5 µm with additional 5 µm tall frames. The first kind was used for the fluorescent microscopy measurements, the framed one was designed for confocal imaging. The frames on the second type served to distinguish the bottom and the top surface of the structure in confocal microscope and provided extra mechanical stability. The disadvantage of fabricating these microstructures with TPP is that it is a much slower process than mask-lithography, but it would provide a much more homogenous surface (Aekbote, et al., 2012). These test blocks were functionalized with GSH using the same protocol as either the ellipsoid or the micromanipulators (detailed in *chapter 2*). After the GSH layer, an extra fluorescent dye is linked to it that refers to the amount of GSH attached to the surface.

To obtain the binding probability in the preliminary GSH-driven adhesion experiments, I polymerized simple SU-8 ellipsoids (short axis 2 μm and long axis 10 μm) and functionalized them with only the PEG linker and with GSH. These ellipsoids were trapped individually and moved over the cell layers with the optical tweezers. I measured the number of binding and non-binding events of the functionalized ellipsoids on four different cell types (primary rat brain astrocyte, pericyte, endothelial cell, and human hCMEC/D3 cell line cells).

For the cell stiffness and binding-force measurements, I prepared very similar microtools that were different only in their probe parts. These purpose designed micromanipulators had two main functional parts: the first, consisted of 4 spheres, each for being trapped by one of four optical traps; the spheres were arranged on a 14 μm side length square's corner points. The spheres were connected to each other with holder rods forming an X-shape, to minimize interference with the optical fields. The rods were made with a small offset between the plane of the spheres and the probe's plane. The force measurement relies on the precise determination of the structure's position, which is determined from the position of the spheres. This offset provides in the video recordings of the experiments, that the connecting rods were always out of focus, allowing a more precise position determination for the spheres which were always kept in focus.
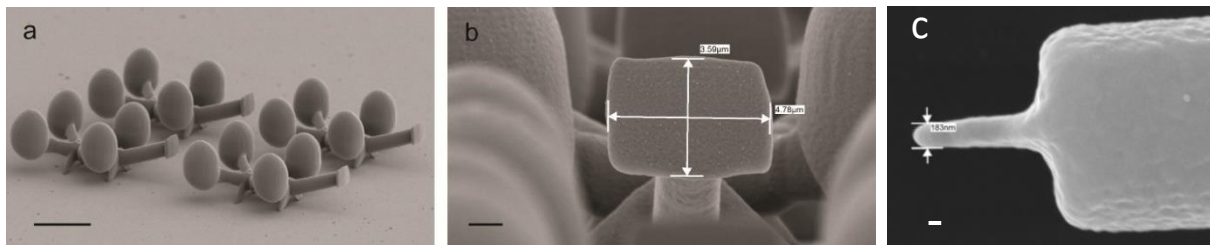


*Figure 6. Scanning electron microscopy images of the micromanipulators. (**a**) View of four individual micromanipulators used for the adhesion force measurements; scalebar: 10 μm. (**b**) Parameters/Dimensions of the contact surface of the structures shown in panel a. scalebar: 1 μm. (**c**) Pointy ended microtool's tip used for cell stiffness measurement; scalebar: 100 nm*

The second functional part was the probe of the microtools which had a different shape for the cell stiffness and for the adhesion force experiments. For the cell stiffness measurements microtool was equipped with a probe forming a pointy tip (Grexa, et al., 2020) showed on *Figure 6/c*. For the adhesion-force measurements the probe part provided the contact area between the cells and the tool in the form of a flat sheet perpendicular to the manipulators's frame, having an ~15 μm$^2$ surface area as shown on *Figure 6/b*. (Fekete, et al., 2021). The trapped spheres of both type of the micromanipulators were more than ten micrometers away from the probe part of the microtool, which ensured that the optical field did not cause photodamage to the investigated cells even if it was scattered on the spheres.

## D: Our TPP system

The most essential part of our TPP system (*Figure 7.*) is an ultrashort-pulsed laser (C-Fiber A, Menlo Systems, Germany, $\lambda = 795$ nm, 100 fs pulse length, 100 MHz repetition rate). The beam of the laser is directed onto a Spatial-Light-Modulator (Holoeye, Pluto NIR-II), which is capable to generate several focal spots, so increasing the production rate of fabrication. Afterwards, the beams were focused into an ~20 μm thick SU-8 layer supported by a 24*40 mm coverslip (type #1, soda-lime glass, RS-France) with a focusing objective (100X Zeiss Achroplan, oil immersion, NA 1.25). The precise 3D movement of the sample is guaranteed with a piezo-electric stage (Physik Instrumente GmbH, Germany) which provides us 300 by 300 μm polymerization field and nanometric translation precision. When the piezo stage's field was filled with the structures a motorized stage moved the sample in the lateral direction (L-step, Marzhauser Wetzlar Gmbh. Germany) to polymerize in another adjacent 300 by 300 μm field. To set the needed polymerization laser intensity we used a polarization beam splitter cube coupled with a half-wave plate (Thorlabs Inc., USA). A mechanical shutter (VS14S2ZM1, Vincent Associates, USA) was used to let the laser beam onto the sample when required. The piezo and motorized stages and the shutter were controlled by a computer through a home-made software written in Labview environment. The coordinate points of the structures to be polymerized were read by the program and it directed the piezo stage through these points during the illumination of the sample by the focused laser beam, opening and closing the shutter at pre-defined positions.
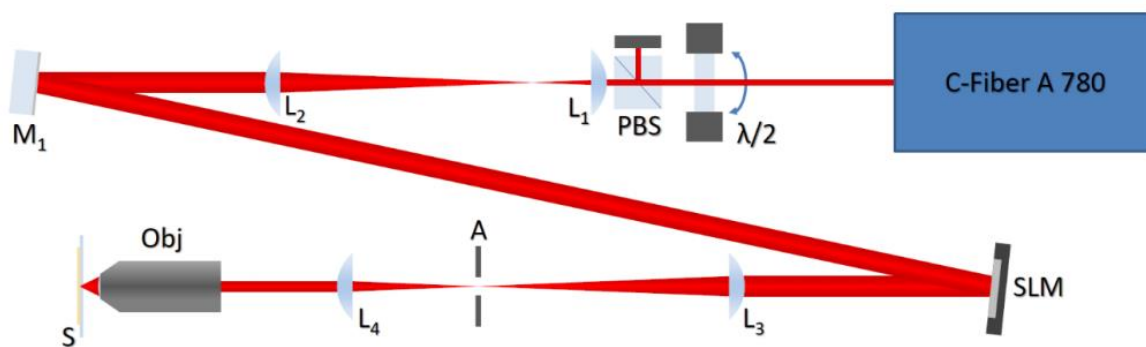


*Figure 7. Schematic of our TPP system*

# 2. Functionalization of microstructures

## A: GSH functionalization of SU-8

In order to measure binding force between the cells and the optically manipulated structures, I had to functionalize the TPP fabricated objects with the ligand of interest, glutathione (GSH) (*Figure 8.*). First, I show how the GSH can be linked on the SU-8 surface covalently according to *Protocol 1*. (See Appendix). First the surface epoxy-rings were opened, for what I used a nitration mixture (Lu, Wu, Peng, & Wu, 2008) which is made of *Ammonium-cerium(IV)-nitrate* (CAN, Sigma-Aldrich Kft.) and *nitric acid* (Molar chemicals Kft.) (**acid-treated** sample). This treatment leaves β-nitrato-alcohols on the surface, what turns into activated carboxyl-groups when $NO_2$ dissociates from the group (**Step I.**). In the following step, we react the carboxyl on the SU-8 with the free primary amine-groups of the amino-PEG-maleimide (MW = 2000, Nanosoft polymers ltd.) linker to form pseudo-peptide bond (**Step II.**) (Yeh, Zhang, Lin, & Cao, 2012). I chose this specific linker because of the experiments testing of the uptake of targeted NPs on endothelial cells ~our collaborator used DSPE-PEG-maleimide to bind GSH to the NPs. In my experiments the PEG-maleimide part was similar as to theirs (Mészáros, et al., 2018) and furthermore, that length of PEG-linker had particularly low affinity to bind biomolecules nonspecifically (Prime & Whitesides, 1993). The surface
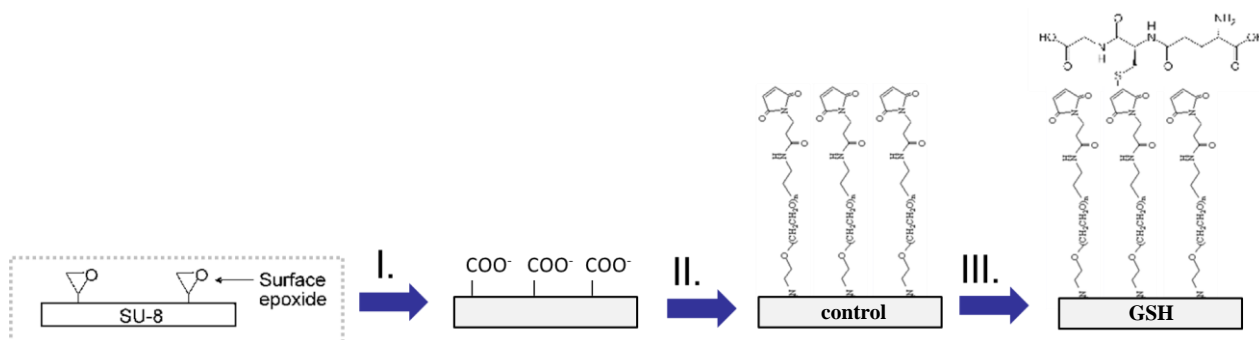


*Figure 8. Significant steps of GSH functionalization protocol*

treated until this step was later used as one of the **controls,** and we refer to it as a **PEGylated** surface. Another, positive control for GSH binding was prepared with PEG-bisamine instead of amine-PEG-maleimide. In this case, in **Step II.**, the sample was incubated with PEG-bisamine (cat. no. 753084, Sigma) to produce amine groups on the surface, onto which the amine-reactive dye (see below) can bind (**PEG-bisamine** treated sample). To cover the surface of PEGylated sample with GSH I simply used a slight alkaline (7.4 pH) PBS solution of 100

mM GSH; the thiol-group of this ligand molecule reacts with the maleimide part of the linker to form oxime-ether connection (**PEG-GSH** sample) (Martínez-Jothar, et al., 2018) (**Step III.**).

To visualize the presence and to quantify the coverage of GSH on SU-8 surface I used the amine-reactive fluorescent CY-5-ester dye (Cyanine5 NHS ester, cat. no. ab146454, Abcam) what had bound to the primary amine of the GSH molecule. The CY-5 staining was carried out after all three functionalization steps on the TPP-made blocks, as well as on the PEG-bisamine-coated sample and were observed with a Nikon (Eclipse Ti, Japan) wide-field fluorescent and an Olympus (Fluoview FV 1000, Japan) confocal microscope. This staining step was carried out as described in *Protocol 2*. (see Appendix).

## B: determination of SU-8 surface coverage of GSH

The measurement of the GSH surface coverage on the SU-8 blocks was based on the comparison of the integrated intensity of a single CY-5 dye molecule and of the uniformly fluorescent CY-5 layer formed on the GSH which is covering the SU-8 surface. As a first step, we imaged single CY-5 molecule by dropping 1.5 μL of very dilute, 1 ng/mL aqueous solution of the dye onto an ethanol cleaned cover slide and covered with another slide. With this method the dye molecules were separated enough on the bottom glass to image them individually. Both these single fluorophores and those covered uniformly functionalized SU-8 surfaces were imaged with wide-field fluorescent microscopy. The setup used the same illumination and observation conditions: as a light source a metal halide lamp (Lumen 200S, Prior Scientific, Inc., USA) was used with a CY-5 filter set (cat. no. 49006, Chroma Technol. Corp.), and we made the recordings with a CMOS camera (ORCA-Flash4.0 V3, type num.: C13440-20CU, Hamamatsu Corp., Japan). The number of fluorescent molecules over a unit area was determined by dividing the integrated intensity of the uniformly fluorescent layer over the unit area with the single CY-5 dye's integrated intensity. The measured intensity over the PEGylated surfaces were used as a background, and it was subtracted from the intensity of the GSH coated layers. Supposing that every GSH molecule binds a fluorescent dye molecule, the amount of the corrected sum intensity of the CY-5 yields the surface coverage of GSH. The z-stacked confocal imaging of the CY-5-stained blocks revealed that it is indeed only the top layer of the blocks that became fluorescent, therefore the wide-field fluorescent intensity, used for the quantification originates only from this single layer.

For the fluorescent images made just to visualize GSH presence on top of SU-8, and to prove the immobilization was most likely covalent: I used 10% intensity of the mercury-vapor lamp without any OD filters, in combination with an CY-5 dichroic cube. For exposure time I used 100 μs on the Qimiging camera with 3800 EM gain. In case of the confocal image sets they were excited with $\lambda = 650$ nm fiber laser at 15% intensity.

# 3. Cell cultures

In all experiments, we used cells which are composing the blood-brain barrier: primary rat brain astroglia, pericyte, and endothelial cells, as well as cultured hCMEC/D3 cell-line's cells. To help cell adhesion to the SU-8 walls and the glass substrate, we tried several adhesion promoters such as: Matrigel (Sigma ltd.) which is secreted by Engelbreth-Holm-Swarm (EHS) mouse sarcoma cells, rat tail collagen and *poly-L-lysin* (Sigma ltd.); the first two had an advantage of containing growth factors which help the cells to reach a confluent layer faster (Vukicevic, et al., 1992). The choice of adhesion promoters had no effect on the cell adhesion to the SU-8 walls. In the following, I shortly review the applied cells:

<u>**hCMEC/D3:**</u> human cerebral microvascular endothelial cell line, which was originated from cerebral micro vessel endothelial cells by transduction of lentiviral vectors; it is one of the most commonly used cells to study BBB's behavior. Morphologically these cells show a lot of similarities with primary endothelial cultures: they are spool-shaped, elongated, and when a confluent layer is formed, contact inhibition takes place. These cells also express proteins which are representative for brain endothelial cells such as: tight and adherence junction proteins, ABC transporters (Weksler, et al., 2005).

<u>**RBEC:**</u> primary rat brain endothelial cells; they are not immortalized as hCMEC/D3 cells but always need to be freshly isolated from the animals. These cells are also often used as model cells. Several types of techniques can be tested with them, such as monolayer uptake for pharmacons or well plate with inserts for co-culturing with other neuronal cells, to improve their biomimicking of BBB. They are isomorphic with hCMEC/D3 cells, the only difference is that they have an orderly rhomboid shape, when reach total confluency. In a confluent layer they express junctional proteins, ATP-binding cassettes (ABC) and solute carrier (SLC) transporters.

We used also primary rat **pericytes** and **astrocytes** for the ellipsoid binding experiment, to prove that our functionalization protocol can be used on more type of cells, but in the adhesion

24

force experiments these cells were not used. The main reason for this is that they do not form a flat cell layer but tend to grow in 3D, which made the adhesion experiments extremely hard to execute. It was almost impossible to approach those cells through this 3D structure with a trapped micromanipulator since, the time window was quite narrow before the cells started engulfing our GSH-coated manipulators or started to exfoliate from the SU-8 walls surface.

# 4. Holographic optical tweezer

For the cell stiffness measurement as well as for the binding and adhesion force experiments, I used our Holographic optical tweezer (HOT) setup shown on *Figure 9*. In the binding probability experiments with ellipsoids, I was using just one focal spot, but for the adhesion force and the cell stiffness measurements I had to create 4 focal spots for the microtool, what could be manipulated with high precision and accuracy. The focal spots, that trap the manipulators' spheres are generated similarly as in our TPP system, with a similar SLM (Holoeye, Pluto NIR-II). The HOT system is built around a Nikon (Eclipse TI) inverted fluorescent microscope with a continuous-wave infrared laser as light source ($\lambda$=1070 nm, THFL-1P400-COL50, BKtel Photonics). In the microscope I used an Olympus water immersion objective (UPlanSApo 60X, NA=1.2) as a focusing element and a motorized stage which provided the translation of the sample (ProScan, Prior Sci., U.K). The total amount of laser intensity at the entrance of the objective pupil was 270 mW which, considering the approximately ~50% transmittance of the objective at 1070 nm, resulted in ~34 mW power for each optical trap. The images of the micromanipulators were obtained with an EMCCD camera (Rolera EMC2, Qimaging, Canada). Moreover, a home-made sample holder was used with a PID-controlled heater element to guarantee the 37 °C for the cells under the measurements.
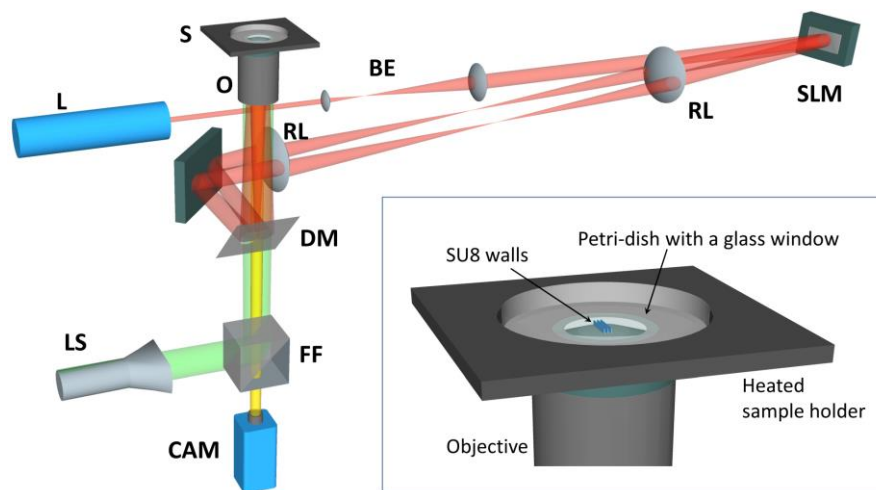


*Figure 9. Schematic of our HOT system and the heated sample holder*

# 5. Optical trap-based measurements

## A: Stiffness calibration of the micromanipulators

For the calculation of the cells' Young's modulus the force that the microtool exerts on the cells surface creating an indentation must be known. Similarly, in the case of the cell membrane-GSH adhesion measurements, the force the tool exerts at the moment of its detachment from the cell has to be determined. The force in both cases is calculated from the microtool's displacement from the equilibrium position multiplied by the trap stiffness. The
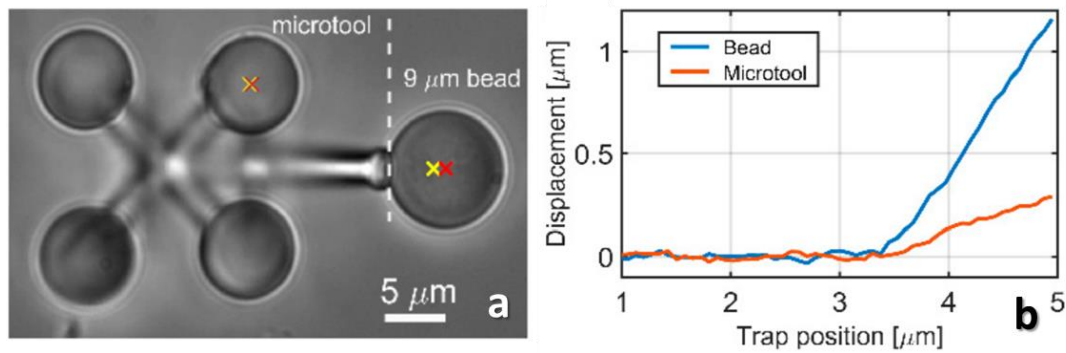


*Figure 10. Trap stiffness calibration for the cell indenter microtool. Panel (**a**) shows the optical microscopic image of the tool (left) and the 9 μm bead (right) during the calibration experiment. The yellow crosses show the positions of two optical traps, one holding one of the spheroids of the microtool, the other holding the 9 μm bead. The red crosses show the center of one of the spheroids on the microtool and that of the bead. The distance between the crosses gives the displacement values plotted on (**b**). In case of the adhesion force-measuring microtool, the arrangement was the same, but a 6 μm bead was used.*

trap stiffness $k_{str}$ for the microtools was determined by an indirect method, where the microtool was pushed against a 9 µm polystyrene bead (cell indentation microtool) or a 6 µm bead (adhesion force-measuring microtool) which has a known stiffness ($k_{bead}$), and the displacement of the microtool was compared to that of the bead (*Figure 10.*). At first, the $k_{bead}$ was measured by holding a bead alone in an optical trap and using the following equation:

$$\frac{1}{2}k_B T = \frac{1}{2}k_{bead}\langle x^2 \rangle; \qquad \text{eq. 1.}$$

where the $\langle x^2 \rangle$ is the variance of the bead's fluctuation measured by video tracking (exposure time: 0.5 ms), $k_B$ is the Boltzmann constant (K. C. Neuman, Optical Trapping, 2004) and T=295 °K. By pushing the tool against the trapped bead with 50 nm steps, $k_{str}$ was calculated from the measured displacements ($\Delta X_{bead}$ and $\Delta X_{str}$) with the following equation:

$$k_{bead} * \Delta X_{bead} = k_{str} * \Delta X_{str}. \qquad \text{eq. 2.}$$

For this measurement we used a flat ended microtool instead of a sharp tipped one, but this slight modification of the probe part did not affect the trap stiffness values determined by the trapping spheres' geometry.

Based on the equation 1., the stiffness values of the beads are: $k_{bead9\mu m}$ = 4.5 pN/µm and for the smaller one $k_{bead6\mu m}$ = 4.9 pN/µm. The trap stiffness of the indentation experiment's microtool was 16.49±2 pN/µm and that of the adhesion force measurements was 25.8±2 pN/µm. The deviation between the two kinds of manipulator stiffnesses originates from the slightly different diameter of the trapping spheres of the two manipulators.

## B: Cell indentation experiments

In these experiments I used only hCMEC/D3 cells that were grown on the SU-8 walls, and the microtools approached the cells in a perpendicular direction. *Figure 11.* depicts the sample arrangement and the microtool alignment procedure. As a first step, the microtools were collected with a pipette from their cover slide (whereat they were polymerized) and placed into the well containing the cells (Step 1). In the well, the hCMEC/D3 cells were immersed in ~200
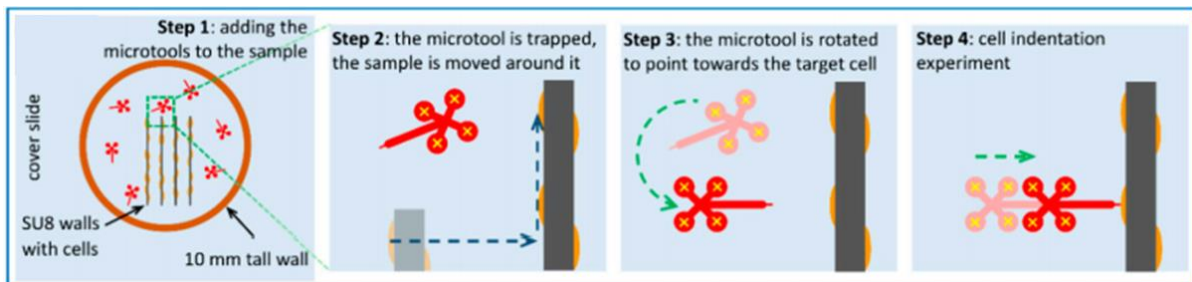


*Figure 11. Schematic of the indentation experiment: Microtools being pipetted into the sample well (Step 1) their alignment towards the target cell; yellow crosses mark the trapping beams positions, blue arrows indicate sample stage translations (Step 2) and green arrows the optical trap actuations (Step 3-4)*

µL of Leibovitz's L-15 medium (Sigma Kft.) which helped them being vital without $CO_2$ incubation for about 2 hours. At this point, the microtools were randomly scattered nearby the supporting walls. An individual tool was trapped with the optical tweezer and elevated from the horizontal glass substrate by about ~10 µm moving the trapping microscope objective. At this height the trapping foci would not be distorted by the presence of the wall when it is approached by the microtool. Then, the microtools were aligned in such a way that the plane of their four spheres were perpendicular to the optical axis, and with stationary optical traps the sample stage was moved to approximate a cell to about 1-2 µm (Step 2). Then with a fixed stage the microtool was turned towards the target cell by rotating the optical traps, until the tool's tip pointed towards the supporting wall (Step 3). At this point, a fine tuning of the tool's

position was executed: the cell's silhouette was brought into focus together with the manipulator's tip by moving the focusing objective. At Step 4 the indentation experiment was performed by moving the held structure with only the HOT by an average speed of 0.05 µm/s and with 10 nm steps toward the cells, and in every step a bright field image of the manipulator was recorded. Before the tool's tip made a contact with the cell or the wall (in the control experiments), the position of the microtool's spheres and that of the optical traps were coincided, but when the tip reached the target, the movement of the trapping beams continued for about another 1 µm and the tool's position was retarded relative to them.

To determine the cells' Young's modulus, the force that pushes the microtool to the target cell and the cell's indentation need to be measured; for both values, the tool's position has to be determined precisely. The force was calculated from the displacement of the microtool relative to the trapping foci. The indentation was determined from the difference of the microtools' position when they were pushed against the cells and against an uncovered SU-8 wall. The difference in the movements in these two instances provided the indentation value as described later (*Results and discussion chapter 1.*).

## C: Adhesion force measurements

The cells we used for binding force measurement were also grown on a wall-like scaffold similar to that in the previous experiment; in this case, however, we used two types of cells. The procedure of the experiment is described below (its main stages are shown in *Figure 12.*). As a first step, the micromanipulators were collected and placed in the petri dish which already contained the cells in growth media with 1% PDS (plasma derived serum). After the
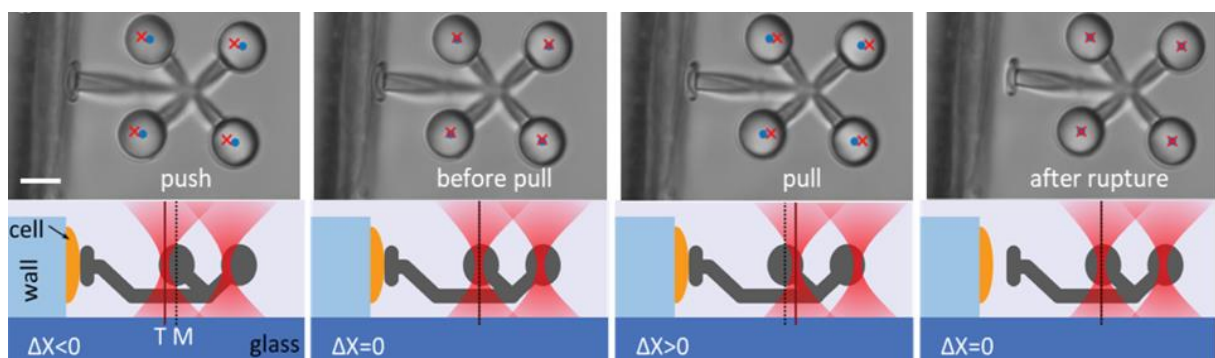


*Figure 12. Image sequence from a record of a typical adhesion experiment (the retraction process). The red crosses show the trap positions, and the blue dots mark the centers of the micromanipulator's spherical handles; scale bar: 5µm. Below each image a corresponding schematic side view drawing shows the relative positions of the trapping beam and the manipulator. The dark red line shows trap position (T), the black dotted line that of the manipulator sphere's center (M).*

manipulator's contact surface was aligned with the cell, the same way as in *Figure 11*. Steps 1-3, it started approaching the cell with 100 nm steps.

When it touched the cell, which was determined visually from the weak reflection of the trapping beams, the manipulator was pushed further against it by less than a micrometer. We paid attention to push the manipulator to the cell's surface with about a few tens of pN pushing force. When the micromanipulator is pushed to the chosen cells surface, $\Delta X$ (the difference between the T trap position and M center of mass of the trapped sphere) is regarded negative (*Figure 12.*). After 10 seconds of waiting, we pulled the structure backwards with 250 nm or 50 nm steps which resulted in retraction speeds of 0.5 μm/s and 0.1 μm/s, respectively.

At the beginning of the retraction, the micromanipulator does not move but the still negative $\Delta X$ slowly increases. If there is no adhesion between the manipulator and the cell, $\Delta X$ first becomes zero, then the manipulator detaches from the cell and follows the trapping foci ($\Delta X$ does not increase any more, *Figure 14/a.*). If there is any cellular interaction, $\Delta X$ becomes positive, and a considerable pulling force is exerted on the micromanipulator by the optical tweezer. Eventually, when the optical force becomes greater than the adhesion force, the manipulator separates from the cell's surface and the centers of the trapped spheroids return to the trap positions ($\Delta X$ becomes zero, *Figure 14/b.*). Next, either the same manipulator was used to test another cell (maximum of 3 measurements per manipulator) or another microtool was used on the following cell. All the experiments were repeated at least two times on different days and on different cell cultures and the number of parallel measurements in each experiment was 6-10.

## 6. AFM measurements

The AFM measurements with functionalized tips were carried out to validate the optical trap-based adhesion force measurements. Endothelial cells were cultured on a circular 24 mm diameter cover slip, previously coated with Matrigel, for 2 days in their respective media. The serum content of the media was reduced to 1% 2 hours prior to the start of the AFM measurement. The cover slips containing the cells were mounted inside of a lid of Petri dish for support. A drop of respective media was placed onto the cell layer and the AFM cantilever was immersed into it. All experiments were made with an Asylum Research MFP-3D head and controller in contact mode (Oxford Instruments Asylum Research), and the driver program (version 16.12.214) was used written in IGOR Pro Software (version 6.38B01, Wavemetrics)

which served also for the data analysis of the recorded data. The parameters for both the sharp-tipped and for the colloidal probes were the following: the typical dwell time before retraction (contact time) was 1s, the loading force was 100 pN and the retraction speed was varied between 0.5-5 µm/s. The spring constant for each cantilever were determined by the thermal fluctuation method (Hutter & Bechhoefer, 1993), (Butt & Jaschke, 1995).

## A: Cell-binding measurements with sharp tipped cantilevers

As a preliminary experiment we carried out adhesion probability measurements on hCMEC/D3 cells with simple sharp silica tipped cantilevers (Bruker, MSCT-D) which has a nominal spring constant of 30 pN/nm. We took care of using similar protocol as we used for functionalizing the SU-8 structures with GSH. In the first step the probes were incubated in 2% (v/v) APTES (Sigma-Merck Kft.) dissolved in isopropanol (Molar Chemicals Kft.) for 1.5 hours at room temperature to form free amine-groups on their surfaces (Ebner, Hinterdorfer, & Gruber, 2007), (Riener, et al., 2003). This was followed by a 1% solution of glutaraldehyde (Molar Chemicals Ltd.) incubation in water for 5 minutes (Wildling, et al., 2011) which enabled us to crosslink the APTES`s amine with the PEG-linkers free amine. Afterwards, the cantilevers were incubated in amino-PEG-maleimide linker solution of 10 mg/mL in ethanol for 20 minutes. The AFM tips coated up to this point were used as a negative control and referred as PEGylated. To demonstrate the effect of GSH with AFM the PEGylated cantilevers were immersed into freshly made 100 mM GSH in PBS buffer for 20 minutes.

## B: Adhesion force measurements with colloidal probes

To have comparable results to our microtool-based adhesion force measurements, we used 10 µm diameter, functionalized borosilicate colloidal probes; these were mounted on triangular cantilevers with a nominal spring constant of 10 pN/nm (NovaScan, USA) and provided similar contact area as the microtools. The functionalization of these spherical-tipped cantilevers was carried out by the same protocol as described in the previous section. Both type of endothelial cells (hCMEC/D3 and RBEC) were investigated with this AFM method.

# 7. Evaluation of the obtained data

A: Cell stiffness measurements evaluation

The position of the microtool on every video frame recorded during the approximation of the endothelial cells was determined with a correlation-based method where the reference was the image taken at the first position. The evaluating program was implemented in Matlab and the script used its built-in image processing and 2D cross-correlation features. The four spheres' positions were determined independently, by choosing a template image for each spheres which was a cropped image of the chosen sphere on the very first frame; this chosen reference image was then compared to the image of the same sphere on all other frames of the recording. The function resulted in a correlation matrix corresponding to each sphere at every frame of the recording. The correlation matrix has a maximum at the vicinity of the location of the sphere, but it is determined only with one pixel precision (which is in our case 120 nm). To obtain sub-pixel precision position for the spheres, the neighborhood of the matrices' maximum was fitted with a 2D Gaussian function. Afterward, the position of the microtool's tip was determined from the spheres' position data with simple geometric considerations assuming a rigid structure. The main reason why not the tip itself was monitored is that after tip had made a contact with the cell's surface its image became distorted, and it was impossible to apply cross-correlation on it. Finally, the position of the tip was calculated for all the images and was plotted as a function of the trap position. With this cross-correlation method, using a surface mounted, non-moving structures the tip position could be determined with 5.5 nm precision.

Only those measurements were used in the analysis where the tip's movement perpendicular to the direction of the approach was negligible after the contact (less than 50 nm). The evaluation resulted in a tip position vs. the trapping focus position traces for every indentation experiment, having two distinguishable ranges as demonstrated on *Figure 13/c.:* the first describes the movement before the contact happens between the microtool and the surface; in this range the microtool follows the trap position continuously, and its slope is 1. After the tool made the contact, it lags the traps position so the slope in this range is less than 1. Since the breakdown at the point of contact happened always at different trap position in the consecutive measurements, the traces had to be aligned with a separate procedure. We had two distinct set of traces, one for the cell indentations and another for the wall approach experiments. In the alignment procedure of both set of traces a reference trace was selected (usually the firstly made one) and the other traces were aligned to it. The alignment procedure

was determining the variance of the difference of two traces while one of them (*Figure 13/c.* red curve) was moved stepwise (in 10 nm steps) in relation to reference one (*Figure 13/c.* blue curve). The minimum of the variance curve gave the amount of shift used for the alignment procedure. In *Figure 13/c.* the inset displays three of such traces: the dark blue line has the smallest variance while the other two has almost 3 times greater.

After the alignment of the cell indentation and the wall approach measurements, the traces from the latter ones were averaged (n=9), while the cellular experiments were used individually further on to determine the microtool's displacements and the indentation of the cells.
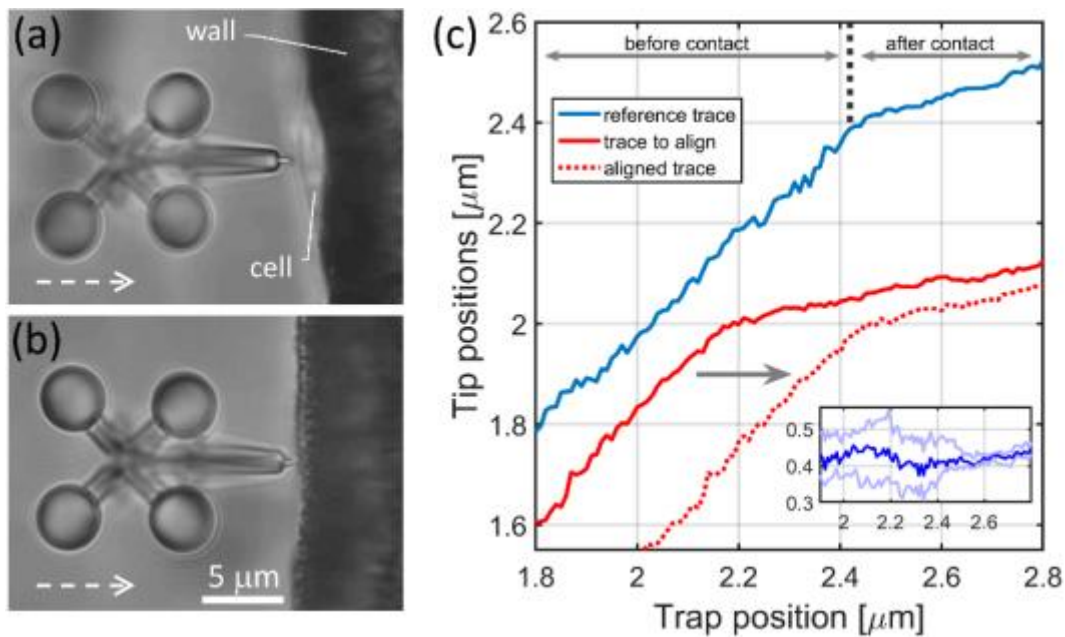


*Figure 13. cell indentation experiments and the resulted traces of the microtool's tip. Typical images of the cell indentation (**a**) and the wall approaching experiments (**b**), white arrows show the direction of the microtool movement during the approximation. The tip position was determined by determining the positions of the four handle spheres on the image series taken during the indentation measurements. (**c**) displays tip positions from two cell indentation measurements as a function of the trapping beam position (solid blue and solid red traces). It also shows the result of the trace alignment when the red trace is aligned to the blue one with the alignment procedure (dashed red). The inset in (**c**) shows differences of the red and blue traces during the alignment.*

## B: Adhesion force measurements evaluation

The recorded image sets were analyzed by a Matlab program for the adhesion-force measurements as well, but this time with a different algorithm. At all images from one adhesion force measurement, the program fits a circle for all four spheres of the used micromanipulator, and the centers of these circles are considered as the trapping sphere centers. The average position of the four centers of the spheres was then calculated and its coordinate along the direction of the movement of the optical trap was plotted as the function of the holding trap`s position. The micromanipulator position was plotted against the trap position only during the

retraction process (*Figure 14/c.* grey dots). While the manipulator was still in contact with the cell during the retraction, its position was constant. After the detachment of the micrmanipulator from the cell in each individual measurement, the averaged sphere center position coincided with that of the trapping beams and grows linearly with it according to a slope of 1. In the following step, a straight line was fitted to this linearly rising section, which was extrapolated to zero trap position and the averaged sphere position was subtracted from it, resulting the ΔX values (*Figure 14/c.* red dots).

The optical force was simply calculated by multiplying the ΔX values with the previously measured stiffness of the micromanipulator ($k_{str} = 25.8 \pm 2$ pN/µm). The adhesion force is the amplitude of the sudden drop of the optical force which is the result of the rupture in the adhesion between the manipulator and the cell`s surface (*Figure 14/b.*). Statistical analyses were performed using GraphPad Prism 8 software (GraphPad Software, USA). Values were compared using ANOVA followed by Bonferroni posttest. Differences were considered statistically significant at $p < 0.05$.
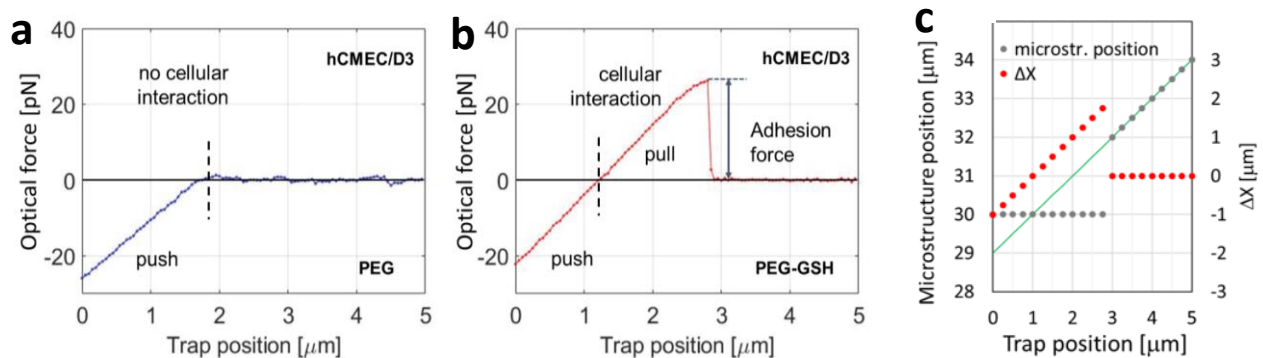


*Figure 14. (**a**) and (**b**) shows a typical adhesion force measurement plots for (**a**) a PEGylated and / control functionalized (**b**) GSH-coated micromanipulator on D3 cells with 50 nm stepsize which shows a strong cellular interaction, part (**c**) Illustrates the determination of ΔX from the manipulator position as the function of the trapping focus position (0 refers to the start of the pulling of the manipulator). Grey circles show modelled micromanipulator positions along the direction of the retraction in the image coordinate system. In this example, in the 0-3 µm trap position ranges the manipulator does not move due to its adhesion to the cell`s surface. At 3 µm it detaches from the cell and above 3 µm it precisely follows the trapping beam. The green line is the fit to this last, 3-5 µm section. ΔX is calculated by subtracting the microtool positions from the fitted line.*

# IV. Results and Discussion

## 1. Endothelial Cells Young's Modulus

The endothelial cells Young's modulus was calculated based on the Hertz model with the following equation used in the literature for AFM and OT indentation experiments:

$$F(d_z) = \frac{4E}{3(1-v^2)} R_b^{1/2} d_z^{3/2};$$

In the equation $F$ is the force which acted on the cell when the microtool was pushed against it, $E$ is the Young's modulus, $R_b$ is the indenter tool's surface radius, $d_z$ is the occurred indentation and $v$ is the Poisson number, what we selected to be 0.5 based on other experiments: AFM (Vargas-Pinto, Gong, Vahabikashi, & Johnson, 2013), OT (Dy, Kanaya, & Sugiura, 2013). The forces and the indentation were determined from the microtool's position as the function of the trapping beams position. The raw microtool tip positions, measured during the cell indentation experiment are shown on *Figure 15/a.* before the alignment procedure (see *Figure 13/b.*). Three individual traces illustrate the movement of the microtool changes sturdily after the microtool contacted with the cells: microtool's movement does not stop completely but the tool's position tails away from the trapping beams position. After the contact, the movement continues to be primarily a linear function of the trapping beams' position for at least another 500–800 nm of trap movement; in this regime, the tip moves less than 150 nm. Infrequently, the tip slips sideways on the cell membrane even by about 100 nm (*Figure 15/c.*). Traces from approximations of the SU-8 scaffolds with no cells on them (control experiment,
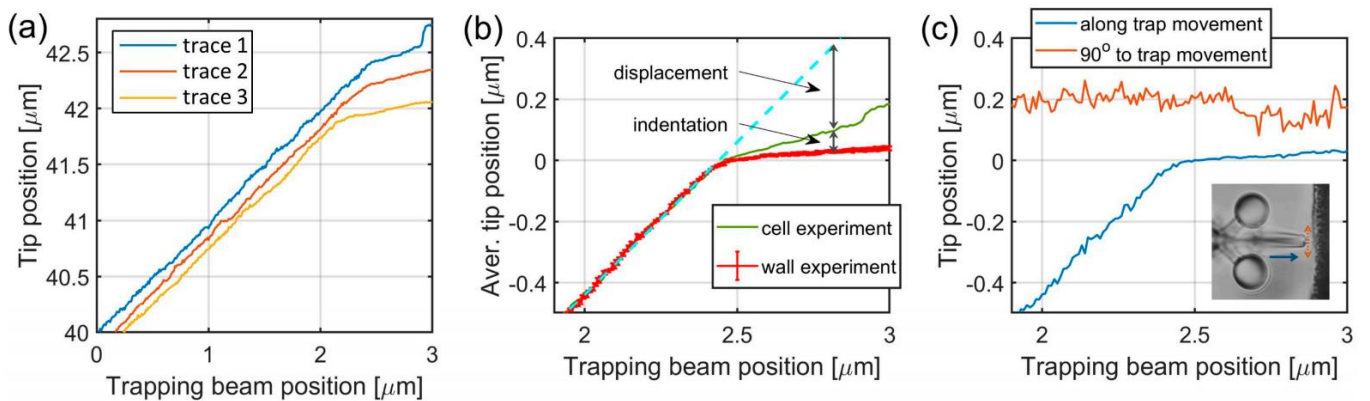


*Figure 15. Tip position traces for the calculation of endothelial cell's Young's modulus.  (a) Representative raw tip position traces as the function of the trap positions before alignment. (b) Tip position traces after the alignment procedure: the wall approach experiments were averaged for background (red curve), while the cell indentation traces were used individually (one representative trace: green curve). Panel (c) shows a tip position movement parallel (blue) and perpendicular (orange) to the trap movement during the tool being pushed against a hard wall*

red curve) and one aligned tip position trace when pushed against a cell (green curve) are shown in *Figure 15/b.*

Since the tip can slip sideways, the tip position is mainly meaningful in the first 400 nm after the contact point, where this effect is negligible. When a tip was pushed against the hard SU-8 wall, it had a residual forward movement after the contact point, which was attributed to its small sideway movement. Since this may also happen in the cell experiments, the observed extra forward movement at the walls was used as a correction in the cell indentation measurements (the tip positions of the cell experiments were compared to this "baseline"). A representative experimental result of an approximation of a hard wall is shown in *Figure 15/c.* It demonstrates that the tip moved forward a few tens of nanometers during the first 400 nm beyond the contact, while it slipped about 50-80 nm sideways. In *Figure 15/b.* two position traces are shown which were used to determine the indentation and the pushing force in the Hertz model for each individual measurement. The difference between the tip position when approaching the wall and when approaching the cell gives the indentation. A straight line was fitted to the linearly increasing part of the cell approach trace (*Figure 15/b.* cyan dashed line) and the difference between this and the tip position trace after the contact point was used to calculate the displacement. The cell indentation and the microtools displacement as a function of trap position is displayed on *Figure 16/a.* The indentation force was determined from the displacement by multiplying it with the stiffness of the microtool ($k_{str}$); the resulted force ranged between 1-5 pN, which transcends the AFM precision. Both the indentation and the
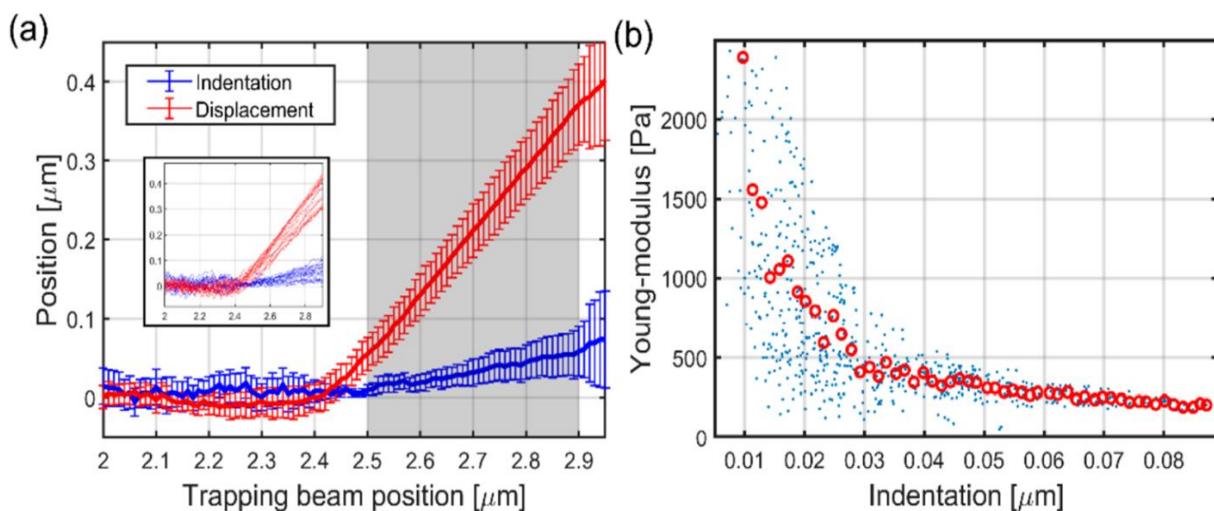


*Figure 16. Measured indentation and displacement data and the Young's modulus calculated from them. The indentation (blue line) and displacement (red line) data on panel (**a**) are calculated from the aligned traces; the error bars represent SD. The shaded area highlights the reliable range for the two quantities. The inset shows the individual displacement (red) and indentation traces (blue) calculated separately for the 19 experiments. The Young's modulus as the function of indentation over the values highlighted in (**a**) is shown in panel (**b**). The blue dots represent all the approximately 800 individual point pairs (40 trap positions × 19 experiments), while the red circles are their averages in 60 regions over the 0–0.09 μm indentation range.*

displacement traces have a break point between 2.4 and 2.5 µm, but about 400 nm beyond the contact point they produce large errors. Therefore, the Young's modulus could be obtained reliably from the range of 2.5–2.9 µm. *Figure 16/b.* shows that the obtained values range from 220 Pa up to 1500 Pa, but between 2.5-2.6 µm trap positions (indentation between 0.01 µm and 0.02 µm) the determined values have significant noise. The obtained data was recorded with 4 microtools on 6 cells, altogether 19 measurements was carried out.

These measured values are parallel with those determined by AFM-based methods on endothelial cells from pulmonary artery with a modulus of 400–1500 Pa (Pesen & Hoh, 2005) on bovine aortic endothelial cells with 700-2700 Pa (Ohashi, Ishii, Ishikawa, Matsumoto, & Sato, 2002) on human umbilical vein endothelial cells (HUVEC) with 350-4000 Pa (Vargas-Pinto, Gong, Vahabikashi, & Johnson, 2013) or on the same type of cells with an another technique based on magnetic tweezers with 400 Pa (Feneberg, Aepfelbacher, & Sackmann, 2004). Interestingly those values which were achieved with AFM, the moduli can vary an order of magnitude for the same type of cell in the literature. The most possible reason for this broad range could trace back to the measurement conditions: the rate and amount of indentation and the indenter tool's shape. In the literature it was demonstrated that the indentation rate increases the Young's modulus mainly due to viscous effects and that about 0.25 µm/s probe velocity was the lower limit of viscous dissipation (Mathur, Collinsworth, Reichert, Kraus, & Truskey, 2001). The AFM measurements' loading rate has a wide span from ~100 pN/s to hundreds of nN/s (Coceano, et al., 2016)). Our OT-based measurements take about one minute each, and it is only about the last tenth of the measurement, where the tip reaches and indents the cell with about 60 nm; by the end of this period, the force increases to about 6 pN, what corresponds to 1 pN/s loading rate and the indentation rate of 0.01 µm/s which is much smaller than those for AFM. In our experiments due to the low indentation rate, we consider the viscous effects negligible in measuring the Young's moduli.

Furthermore, when the amount of indentation is too large, the intracellular actin network /cytoskeleton could spoil the measurement of the elastic properties of only the cell membrane. The relatively large noise observed for small indentation values were very likely produced by the thermal fluctuation of the trapped microtool, when small indentations and forces are applied. In addition, the indenter tool's shape and surface area also plays a role: as an example, AFM tips with radii of 20 nm and 5000 nm in the indentation experiments of Vargas-Pinto and co-workers yielded Young's modulus values of 3.8 kPa and 350 Pa, respectively, on the same cell type (Vargas-Pinto, Gong, Vahabikashi, & Johnson, 2013). Other experiments

demonstrated that colloidal probes (r = 7.5 µm) measured half the value on a same MDCK cell as the pyramidal tipped cantilevers: 400 Pa versus 800 Pa (Harris & Charras, 2011). Similar result was observed when mouse fibroblast cells were analyzed by pyramidal, flat topped and colloidal probes (Chiou, Lin, Tang, Lin, & Yeh, 2013). Our indenter tool's tip has ~300 nm radius, which is much larger than the conical AFM probes and rather comparable to those what were used in arrangements using optical tweezers. With our method, it is possible to measure the moduli in the lower hundreds of Pa range. Although the optical force of our presented experiments together with the 300 nm tip radius of the microtool yielded the indentation values of up to 90 nm, our operating range can be easily increased to greater values with higher trapping laser intensity and smaller trapping sphere diameters.

# 2. Preliminary experiments for adhesion force measurements

## A: Visualizing and calculating the surface coverage of GSH

In order to properly interpret the adhesion force measurements carried out on different types of cells with covalently immobilized GSH on SU-8 surface, as described in *chapter 5C* of Methods, I had to prove that the GSH molecule is detectable on this kind of surface. The rational choice was to use fluorescent dye to visualize the GSH presence on top of SU-8. For that purpose, I chose an amine reactive stain, because the GSH is containing one primary amine group per molecule. The amine-reactive CY-5 staining was performed after the three main steps of Protocol 1, as detailed below, and after a PEG-bisamine treatment:

- **CAN:** acid treatment only, *Protocol 1*, steps 1-2      **+ amine reactive dye**
- **Linker:** acid + amino-PEG-maleimide treatment, *Protocol 1*, steps 1-4,
  **+ amine reactive dye**
- **PEG-bisamine:** acid + PEG-bisamine treatment, *Protocol 1*, steps 1-4, but instead of amino-PEG-maleimide, PEG-bisamine is used**,**      **+ amine reactive dye**
- **GSH:** acid + amino-PEG-maleimide treatment + GSH treatment, *Protocol 1*, steps 1-7
  **+ amine reactive dye**

<u>**CAN:**</u> this layer works as one of the negative controls for nonspecific association of the amino-reactive dye upon the polymer surface.

**PEGylated:** this functionalization was applied for all the following GSH adhesion experiments as a negative control, since here only the terminal GSH is missing. It also worked as one of the two negative controls for the CY-5 fluorescence experiments.

**PEG-bisamine**: this PEG-linker has primary amine-groups on both ends, so I used this as a positive control to confirm that CY-5 indeed binds to primary amine groups, found on GSH.

**GSH:** the PEGylated surface's maleimide group forms an oxime-ether bond with the thiol-group of the GSH molecule. The primary amine on the GSH binds the reporting amine-reactive CY-5.

First, I applied *carboxyfluorescein* staining to visualize the coverage. That turned out have two major drawbacks: it provided very low fluorescence intensities even if overnight incubation were used, and the autofluorescence of SU-8 is considerably at the excitation wavelength of dye (FITC excitation center wavelength $\lambda = 475$ nm). After some endeavoring, we purchased an another amino-reactive dye which was CY-5-ester based fluorophore. The excitation wavelength of this dye ($\lambda = \sim 650$ nm) is far enough not to excite SU-8. Further advantage was, that for the amine-reactive CY-5 much shorter incubation time was sufficient.

In *Figure 17.* functionalized and fluorescently stained SU-8 blocks can be seen; in all images CY-5-ester dye was used with 30 minutes incubation time, both for fluorescence and confocal microscopy. The fluorescent intensities were measured in the central region of each
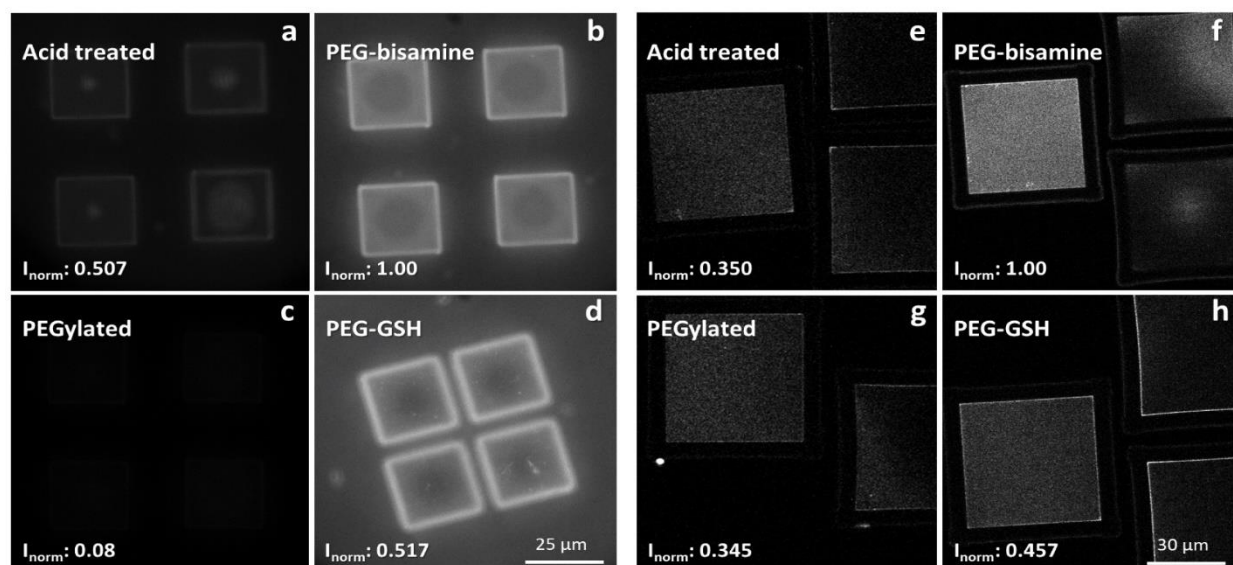


*Figure 17. CY-5 stained, and differently functionalized SU-8 blocks. Wide-field fluorescent (a-d) and confocal (e-h) microscopy images of the functionalized SU-8 blocks.*

square, and in the case of the wide-field microscopy the intensity, measured on the glass surface adjacent to the squares, was subtracted as background. For confocal microscopy it was not necessary since the glass surface was not imaged for it situated a few micrometers below the focal plane. At all samples, the resulted intensities were normalized with/to the positive control's values. At all types of samples at least 10 TPP fabricated blocks were imaged and evaluated to obtain the normalized average shown in the lower left corner of the corresponding image. With both microscopy method I demonstrated that the GSH-functionalized SU-8 blocks have greater fluorescence than in case of the negative controls. I concluded that GSH can be immobilized with covalent bonds to SU-8.

To obtain the surface coverage of GSH on SU-8, first we determined the integrated fluorescence intensity of single CY-5 molecules (*Figure 18/a.*) with the methodology detailed in subsection Methods 2B. The integrated fluorescent intensity of the image of a single CY-5 fluorophore molecule was measured to be 200±39 pixel intensity unit (n=71) (*Figure 18/b.*). The determined average fluorescence intensity for each pixel (where a sample area of 100 nm x 100 nm was imaged) on the GSH functionalized sample was 6727±349 (n=7) and on the PEGylated sample 1794±224 (n=21). The difference of pixel intensity values between the GSH functionalized and the PEGylated one was integrated over one $\mu m^2$ and the result was divided by the integrated intensity of a single CY-5 molecule, what gave us 2464±770 molecule/$\mu m^2$ surface coverage value (~25 GSH molecule/ 100 by 100 nm).



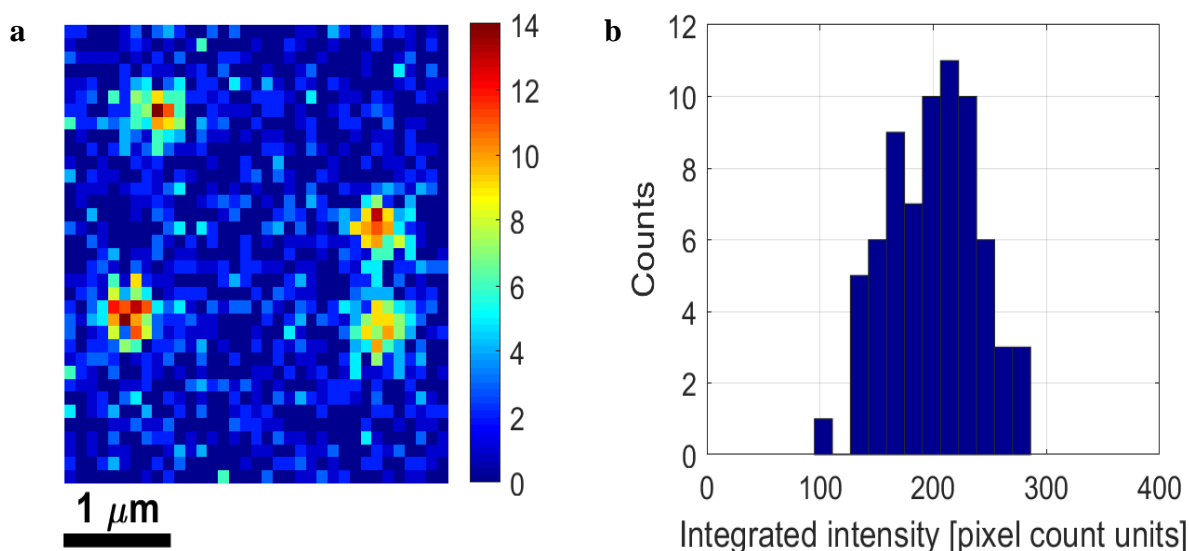*Figure 18. The integrated intensity determined from the fluorescent images of single CY-5 fluorophore molecules (**a**) were used to calculate the surface coverage of CY5 on the homogeneously coated layers (the colorbar shows fluorescent intensity in pixel count units). The intensity of the single dye molecules was quite uniform, giving a well-defined average integrated intensity value (**b**) (N=71).*

Supposing that each GSH binds one fluorophore molecule, this results in approx. 2500 GSH molecules on every square micrometer on the surface of the SU-8 structures.

## B: Binding probability on 4 types of cells with ellipsoids

Before we made the binding measurements, I had done preliminary experiments with simple microstructures (ellipsoids) made by TPP fabrication on 4 types of cells: primary rat brain endothelial cells (RBEC), human endothelial cell line (hCMEC/D3), primary rat brain astrocytes and pericytes to shed light on the binding probability between them and PEGylated and PEG-GSH functionalized SU-8 surfaces. We expected that the GSH coated ellipsoids can reach a better binding ratio than the control functionalized ones on the different cells. We carried out these measurements on our HOT setup, where the cells were grown on a horizontal glass surface instead of a vertical wall, with the addition of a temperature-controlled sample holder which was able to provide 37 C° for the whole time of the experiments. For each cell type we made at least 2 series of binding attempts on different cultures and days.

A binding attempt was carried out as follows: an individual, previously functionalized (either PEGylated or PEG-GSH) ellipsoid was picked up by the optical tweezer, and then it was pushed to the cell's surface nearby the nucleus cell by cell, where a planar surface was expected. It was pushed against the cell for 10 seconds and after that the optical tweezer was slowly moved upwards to remove the ellipsoid from the cell. This could end with binary output: if there was not enough adhesion between the cell and the ellipsoid, then it could be removed
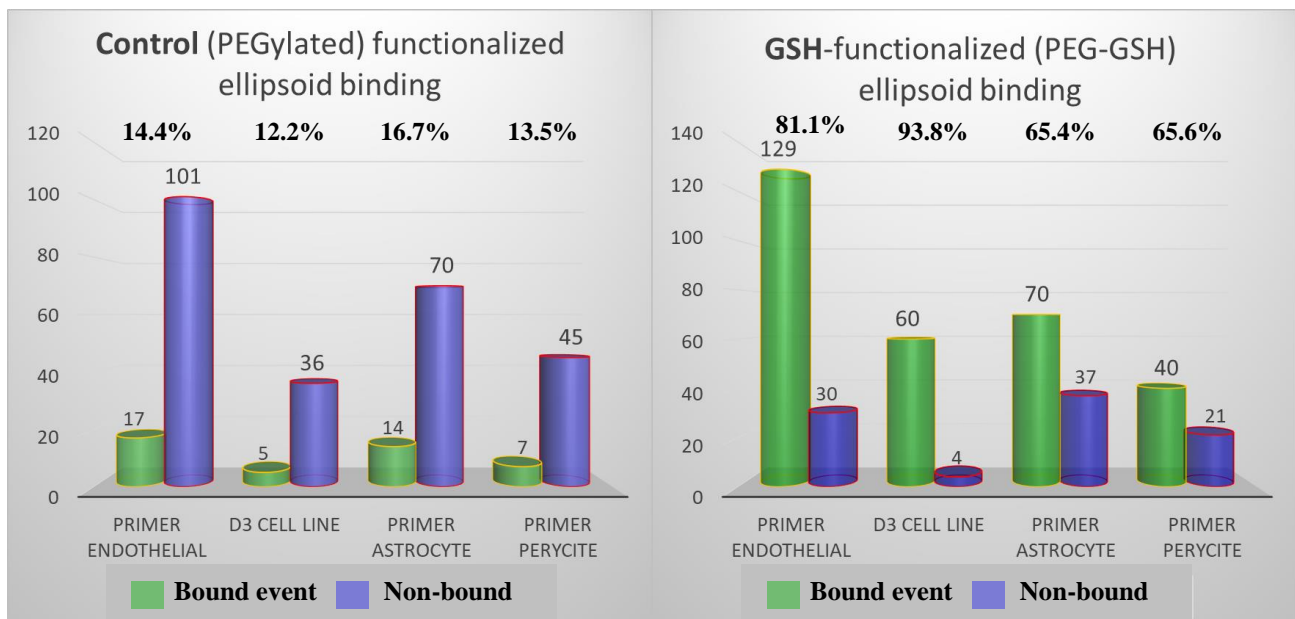


*Figure 19. Ellipsoid binding experiments on four different cells. On the left side the PEGylated ellipsoids binding probabilities are show, ant the right the same for PEG-GSH functionalized ones*

from the cell membrane (**non-bound event**); if there was enough adhesion, the microstructure could not be removed by optical forces (**bound event**).

At *Figure 19.* the ellipsoid binding experiments' results are shown, whit the representing element number and the binding probability in terms of percentage (bound events divided by all) at the top of each column. A clear distinction could be observed between the binding probabilities of the PEG-GSH functionalized ellipsoids relative to the PEGylated (control) ones for all 4 cell types. When GSH was present on the surface, the ellipsoids bound to primary endothelial cells with 81% probability as compared to 14% in the absence of it. Similar results were observed with hCMEC/D3 cells where GSH-coated ellipsoids reached 93% binding probability versus only 12% in the control functionalized ones where the GSH missing.

After these experiments I was convinced, that in the final adhesion force measurements pericytes and astrocytes cannot be used, because they grew in a random 3D structure which would make it very hard to reach them on the SU-8 walls. The other two endothelial cells have more 2D shapes flattened to the surface of the substrate, therefore they can be approached easier with the microtools.

In our Institute, my co-workers carried out binding probability measurements with functionalized AFM tips on hCMEC/D3 cells as support experiments to my optical trap measurements (experiment carried out by Zsolt Szegletes). *Figure 20.* shows that the PEGylated sharp tipped cantilevers would not bound to the surface of the cells at all, while the GSH-functionalized ones achieved 94% binding probability (NPEG = 42, NPEG-GSH = 124). These results indicate that the surface of the applied cells preferentially binds to GSH-covered surfaces. The increased binding can explain the greater cellular uptake and transcytosis trough the BBB where the GSH is present in the niosomes' outer membrane, as others and our colleagues observed in uptake experiments of PEGylated and GSH functionalized niosomes (Geldenhuys, Wehrung, Groshev, Hirani, & Sutariya, 2015), (Porkoláb, et al., 2020).
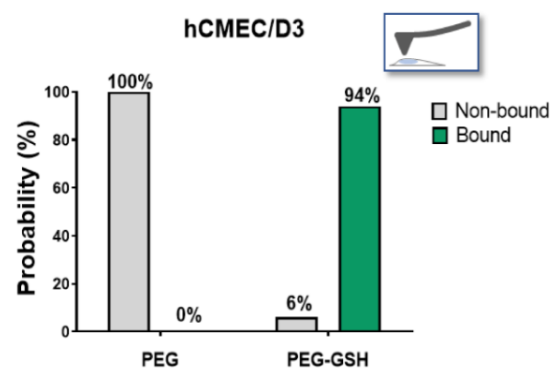


*Figure 20. AFM binding probability measurement with sharp silica tip on hCMEC/D3 cell, with control (left) and GSH-functionalized (right)*

# 3. Adhesion force measurements

After presenting that the GSH can greatly increase the binding probability of SU-8 microstructures and sharp silica tipped AFM cantilevers to brain endothelial cells, we performed adhesion force measurements with our HOT system to quantify this force. I used for these measurements TPP-made and optically manipulated micromanipulators with flat contact surface, where the cells were cultured on a vertical scaffold-like supporting wall. I carried out at least two individual measurements with each cell type and functionalization parameters on different cultures and days. The retraction of the micromanipulators in a well-controlled manner by stepping the trapping foci after they were pushed against the cell's surface has a capital importance in these measurements. These retractions were made with two different step sizes, namely 50 and 250 nm which represents the following retraction speeds: 0.1 μm/s and 0.5 μm/s respectively; this way we could check if the speed has any influence on the adhesion force. Because the SLM has a fixed refresh rate the time between the steps was kept constant.
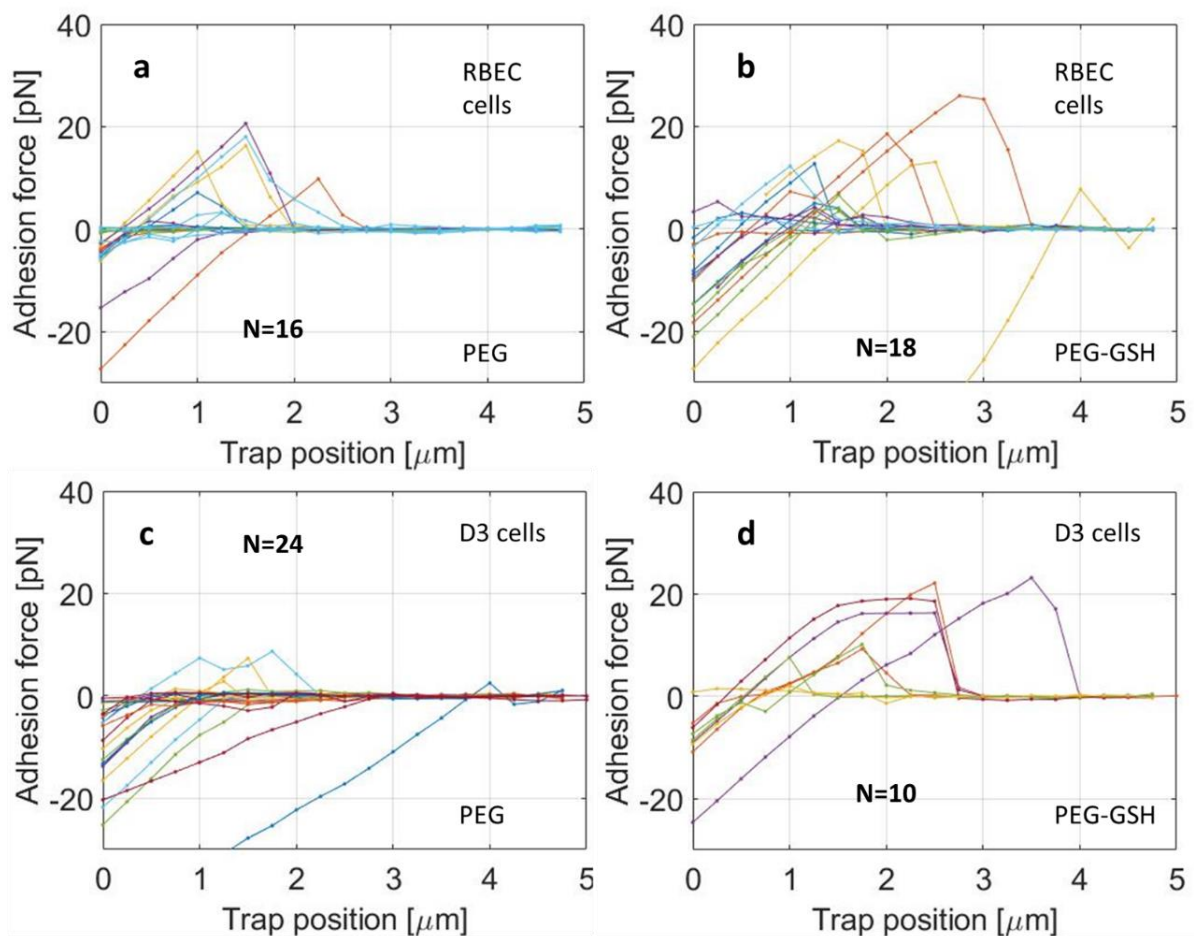


*Figure 21. Optical force curves from all experiments on (**a, b**) rat brain endothelial cells (RBEC) and on (**c, d**) human cerebral microvascular endothelial cells (hCMEC/D3) made with 250 nm stepsize*

In *Figure 21. and 22.*, significant difference can be observed between those traces which were recorded with GSH-functionalized manipulators and those obtained with the control ones. Also, both aforementioned figures display that the micromanipulators are pushed against the cell with a few tens of pN optical force at the beginning of the retraction process (trap position = 0 μm), which then linearly decreases (in terms of absolute value) when the tool is pulled backwards. If there was adhesion between the micromanipulator and the cell, the pushing force switches to pulling during the retraction, otherwise the manipulator detaches from the cell membrane and no pulling force acts on it. In case of adhesion, the cell membrane was pulled by the micromanipulator up to a particular trap position, where the bond between the two surfaces ruptures and they detach from each other, returning the optical force to zero. The optical force at the rupture position defines the adhesion force. Curiously, we did not find any correlation between the initial pushing force and the magnitude of the adhesion force.
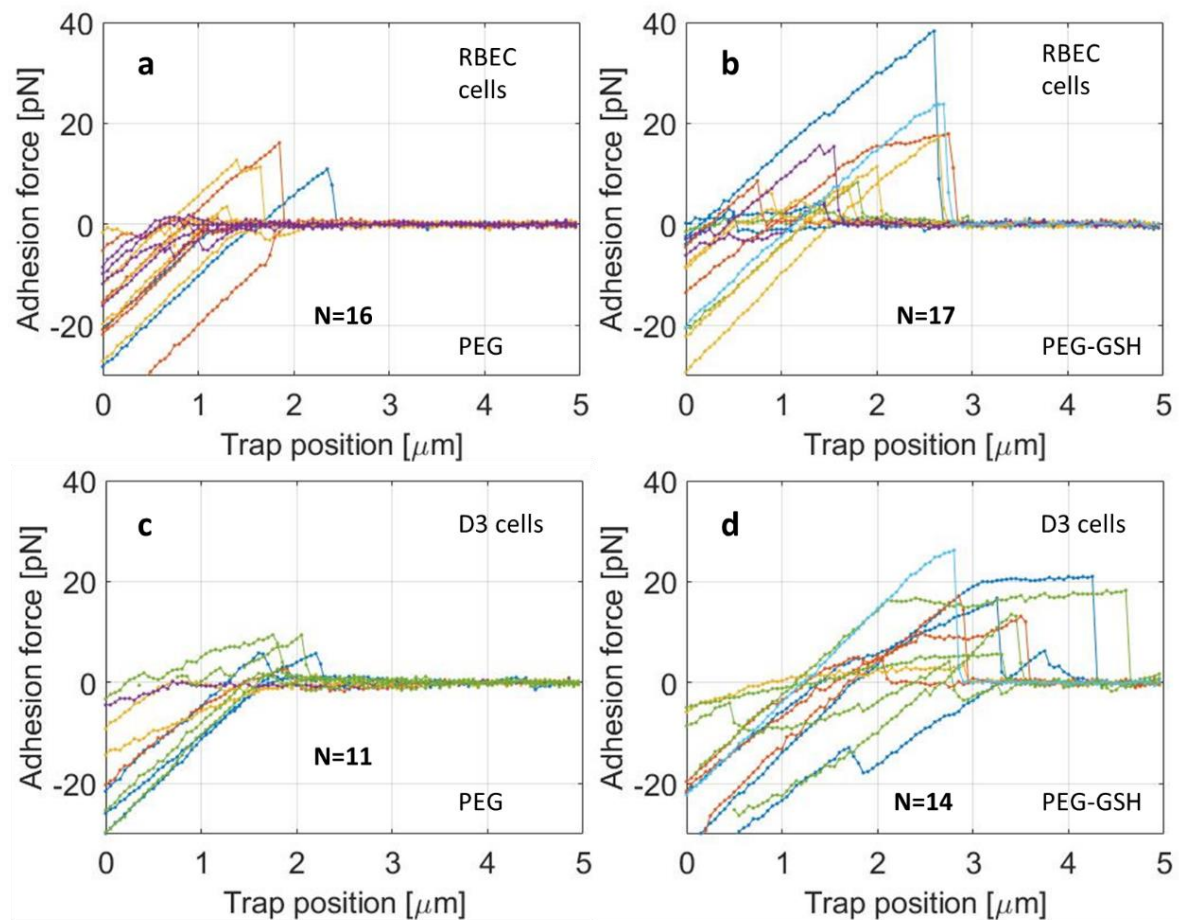


*Figure 22. Adhesion force curves from all experiments on (**a, b**) rat brain endothelial cells (RBEC) and (**c, d**) on human cerebral microvascular endothelial cells (hCMEC/D3) made with 50 nm stepsize*

When I averaged the adhesion forces for each individual group (*Figure 23/a, b.*), I observed that the means of the adhesion forces were always significantly greater when GSH was present than when it was omitted, and the ratio of the average measured adhesion forces between the

two functionalization groups could be as high as eight. In case of the GSH-coated structures, the difference between the 50 nm stepsize values and those recorded with 250 nm stepsize was not found to be statistically significant. With 250 nm stepsize, we measured $9 \pm 6.6$ pN adhesion force for RBEC cells and $16.4 \pm 6$ pN for hCMEC/D3 cells when the targeting ligand GSH was present, while for PEGylated micromanipulators the adhesion forces were only $2.2 \pm 3$ pN for RBEC and $2 \pm 4.3$ pN for hCMEC/D3; the element numbers are shown on the graphs of the individual force curves (*Figure 21.*).

When the smaller stepsize was used, the average adhesion force for GSH functionalized micromanipulators was $12.1 \pm 9.5$ pN on RBEC cells and $10.2 \pm 7.2$ pN on hCMEC/D3 cells, whereas in case of the PEGylated manipulators, our control group, it was $3.4 \pm 4.9$ pN RBEC and $3.8 \pm 3.2$ pN for hCMEC/D3 (*Figure 22.*). In case of D3 cells, when the slower speed was applied, we observed large plateau like curves. We hypothesize that it can be explained by pulling short tethers formed by the cells or the micromanipulator was attached to cell's primary cilia (Lim, McGlashan, Cooling, & Long, 2015).

We performed experiments with similarly GSH functionalized colloidal AFM cantilevers where a 5 µm radius spherical bead was attached at the tip of it (*Figure 23/c, inset*); we chose this special cantilever because it had a comparable contact surface with our manipulator. The



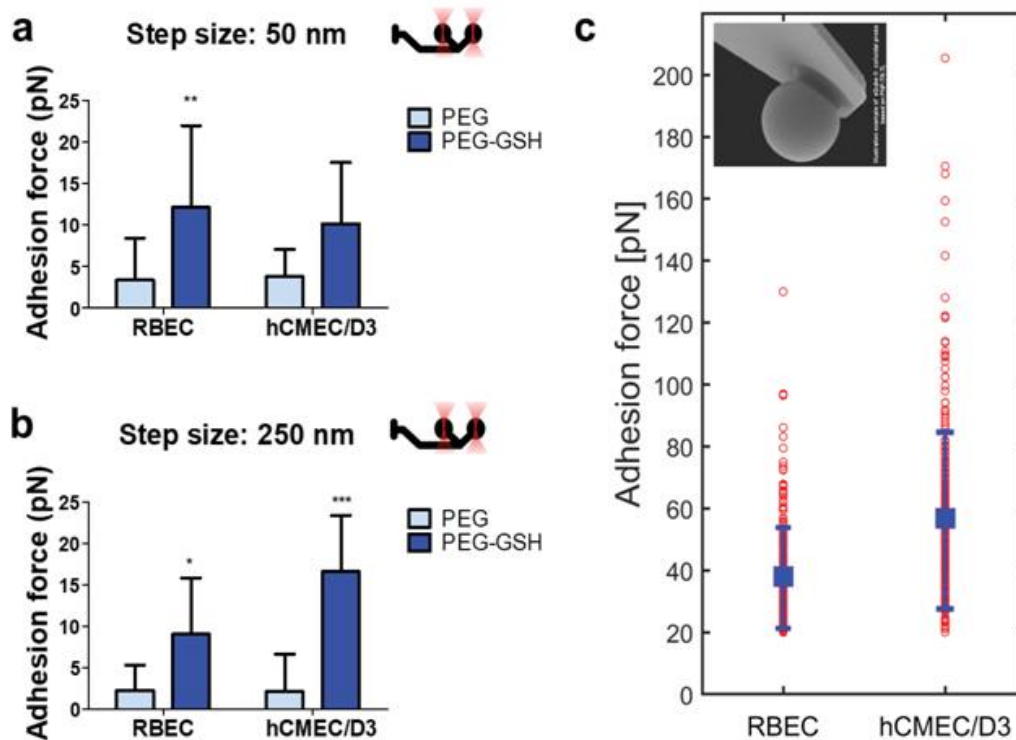*Figure 23. Summary of the adhesion forces obtained with the GSH and with the PEGylated microtools on brain endothelial cells using two step sizes indicated in (**a**) and (**b**). (**c**) Adhesion forces between PEG-GSH functionalized colloidal tipped cantilevers and the surface of endothelial cells, as measured with the AFM. Red circles represent individual measurements, blue squares are their means, blue whiskers are SD.*

AFM measurements resulted in 3-6 times greater adhesion forces than those obtained with the HOT method both for RBEC cells (38±18 pN), and for hCMEC/D3 cells (57±28 pN) (N=247 for both cases). The most possible reason why the AFM measurements showed much larger adhesion forces is that the AFM probe was pushed against the cell with 100 pN which is almost an order of magnitude higher than in the HOT measurements (there we used only 10-30 pN) what could generate higher number of bonds. On the other hand, the AFM's detection level is around 10 pN, so only those measurements were taken into account which resulted in higher adhesion force than this limit.

Similar interaction forces (20-60 pN, depending on the loading rate) were measured by AFM between T24 cancer cells and folic acid targeted carbon nanotubes, which corresponded to our values (Lamprecht, et al., 2014). The fact that the optical trapping-based method yields adhesion force values in the same range as the more standard AFM, reassured us that it is an effective tool to characterize ligand binding to cell membranes. The OT based method has an additional advantage over the AFM: it has higher sensitivity, since it can measure from tenth of pN up to some tens of pNs. From technical point of view, it is interesting to consider the surface roughness of the SU-8 polymerized structures. We believe that it does not play a role in the observed adhesion forces, because the peak-to-valley height difference on the "rough" SU-8 surface is less than 10 nm, as measured earlier with AFM (Aekbote, et al., 2012). Furthermore, this minor variation takes place over a few hundreds of nanometers in the lateral direction on the surface of the polymerized object, resulting in a low steepness. In this series of experiments, we used 2000 g/M PEG-chain which has around 15 nm length in total, considering that one PEG-unit length is in the regime of 0.26-0.36 nm (Oesterhelt, Rief, & Gaub, 1999). Based on these data, if the PEG-linker coupled GSH is sitting on the bottom of one of the 'valleys', the GSH can still reach out from there.

We can conclude that the GSH could be an effective BBB targeting ligand in NP carrier-mediated drug uptake, but unfortunately very few details of the mechanism of GSH-aided NP adhesion to the cell membrane are clear. There are further OT-based technics which served information about ligand-receptor binding forces. As an example, ligand-binding domain of Notch1 protein were immobilized on the surface of microbeads to measure adhesion force on Dll1-expressing cells. In these experiments the authors measured rupture forces in the range of 0-40 pN and determined that the single bond can be broken with an average of 19 pN force (Shergill, Meloty-Kapella, Musse, Weinmaster, & Botvinick, 2012). Also, adhesion forces between claudin-3, -4 and -7-expressing epithelial-like human breast adenocarcinoma (MCF-7) cells and its ligands were investigated similarly with microbeads. The ligand c-CPE-coated

(enterotoxin of *Clostridium perfringens*) microbeads were held a few micrometers above the glass substrate and attachments were made in lateral directions towards the tested cells; the measured forces were between 5-30 pN (Riesenberg, et al., 2020).

The results of the GSH-coated adhesion force measurements on endothelial cells are in the same range as those of the previously mentioned OT-based experiments. The resulted 10-15 pN adhesion force in case of GSH-coated micromanipulators suggests that it could be a single bond rupture event. Also, the interaction of GSH with the cells seems to be specific, because without it the adhesion was just 2-4 pN. As for the molecular background of the GSH binding to the cells, we believe that the middle cysteine's thiol group of GSH tripeptide is not playing a role in the adhesion because it was used to connect GSH covalently to the PEG-linker's maleimide-group.

GSH binding could be further investigated by applying neuraminidase on the target cells to eliminate their glycocalyx and expose their transporter receptor proteins in higher number and more reachable. Furthermore, we could shed light on the importance of the cell's surface charge. We know from previous lab-on-a-chip experiments that the endothelial cell's surface charge has a large effect on BBB's permeability (Kincses, et al., 2020); also, it was demonstrated in our Institute, that when the overall charge of the cell membrane was tuned to more positive with neuraminidase treatment, the niosomes could reach significantly higher uptake (Mészáros, et al., 2018).

If we combine this surface charge modification treatments with our newly developed adhesion force measurement setup in a future experiment, the number of bonds is expected to be presented in larger number, and perhaps the applicable optical forces may not be strong enough to rupture them. So, in this case the functionalization protocol or the micromanipulators' contact surface should be fine adjusted. Furthermore, with small changes, our proof-of-concept measurement method could be extended to study dozens of ligands or chemoattractant molecules thanks to a diverse range of functional PEG-linkers.

# V.   Conclusion

In my thesis I demonstrated that optical tweezer-based techniques are capable to explore living cells' physical and biochemical properties. First, the measurement of Young's modulus of endothelial cells can be carried out with precisely manipulated two-photon polymerized, purpose designed microtool. Furthermore, the stiffness measurement technique could give very different results depending on the parameters of the experiment: if the pure linear elasticity of the cell is the topic of interest, it is believed that use of indentation surfaces with large radius of curvature and small loading rates with small forces is more potent to examine specifically that. Our method is perfectly capable to operate in this regime.

In our other work/publication we reported for the first time GSH adhesion forces to brain endothelial cells (D3 and RBEC) using our novel holographic optical tweezer-based binding force measurement technique. In those series of experiments, I used similar SU-8 micromanipulators as in the previous work which could prevent the cells from photodamage. The laser microfabrication made it possible to easily change the geometry of the micromanipulator's probe as the experimental methodology required. In both type of measurement arrangements, we used a cell culturing method where the cells were grown on mask-lithography made walls, which were parallel to the optical axis what enabled us to measure the adhesion force and the stiffness in a direction perpendicular to the cell membrane by approximation of the cell via lateral movement of the trapped micromanipulator.

We measured adhesion forces in the regime of 10-15 pN when the GSH was present that indicates a specificity towards glutathione: when void of the targeting ligand (PEGylated structures) we observed 3-8 times smaller forces. The adhesion forces what we observed coincide with those what could be found in the literature for other receptor ligand pairs also measured with optical trap-based methods. Our method could be extended in the future to differentiate between multiple and single binding events, to characterize other BBB targeting ligands with the adhesion force on living cells or even to select novel targeting molecules. The functionalization protocol could be easily adapted to immobilize those molecules with covalent bonds, thanks to the variety of PEG-linkers.

# Appendix I.

# Protocols

## 1. Functionalizing structures with PEG-maleimide and GSH

1. Hard bake the SU-8 samples on a hot plate at 110 C° for 10 min. Wait for the sample to cool down with the plate.

2. Acid treat them for 30 min at room temperature. For 5 mL acid solution, add 265 mg of Cerium-ammonium nitrate and 0,35 mL of 65% $HNO_3$ to 4,65 mL $H_2O$. (acid treatment step)

3. Wash the sample with de-ionized water (DI-water) in a clean Petri dish twice, for 10 min each.

4. Solubilize 1 mg of PEG-maleimide in 4:1 mixture of $MeOH:H_2O$ and cast it on the dried structures in small droplets. Keep the PEG-maleimide on the structures for 45 min at room temperature. (PEGylation step) For PEG-bisamine treated SU-8 surface, use PEG-bisamine instead of PEG-maleimide the same way.

5. After the PEG-maleimide or PEG-bisamine treatment, rinse the sample with DI-water in a clean Petri dish twice, for 10 min each. Dry it with a gentle nitrogen steam.

6. Place 3 mL of 100 mM GSH (reduced) in PBS on the PEGylated sample for 1 hour at 4 C° in a Petri dish. (GSH treatment step)

7. Wash the sample with DI-water once for 10 minutes, and then in PBS for 10 minutes. As a last step, wash it with DI-water and dry it with nitrogen steam.

## 2. Staining functionalized SU-8 surfaces with CY-5 amine reactive dye

Apply the following steps on acid-treated, PEGylated, PEG-bisamine treated and GSH-treated SU-8 samples.

1. Prepare a 0.1 mg/mL stock solution of the CY-5 amine reactive dye in 1:1 $DMSO:H_2O$ mixture.

2. For staining, dilute the stock solution to 0.01 mg/mL with 1:1 $DMSO:H_2O$ mixture.

3. Place 100 μL of staining solution on the sample and incubate it for 30 minutes at 4 C°.

4. Rinse the sample with DI-water, then wash it in a 1:1 mixture of DMSO:$H_2O$ for 10 minutes and in 5% DMSO for 10 minutes.

5. As a last step wash the sample with DI-water and dry it under nitrogen steam

   **Important:** all these steps should be carried out in dark to avoid bleaching of the dye.

## 3. Cleaning the glasses

Clean the soda-lime glass coverslips or Petri dish bottoms with solutions prepared freshly before use:

1. Add one gram of $K_2Cr_2O_7$ to 150 mL of DI-water. When it is completely solvated, immerse the glasses in this solution.

2. Slowly add 1 mL of 20-35% $H_2O_2$ to it. **Caution**: It is a highly corrosive solution, do not drop any kind of organic compound in it.

3. When the solution finished bubbling oxygen and turned back to orange, repeat step 2 for 2-3 times depending how scabious are the glasses.

   **Important**: too many repeats can cause $Cr_2O_3$ nanoparticle deposition on the glass surface (it could be noticeable by a slight greenish color).

4. Wash the glasses with DI-water and dry with $N_2$ steam.

5. Before spin coating, use a freshly made Aqua Regia solution

6. Wash the cleaned glasses with DI-water thoroughly and then rinse them with acetone to ease the drying. Place them on 110 C° hotplate to evaporate the water monolayer from the glass.

7. After 2-3 minutes of baking let them cool to room temperature, and immediately spin-coat SU-8 onto the sample.

## 4. Spin-coating and processing SU-8 layers for microstructures

To make SU-8 micromanipulators and blocks the obtained layer should be at least 16 μm tick. For that purpose, we use SU-8 2007 photoresist.

1. Using a pipette tip, smear about 100 mL of SU-8 on the cleaned glasses.

The spin-coating process could be decomposed to two steps:

2. The first spin-coating step is the dissipation of the resist on the glass: spin the glass with the photoresist on it at low, 500 RPM for 5 seconds with 100 RPM/sec acceleration.

3. In the second spin-coating step, spin the glass at 700 RPM for 30 seconds this results in the final 16-17 μm tick SU-8 layer.

4. After spin coating, bake the layers for several minutes at 95 C° to evaporate the great portion of solvents.

5. The layers should bake for several hours at least at 70 C° to evaporate the residual solvents.

6. The solidified layers can be manufactured with either TPP or mask-lithography

7. After illumination baking the sample for a 10-minute at 100 ℃ to complete the photopolymerization-chain reaction

8. When the sample cooled down to room temperature the development succeed as 3 washing step in PGMEA for 10 min and after 3 washings in 1:1 EtOH:$H_2O$ mixture

9. The developed samples dried under $N_2$ steam

## 5. Spin-coating SU-8 layers for cell walls

To make 80-100 μm tall SU-8 walls SU-8 2075 photoresist was used which is a more viscous resin.

1. First, place a pea sized bead of SU-8 at the center of the round glass Petri dish bottom and disperse it with a pipette tip.

2. Spin the glass at 500 RPM for 5 seconds with 100 RPM/sec acceleration.

3. Spin the glass for 30 seconds at 2500 RPM. This yields in an ~90 μm thick layers.

4. Bake the layers for at least 24 hours at 70 C° to evaporate the solvents of SU-8

# VI. Citations

1. Abbott, N. (2002). Astrocyte–endothelial interactions and blood–brain barrier permeability*. *Journal of Anatomy, 200*(6), 629-638. Retrieved from https://academic.microsoft.com/paper/2117691576

2. Abbott, N., Patabendige, A., Dolman, D., Yusof, S., & Begley, D. (2010). Structure and function of the blood–brain barrier. *Neurobiology of Disease, 37*(1), 13-25. Retrieved from https://academic.microsoft.com/paper/2159821105

3. Abdelkader, H., Alani, A., & Alany, R. (2014). Recent advances in non-ionic surfactant vesicles (niosomes): self-assembly, fabrication, characterization, drug delivery applications and limitations. *Drug Delivery, 21*(2), 87-100. Retrieved from https://academic.microsoft.com/paper/2042253098

4. Accardo, A., Blatché, M.-C., Courson, R., Loubinoux, I., Vieu, C., & Malaquin, L. (2018). Two-photon lithography and microscopy of 3D hydrogel scaffolds for neuronal cell growth. *Biomedical Physics & Engineering Express, 4*(2), 27009. Retrieved from https://academic.microsoft.com/paper/2786832617

5. Aekbote, B., Fekete, T., Jacak, J., Vizsnyiczai, G., Ormos, P., & Kelemen, L. (2016). Surface-modified complex SU-8 microstructures for indirect optical manipulation of single cells. *Biomedical Optics Express, 7*(1), 45-56. Retrieved from https://academic.microsoft.com/paper/2184108404

6. Aekbote, B., Jacak, J., Schütz, G., Csányi, E., Szegletes, Z., Ormos, P., & Kelemen, L. (2012). Aminosilane-based functionalization of two-photon polymerized 3D SU-8 microstructures. *European Polymer Journal, 48*(10), 1745-1754. Retrieved from https://academic.microsoft.com/paper/2018525985

7. Aekbote, B., Schubert, F., Ormos, P., & Kelemen, L. (2014). Gold nanoparticle-mediated fluorescence enhancement by two-photon polymerized 3D microstructures. *Optical Materials, 38*, 301-309. Retrieved from https://academic.microsoft.com/paper/2076859948

8. Andrade, M., Leite, F., Rodrigues, L., Ierich, J., Melendez, M., Carvalho, A., . . . Oliveira, O. (2020). A Nanomechanical Genosensor Using Functionalized Cantilevers to Detect the Cancer Biomarkers miRNA-203 and miRNA-205. *IEEE Sensors Journal, 20*(6), 2860-2867. Retrieved from https://academic.microsoft.com/paper/2981667746

9. Arai, Y., Yasuda, R., Akashi, K., Harada, Y., Miyata, H., Kinosita, K., & Itoh, H. (1999). Tying a molecular knot with optical tweezers. *Nature, 399*(6735), 446-448. Retrieved from https://academic.microsoft.com/paper/1525990378

10. Ashkin, A., Dziedzic, J., Bjorkholm, J., & Chu, S. (1986). Observation of a single-beam gradient force optical trap for dielectric particles. *Optics Letters, 11*(5), 288-290. Retrieved from https://academic.microsoft.com/paper/2113372755

11. Bragagni, M., Mennini, N., Ghelardini, C., & Mura, P. (2012). Development and characterization of niosomal formulations of doxorubicin aimed at brain targeting.

*Journal of pharmacy & pharmaceutical sciences : a publication of the Canadian Society for Pharmaceutical Sciences, 15*(1), 184-196. Retrieved from https://academic.microsoft.com/paper/1480859163

12. Brewer, C., Brown, R., & Koenig, S. (1983). Metal Ion Binding and Conformational Transitions in Concanavalin A: A Structure-Function Study. *Journal of Biomolecular Structure & Dynamics, 1*(4), 961-997. Retrieved from https://academic.microsoft.com/paper/2084101844

13. Brouhard, G., Schek, H., & Hunt, A. (2003). Advanced optical tweezers for the study of cellular and molecular biomechanics. *IEEE Transactions on Biomedical Engineering, 50*(1), 121-125. Retrieved from https://academic.microsoft.com/paper/2162657950

14. Busche, J., Starke, G., Knickmeier, S., & Dietzel, A. (2020). Controllable dry adhesion based on two-photon polymerization and replication molding for space debris removal. *Micro and Nano Engineering, 7*, 100052. Retrieved from https://academic.microsoft.com/paper/3014175725

15. Butt, H.-J., & Jaschke, M. (1995). Calculation of thermal noise in atomic force microscopy. *Nanotechnology, 6*(1), 1-7. Retrieved from https://academic.microsoft.com/paper/1974262428

16. Campos-Bedolla, P., Walter, F., Veszelka, S., & Deli, M. (2014). Role of the blood-brain barrier in the nutrition of the central nervous system. *Archives of Medical Research, 45*(8), 610-638. Retrieved from https://academic.microsoft.com/paper/1995304741

17. Carthy, D., Malhotra, M., O'Mahony, A., Cryan, J., & O'Driscoll, C. (2015). Nanoparticles and the blood-brain barrier: advancing from in-vitro models towards therapeutic significance. *Pharmaceutical Research, 32*(4), 1161-1185. Retrieved from https://academic.microsoft.com/paper/2464874208

18. Cecconi, C., Shank, E., Marqusee, S., & Bustamante, C. (2007). Studying protein folding with laser tweezers. *International School of Physics "Enrico Fermi": Protein Folding and Drug Design*, 145-160. Retrieved from https://academic.microsoft.com/paper/2603191233

19. César-Razquin, A., Snijder, B., Frappier-Brinton, T., Isserlin, R., Gyimesi, G., Bai, X., . . . Superti-Furga, G. (2015). A Call for Systematic Research on Solute Carriers. *Cell, 162*(3), 478-487. Retrieved from https://academic.microsoft.com/paper/1820155366

20. Chiou, Y., Lin, H., Tang, M., Lin, H., & Yeh, M. (2013). The influence of physical and physiological cues on atomic force microscopy-based cell stiffness assessment. *PLOS ONE, 8*(10). Retrieved from https://academic.microsoft.com/paper/2056234348

21. Coceano, G., Yousafzai, M., Ma, W., Ndoye, F., Venturelli, L., Hussain, I., . . . Ferrari, E. (2016). Investigation into local cell mechanics by atomic force microscopy mapping and optical tweezer vertical indentation. *Nanotechnology, 27*(6), 65102-65102. Retrieved from https://academic.microsoft.com/paper/2206877308

22. Crump, S. (1989). Apparatus and method for creating three-dimensional objects. Retrieved from https://academic.microsoft.com/paper/1858096020

23. Cumpston, B., Ehrlich, J., Erskin, L., Heikalt, A., Hu, Z.-Y., Leet, I.-Y., . . . Wu, X.-L. (1997). New Photopolymers Based on Two-Photon Absorbing Chromophores and Application to Three-Dimensional Microfabrication and Optical Storage. *MRS Proceedings, 488,* 217-225. Retrieved from https://academic.microsoft.com/paper/2109290256

24. Dy, M.-C., Kanaya, S., & Sugiura, T. (2013). Localized cell stiffness measurement using axial movement of an optically trapped microparticle. *Journal of Biomedical Optics, 18*(11), 111411-111411. Retrieved from https://academic.microsoft.com/paper/2163768098

25. Ebner, A., Hinterdorfer, P., & Gruber, H. (2007). Comparison of different aminofunctionalization strategies for attachment of single antibodies to AFM cantilevers. *Ultramicroscopy, 107*(10), 922-927. Retrieved from https://academic.microsoft.com/paper/1971638410

26. Falleroni, F., Torre, V., & Cojoc, D. (2018). Cell Mechanotransduction With Piconewton Forces Applied by Optical Tweezers. *Frontiers in Cellular Neuroscience, 12*, 130. Retrieved from https://academic.microsoft.com/paper/2802298068

27. Feneberg, W., Aepfelbacher, M., & Sackmann, E. (2004). Microviscoelasticity of the Apical Cell Surface of Human Umbilical Vein Endothelial Cells (HUVEC) within Confluent Monolayers. *Biophysical Journal, 87*(2), 1338-1350. Retrieved from https://academic.microsoft.com/paper/2040360234

28. Finer, J., Simmons, R., & Spudich, J. (1994). Single myosin molecule mechanics: piconewton forces and nanometre steps. *Nature, 368*(6467), 113-119. Retrieved from https://academic.microsoft.com/paper/2059158601

29. Geldenhuys, W., Wehrung, D., Groshev, A., Hirani, A., & Sutariya, V. (2015). Brain-targeted delivery of doxorubicin using glutathione-coated nanoparticles for brain cancers. *Pharmaceutical Development and Technology, 20*(4), 497-506. Retrieved from https://academic.microsoft.com/paper/2139099210

30. Gharbavi, M., Amani, J., Kheiri-Manjili, H., Danafar, H., & Sharafi, A. (2018). Niosome: A Promising Nanocarrier for Natural Drug Delivery through Blood-Brain Barrier. *Advances in Pharmacological Sciences, 2018*, 6847971-6847971. Retrieved from https://academic.microsoft.com/paper/2904990515

31. Gomes, C., Lopes, C., Leitner, M., Ebner, A., Hinterdorfer, P., & Pêgo, A. (2017). Atomic Force Microscopy as a Tool to Assess the Specificity of Targeted Nanoparticles in Biological Models of High Complexity. *Advanced Healthcare Materials, 6*(21), 1700597. Retrieved from https://academic.microsoft.com/paper/2739979995

32. Greenleaf, W., & Block, S. (2006). Single-Molecule, Motion-Based DNA Sequencing Using RNA Polymerase. *Science, 313*(5788), 801-801. Retrieved from https://academic.microsoft.com/paper/1991267416

33. Gross, A., & Bertoldi, K. (2019). Additive Manufacturing of Nanostructures That Are Delicate, Complex, and Smaller than Ever. *Small, 15*(33). Retrieved from https://academic.microsoft.com/paper/2956044442

34. Guck, J., Schinkinger, S., Lincoln, B., Wottawah, F., Ebert, S., Romeyke, M., . . . Bilby, C. (2005). Optical deformability as an inherent cell marker for testing malignant transformation and metastatic competence. *Biophysical Journal, 88*(5), 3689-3698. Retrieved from https://academic.microsoft.com/paper/2006073003

35. Harris, A., & Charras, G. (2011). Experimental validation of atomic force microscopy-based cell elasticity measurements. *Nanotechnology, 22*(34), 345102. Retrieved from https://academic.microsoft.com/paper/2041205033

36. Haseloff, R., Dithmer, S., Winkler, L., Wolburg, H., & Blasig, I. (2015). Transmembrane proteins of the tight junctions at the blood-brain barrier: structural and functional aspects. *Seminars in Cell & Developmental Biology, 38*, 16-25. Retrieved from https://academic.microsoft.com/paper/2079966013

37. Haske, W., Chen, V., Hales, J., Dong, W., Barlow, S., Marder, S., & Perry, J. (2007). 65 nm feature sizes using visible wavelength 3-D multiphoton lithography. *Optics Express, 15*(6), 3426-3436. Retrieved from https://academic.microsoft.com/paper/2019394610

38. Hutter, J., & Bechhoefer, J. (1993). Calibration of atomic-force microscope tips. *Review of Scientific Instruments, 64*(7), 1868-1873. Retrieved from https://academic.microsoft.com/paper/2010227280

39. I. Grexa, T. F. (2020). *Single cell elasticity measurement with an optically actuated micro-robot.* Szeged: Manusricpt under process.

40. Ito, A., Shinkai, M., Honda, H., & Kobayashi, T. (2005). Medical Application of Functionalized Magnetic Nanoparticles. *Journal of Bioscience and Bioengineering, 100*(1), 1-11. Retrieved from https://academic.microsoft.com/paper/2050524601

41. J. Gao, L. G. (2010). Determining the Young's modulus of SU8 negative photoresist through tensile testing for MEMS applications. *Proceedings of SPIE - The International Society for Optical Engineering 7544*.

42. Joshi, M., Pinto, R., Rao, V., & Mukherji, S. (2007). Silanization and antibody immobilization on SU-8. *Applied Surface Science, 253*(6), 3127-3132. Retrieved from https://academic.microsoft.com/paper/2019074222

43. K. C. Neuman, S. M. (2004). Optical Trapping. *Review of Scientific Instruments, 75*, 2787–2809.

44. K. C. Neuman, S. M. (2004). Optical Trapping. *Review of Scientific Instruments*, pp. 2787-2809.

45. Kawata, S., Sun, H.-B., Tanaka, T., & Takada, K. (2001). Finer features for functional microdevices. *Nature, 412*(6848), 697-698. Retrieved from https://academic.microsoft.com/paper/2090572943

46. Kincses, A., Santa-Maria, A., Walter, F., Dér, L., Horányi, N., Lipka, D., . . . Dér, A. (2020). A chip device to determine surface charge properties of confluent cell monolayers by measuring streaming potential. *Lab on a Chip, 20*(20), 3792-3805. Retrieved from https://academic.microsoft.com/paper/3083751983

47. Kodama, H. (1981). Automatic method for fabricating a three-dimensional plastic model with photo-hardening polymer. *Review of Scientific Instruments, 52*(11), 1770-1773. Retrieved from https://academic.microsoft.com/paper/1986517041

48. Kreuter, J. (2014). Drug delivery to the central nervous system by polymeric nanoparticles: what do we know? *Advanced Drug Delivery Reviews, 71*, 2-14. Retrieved from https://academic.microsoft.com/paper/1975495109

49. LaFratta, C., Baldacchini, T., Farrer, R., Fourkas, J., Teich, M., Saleh, B., & Naughton, M. (2004). Replication of Two-Photon-Polymerized Structures with Extremely High Aspect Ratios and Large Overhangs. *Journal of Physical Chemistry B, 108*(31), 11256-11258. Retrieved from https://academic.microsoft.com/paper/2068176475

50. LaFratta, C., Fourkas, J., Baldacchini, T., & Farrer, R. (2007). Cover Picture: Multiphoton Fabrication (Angew. Chem. Int. Ed. 33/2007). *Angewandte Chemie, 46*(33), 6201-6201. Retrieved from https://academic.microsoft.com/paper/2082793166

51. Lamprecht, C., Hinterdorfer, P., & Ebner, A. (2014). Applications of biosensing atomic force microscopy in monitoring drug and nanoparticle delivery. *Expert Opinion on Drug Delivery, 11*(8), 1237-1253. Retrieved from https://academic.microsoft.com/paper/2030309966

52. Lamprecht, C., Plochberger, B., Ruprecht, V., Wieser, S., Rankl, C., Heister, E., . . . Ebner, A. (2014). A single-molecule approach to explore binding, uptake and transport of cancer cell targeting nanotubes. *Nanotechnology, 25*(12), 125704. Retrieved from https://academic.microsoft.com/paper/2103469760

53. Leonardo, R., Ianni, F., & Ruocco, G. (2007). Computer generation of optimal holograms for optical trap arrays. *Optics Express, 15*(4), 1913-1922. Retrieved from https://academic.microsoft.com/paper/1985080845

54. Lim, C., Dao, M., Suresh, S., Sow, C., & Chew, K. (2004). Large deformation of living cells using laser traps. *Acta Materialia, 52*(7), 1837-1845. Retrieved from https://academic.microsoft.com/paper/2156393721

55. Lim, S., Shen, W., & Gao, Z. (2015). Carbon quantum dots and their applications. *Chemical Society Reviews, 44*(1), 362-381. Retrieved from https://academic.microsoft.com/paper/2136693699

56. Lim, Y., McGlashan, S., Cooling, M., & Long, D. (2015). Culture and detection of primary cilia in endothelial cell models. *Cilia, 4*(1), 11-11. Retrieved from https://academic.microsoft.com/paper/2101406974

57. Lockman, P., Koziara, J., Mumper, R., & Allen, D. (2004). Nanoparticle Surface Charges Alter Blood–Brain Barrier Integrity and Permeability. *Journal of Drug*

*Targeting, 12*, 635-641. Retrieved from https://academic.microsoft.com/paper/2020915539

58. Loos, C., Syrovets, T., Musyanovych, A., Mailänder, V., Landfester, K., Nienhaus, G., & Simmet, T. (2014). Functionalized polystyrene nanoparticles as a platform for studying bio–nano interactions. *Beilstein Journal of Nanotechnology, 5*(1), 2403-2412. Retrieved from https://academic.microsoft.com/paper/2168320884

59. Lu, Z., Wu, W., Peng, L., & Wu, L. (2008). Ring opening of α,β-epoxy phenyl ketones with ceric ammonium nitrate (CAN) and potassium bromide. *Canadian Journal of Chemistry, 86*(2), 142-145. Retrieved from https://academic.microsoft.com/paper/2110136916

60. Marino, A., Tricinci, O., Battaglini, M., Filippeschi, C., Mattoli, V., Sinibaldi, E., & Ciofani, G. (2018). A 3D Real-Scale, Biomimetic, and Biohybrid Model of the Blood-Brain Barrier Fabricated through Two-Photon Lithography. *Small, 14*(6), 1702959. Retrieved from https://academic.microsoft.com/paper/2772447408

61. Martínez-Jothar, L., Doulkeridou, S., Schiffelers, R., Torano, J., Oliveira, S., Nostrum, C., & Hennink, W. (2018). Insights into maleimide-thiol conjugation chemistry: Conditions for efficient surface functionalization of nanoparticles for receptor targeting. *Journal of Controlled Release, 282*, 101-109. Retrieved from https://academic.microsoft.com/paper/2790158478

62. Maruo, S., & Inoue, H. (2006). Optically driven micropump produced by three-dimensional two-photon microfabrication. *Applied Physics Letters, 89*(14), 144101. Retrieved from https://academic.microsoft.com/paper/2086807391

63. Masserini, M. (2013). Nanoparticles for brain drug delivery. *International Scholarly Research Notices, 2013*, 238428-238428. Retrieved from https://academic.microsoft.com/paper/2011005493

64. Mathur, A., Collinsworth, A., Reichert, W., Kraus, W., & Truskey, G. (2001). Endothelial, cardiac muscle and skeletal muscle exhibit different viscous and elastic properties as determined by atomic force microscopy. *Journal of Biomechanics, 34*(12), 1545-1553. Retrieved from https://academic.microsoft.com/paper/2042010963

65. McNerney, G., Hübner, W., Chen, B., & Huser, T. (2010). Manipulating CD4+ T cells by optical tweezers for the initiation of cell-cell transfer of HIV-1. *Journal of Biophotonics, 3*(4), 216-223. Retrieved from https://academic.microsoft.com/paper/2107877347

66. Mészáros, M., Porkoláb, G., Kiss, L., Pilbat, A.-M., Kóta, Z., Kupihár, Z., . . . Veszelka, S. (2018). Niosomes decorated with dual ligands targeting brain endothelial transporters increase cargo penetration across the blood-brain barrier. *European Journal of Pharmaceutical Sciences, 123*, 228-240. Retrieved from https://academic.microsoft.com/paper/2883148673

67. Nawaz, S., Sánchez, P., Bodensiek, K., Li, S., Simons, M., & Schaap, I. (2012). Cell visco-elasticity measured with AFM and optical trapping at sub-micrometer

deformations. *PLOS ONE, 7*(9), 45297. Retrieved from https://academic.microsoft.com/paper/2055645719

68. Neuman, K., & Nagy, A. (2008). Single-molecule force spectroscopy: optical tweezers, magnetic tweezers and atomic force microscopy. *Nature Methods, 5*(6), 491-505. Retrieved from https://academic.microsoft.com/paper/2158208080

69. Obata, K., El-Tamer, A., Koch, L., Hinze, U., & Chichkov, B. (2013). High-aspect 3D two-photon polymerization structuring with widened objective working range (WOW-2PP). *Light-Science & Applications, 2*(12). Retrieved from https://academic.microsoft.com/paper/1991036635

70. Oesterhelt, F., Rief, M., & Gaub, H. (1999). Single molecule force spectroscopy by AFM indicates helical structure of poly(ethylene-glycol) in water. *New Journal of Physics, 1*(1), 6-6. Retrieved from https://academic.microsoft.com/paper/2016867898

71. Ohashi, T., Ishii, Y., Ishikawa, Y., Matsumoto, T., & Sato, M. (2002). Experimental and numerical analyses of local mechanical properties measured by atomic force microscopy for sheared endothelial cells. *Bio-medical Materials and Engineering, 12*(3), 319-327. Retrieved from https://academic.microsoft.com/paper/277210135

72. Oliveira, H., Rangl, M., Ebner, A., Mayer, B., Hinterdorfer, P., & Pêgo, A. (2011). Molecular Recognition Force Spectroscopy: A New Tool to Tailor Targeted Nanoparticles. *Small, 7*(9), 1236-1241. Retrieved from https://academic.microsoft.com/paper/2083744321

73. Palima, D., Bañas, A., Vizsnyiczai, G., Kelemen, L., Ormos, P., & Glückstad, J. (2012). Wave-guided optical waveguides. *Optics Express, 20*(3), 2004-2014. Retrieved from https://academic.microsoft.com/paper/2094489954

74. Pesen, D., & Hoh, J. (2005). Micromechanical Architecture of the Endothelial Cell Cortex. *Biophysical Journal, 88*(1), 670-679. Retrieved from https://academic.microsoft.com/paper/2023255019

75. Phillips, D., Gibson, G., Bowman, R., Padgett, M., Hanna, S., Carberry, D., . . . Simpson, S. (2012). An optically actuated surface scanning probe. *Optics Express, 20*(28), 29679-29693. Retrieved from https://academic.microsoft.com/paper/1967860575

76. Piramowicz, M., Czuba, P., Targosz, M., Burda, K., & Szymoński, M. (2006). Dynamic force measurements of avidin-biotin and streptavdin-biotin interactions using AFM. *Acta Biochimica Polonica, 53*(1), 93-100. Retrieved from https://academic.microsoft.com/paper/2037966703

77. Porkoláb, G., Mészáros, M., Tóth, A., Szecskó, A., Harazin, A., Szegletes, Z., . . . Veszelka, S. (2020). Combination of Alanine and Glutathione as Targeting Ligands of Nanoparticles Enhances Cargo Delivery into the Cells of the Neurovascular Unit. *Pharmaceutics, 12*(7), 635. Retrieved from https://academic.microsoft.com/paper/3039157211

78. Prime, K., & Whitesides, G. (1993). Adsorption of proteins onto surfaces containing end-attached oligo(ethylene oxide): a model system using self-assembled monolayers. *Journal of the American Chemical Society, 115*(23), 10714-10721. Retrieved from https://academic.microsoft.com/paper/2024004515

79. Probst, C., Zrazhevskiy, P., Bagalkot, V., & Gao, X. (2013). Quantum dots as a platform for nanoparticle drug delivery vehicle design. *Advanced Drug Delivery Reviews, 65*(5), 703-718. Retrieved from https://academic.microsoft.com/paper/2088779155

80. Radotić, K., Roduit, C., Simonović, J., Hornitschek, P., Fankhauser, C., Mutavdžić, D., . . . Kasas, S. (2012). Atomic force microscopy stiffness tomography on living Arabidopsis thaliana cells reveals the mechanical properties of surface and deep cell-wall layers during growth. *Biophysical Journal, 103*(3), 386-394. Retrieved from https://academic.microsoft.com/paper/2000113865

81. Ricci, D., Nava, M., Zandrini, T., Cerullo, G., Raimondi, M., & Osellame, R. (2017). Scaling-Up Techniques for the Nanofabrication of Cell Culture Substrates via Two-Photon Polymerization for Industrial-Scale Expansion of Stem Cells. *Materials, 10*(1), 66. Retrieved from https://academic.microsoft.com/paper/2576347860

82. Riener, C., Stroh, C., Ebner, A., Klampfl, C., Gall, A., Romanin, C., . . . Gruber, H. (2003). Simple test system for single molecule recognition force microscopy. *Analytica Chimica Acta, 479*(1), 59-75. Retrieved from https://academic.microsoft.com/paper/2037250162

83. Riesenberg, C., Iriarte-Valdez, C., Becker, A., Dienerowitz, M., Heisterkamp, A., Ngezahayo, A., & Torres-Mapa, M. (2020). Probing Ligand-Receptor Interaction in Living Cells Using Force Measurements With Optical Tweezers. *Frontiers in Bioengineering and Biotechnology, 8*, 598459. Retrieved from https://academic.microsoft.com/paper/3100431022

84. Saraiva, C., Praça, C., Ferreira, R., Santos, T., Ferreira, L., & Bernardino, L. (2016). Nanoparticle-mediated brain drug delivery: Overcoming blood-brain barrier to treat neurodegenerative diseases. *Journal of Controlled Release, 235*, 34-47. Retrieved from https://academic.microsoft.com/paper/2395300225

85. Shergill, B., Meloty-Kapella, L., Musse, A., Weinmaster, G., & Botvinick, E. (2012). Optical Tweezers Studies on Notch: Single-Molecule Interaction Strength Is Independent of Ligand Endocytosis. *Developmental Cell, 22*(6), 1313-1320. Retrieved from https://academic.microsoft.com/paper/2078742722

86. Smith, R., Spalding, G., Neale, S., Dholakia, K., & MacDonald, M. (2006). Colloidal traffic in static and dynamic optical lattices. *Society of Photo-Optical Instrumentation Engineers (SPIE) Conference Series*, *6326*. Retrieved from https://academic.microsoft.com/paper/2022878843

87. Smith, S., Cui, Y., & Bustamante, C. (1996). Overstretching B-DNA: The Elastic Response of Individual Double-Stranded and Single-Stranded DNA Molecules. *Science, 271*(5250), 795-799. Retrieved from https://academic.microsoft.com/paper/2081407528

88. Sun, H.-B., Tanaka, T., & Kawata, S. (2002). Three-dimensional focal spots related to two-photon excitation. *Applied Physics Letters, 80*(20), 3673-3675. Retrieved from https://academic.microsoft.com/paper/1994230165

89. T. Fekete, M. M. (2021, August 16). Optically Manipulated Microtools to Measure Adhesion of the Nanoparticle-Targeting Ligand Glutathione to Brain Endothelial Cells. *ACS Applied Materials & Interfaces, 13*, pp. 39018-39029.

90. Tamás Fekete, M. M. (2021, August 16). Optically Manipulated Microtools to Measure Adhesion of the Nanoparticle-Targeting Ligand Glutathione to Brain Endothelial Cells. *ACS Applied Materials & Interfaces, 13*, pp. 39018-39029.

91. Tao, S., Popat, K., & Desai, T. (2006). Off-wafer fabrication and surface modification of asymmetric 3D SU-8 microparticles. *Nature Protocols, 1*(6), 3153-3158. Retrieved from https://academic.microsoft.com/paper/1987413516

92. Tao, S., Popat, K., Norman, J., & Desai, T. (2008). Surface modification of SU-8 for enhanced biofunctionality and nonfouling properties. *Langmuir, 24*(6), 2631-2636. Retrieved from https://academic.microsoft.com/paper/2044792910

93. Teh, W., Dürig, U., Drechsler, U., Smith, C., & Güntherodt, H.-J. (2005). Effect of low numerical-aperture femtosecond two-photon absorption on (SU-8) resist for ultrahigh-aspect-ratio microstereolithography. *Journal of Applied Physics, 97*(5), 54907. Retrieved from https://academic.microsoft.com/paper/1993633645

94. Tihanyi, K., Vastag, M., Balázs, O., Balogh, G., Deli, Duda, E., . . . Veszelka, S. (2018). *Solubility, Delivery and ADME Problems of Drugs and Drug-Candidates.* Retrieved from https://academic.microsoft.com/paper/150573866

95. Tseng, F.-G., Lin, K.-H., Hsu, H.-T., & Chieng, C.-C. (2004). A surface-tension-driven fluidic network for precise enzyme batch-dispensing and glucose detection. *Sensors and Actuators A-physical, 111*(1), 107-117. Retrieved from https://academic.microsoft.com/paper/2163934436

96. Vargas-Pinto, R., Gong, H., Vahabikashi, A., & Johnson, M. (2013). The Effect of the Endothelial Cell Cortex on Atomic Force Microscopy Measurements. *Biophysical Journal, 105*(2), 300-309. Retrieved from https://academic.microsoft.com/paper/2122131535

97. Végh, A., Fazakas, C., Nagy, K., Wilhelm, I., Krizbai, I., Nagyõszi, P., . . . Váró, G. (2011). Spatial and temporal dependence of the cerebral endothelial cells elasticity. *Journal of Molecular Recognition, 24*(3), 422-428. Retrieved from https://academic.microsoft.com/paper/2049635578

98. Végh, A., Fazakas, C., Nagy, K., Wilhelm, I., Molnár, J., Krizbai, I., . . . Váró, G. (2012). Adhesion and stress relaxation forces between melanoma and cerebral endothelial cells. *European Biophysics Journal, 41*(2), 139-145. Retrieved from https://academic.microsoft.com/paper/2081945824

99. Vizsnyiczai, G., Búzás, A., Aekbote, B., Fekete, T., Grexa, I., Ormos, P., & Kelemen, L. (2020). Multiview microscopy of single cells through microstructure-based indirect

optical manipulation. *Biomedical Optics Express, 11*(2), 945-962. Retrieved from https://academic.microsoft.com/paper/2996530635

100.     Vizsnyiczai, G., Frangipane, G., Maggi, C., Saglimbeni, F., Bianchi, S., & Leonardo, R. (2017). Light controlled 3D micromotors powered by bacteria. *Nature Communications, 8*(1), 15974-15974. Retrieved from https://academic.microsoft.com/paper/2728941587

101.     Vizsnyiczai, G., Kelemen, L., & Ormos, P. (2014). Holographic multi-focus 3D two-photon polymerization with real-time calculated holograms. *Optics Express, 22*(20), 24217-24223. Retrieved from https://academic.microsoft.com/paper/2139660001

102.     Vizsnyiczai, G., Lestyán, T., Joniova, J., Aekbote, B., Strejčková, A., Ormos, P., . . . Bánó, G. (2015). Optically Trapped Surface-Enhanced Raman Probes Prepared by Silver Photoreduction to 3D Microstructures. *Langmuir, 31*(36), 10087-10093. Retrieved from https://academic.microsoft.com/paper/1189953203

103.     Vukicevic, S., Kleinman, H., Luyten, F., Roberts, A., Roche, N., & Reddi, A. (1992). Identification of multiple active growth factors in basement membrane matrigel suggests caution in interpretation of cellular activity related to extracellular matrix components. *Experimental Cell Research, 202*(1), 1-8. Retrieved from https://academic.microsoft.com/paper/2048321002

104.     Wang, X., Chen, S., Kong, M., Wang, Z., Costa, K., Li, R., & Sun, D. (2011). Enhanced cell sorting and manipulation with combined optical tweezer and microfluidic chip technologies. *Lab on a Chip, 11*(21), 3656-3662. Retrieved from https://academic.microsoft.com/paper/2017348445

105.     Weksler, B., Subileau, E., Perrière, N., Charneau, P., Holloway, K., Leveque, M., . . . Couraud, P. (2005). Blood-brain barrier-specific properties of a human adult brain endothelial cell line. *The FASEB Journal, 19*(13), 1872-1874. Retrieved from https://academic.microsoft.com/paper/2107798346

106.     Wen, J.-D., Lancaster, L., Hodges, C., Zeri, A.-C., Yoshimura, S., Noller, H., . . . Tinoco, I. (2008). Following translation by single ribosomes one codon at a time. *Nature, 452*(7187), 598-603. Retrieved from https://academic.microsoft.com/paper/2166053360

107.     Wildling, L., Unterauer, B., Zhu, R., Rupprecht, A., Haselgrübler, T., Rankl, C., . . . Gruber, H. (2011). Linking of Sensor Molecules with Amino Groups to Amino-Functionalized AFM Tips. *Bioconjugate Chemistry, 22*(6), 1239-1248. Retrieved from https://academic.microsoft.com/paper/2170737085

108.     Wilmad-LabGlass. (2008). *Proper Cleaning Procedures for NMR Sample Tubes.* Wilmad-LabGlass.

109.     Wollhofen, R., Katzmann, J., Hrelescu, C., Jacak, J., & Klar, T. (2013). 120 nm resolution and 55 nm structure size in STED-lithography. *Optics Express, 21*(9), 10831-10840. Retrieved from https://academic.microsoft.com/paper/2048905346

110.     Woods, S., O'Brien, L., Butcher, W., Preston, J., Georgian, A., Williamson, E., . . . D'Elia, R. (2020). Glucosamine-NISV delivers antibody across the blood-brain barrier: Optimization for treatment of encephalitic viruses. *Journal of Controlled Release, 324*, 644-656. Retrieved from https://academic.microsoft.com/paper/3034021212

111.     Wouters, K., & Puers, R. (2010). Diffusing and swelling in SU-8: insight in material properties and processing. *Journal of Micromechanics and Microengineering, 20*(9), 95013. Retrieved from https://academic.microsoft.com/paper/1977491979

112.     Yeh, P., Zhang, Z., Lin, M., & Cao, X. (2012). Nonfouling Hydrophilic Poly(ethylene glycol) Engraftment Strategy for PDMS/SU-8 Heterogeneous Microfluidic Devices. *Langmuir, 28*(46), 16227-16236. Retrieved from https://academic.microsoft.com/paper/2062142964

113.     Yeh, Y.-C., Creran, B., & Rotello, V. (2012). Gold nanoparticles: preparation, properties, and applications in bionanotechnology. *Nanoscale, 4*(6), 1871-1880. Retrieved from https://academic.microsoft.com/paper/2156769174

*Article*

# Single-Cell Elasticity Measurement with an Optically Actuated Microrobot

**István Grexa [1,2], Tamás Fekete [1,3], Judit Molnár [1], Kinga Molnár [1,4], Gaszton Vizsnyiczai [1], Pál Ormos [1] and Lóránd Kelemen [1,\*]**

[1]  Biological Research Centre, Temesvári krt. 62, 6726 Szeged, Hungary; grexa.istvan@brc.hu (I.G.); fekete.tamas@brc.hu (T.F.); molnartiduj@gmail.com (J.M.); molnar.kinga@brc.hu (K.M.); gaszton@brc.hu (G.V.); ormos.pal@brc.hu (P.O.)
[2]  Doctoral School of Interdisciplinary Medicine, University of Szeged, Korányi fasor 10, 6720 Szeged, Hungary
[3]  Doctoral School of Multidisciplinary Medicine, Dóm tér 9, Hungary University of Szeged, 6720 Szeged, Hungary
[4]  Doctoral School of Theoretical Medicine, University of Szeged, Korányi fasor 10, 6720 Szeged, Hungary
\*  Correspondence: lkelemen@brc.hu; Tel.: +36-62-599-600 (ext. 419)

**Abstract:** A cell elasticity measurement method is introduced that uses polymer microtools actuated by holographic optical tweezers. The microtools were prepared with two-photon polymerization. Their shape enables the approach of the cells in any lateral direction. In the presented case, endothelial cells grown on vertical polymer walls were probed by the tools in a lateral direction. The use of specially shaped microtools prevents the target cells from photodamage that may arise during optical trapping. The position of the tools was recorded simply with video microscopy and analyzed with image processing methods. We critically compare the resulting Young's modulus values to those in the literature obtained by other methods. The application of optical tweezers extends the force range available for cell indentations measurements down to the fN regime. Our approach demonstrates a feasible alternative to the usual vertical indentation experiments.

**Keywords:** cell elasticity; endothelial cells; optical micromanipulation; holographic optical tweezers; two-photon polymerization; image processing

## 1. Introduction

Autonomous microrobots and microactuators have gained attention recently due to their ability to perform complex tasks on biological targets inside microfluidic environments (channels, reservoirs) without the administration of external physical tools. The targets of these manipulations include protein [1], DNA [2], their association [3] or single cells [4,5]. Furthermore, microtools have been developed to control the flow of the solvent that carries these biological objects [6,7] or to characterize their composition [8]. The complexity of microrobots spans from simple microspheres [1,9] to complex tailor-made microstructures [4,10–12], and sometimes a group of such structures is needed to perform specific tasks [13,14]. Most often, these microtools are actuated and guided by optical means, but magnetic [15,16] or acoustic [17] controls are also applied.

Since the size of these microrobots can range from sub-micrometers to a few hundreds of micrometers, they can be easily optimized for the manipulation of single cells. A broad range of tasks can be performed: cells can be actuated with the tools, which includes their simple translation or rotation either on a hard surface [4,5] or in 3D [11,18]; the tools can enhance imaging of cells [12]; the internal structure of the cells can be altered by punching holes in them with the tools [19]; and such microtools have a great potential even in performing cell-to-cell interaction experiments with high precision and selectivity.

In this work, we report on a method that uses tailor-made microtools for the mechanical characterization of single cells. We use optically actuated microtools to make nano-indentations on the cell surface, thereby determining its elastic properties. In order to measure cell membrane elasticity, one needs to realize a small indentation on it with a known radius of curvature of the indenter and a known force; the Young's modulus then can be calculated from the measured indentation and these parameters [20,21]. In the literature, there are many works reporting on the viscoelastic properties of cells measured by atomic force microscopy (AFM). While AFM can perform this task using forces typically higher than 10 pN, the great benefit of optical manipulation is that the achievable forces complete the range of AFM reaching down to even a few tenths of a pN. Optical tweezers have been applied successfully earlier to measure cells' Young's modulus by trapping microbeads of various diameters and pushing them against the cells in an axial direction [20,22–24]. These cell indentation experiments use optical forces of less than 10 pN combined with a larger contact surface radius than a typical AFM tip ($r \approx 1$ μm vs. $r \approx 10$ nm), which allows only small indentations, and consequently only smaller Young's moduli can be measured. The smaller force and larger radius of the indenter enable the optical trap-based methods to give a more precise evaluation of the elasticity of softer cells. It is an additional aspect that in the case of the large indentations of AFM, especially if it is coupled with high indentation rates, not only elasticity but also viscosity contributes to the results [20].

On the other hand, in the arrangement where the movement of the optically actuated bead is perpendicular to the surface supporting the cells and parallel to the optical axis, the measurement of bead position is somewhat less accurate. Further, in these situations, the trapping beam illuminates the bead through the cells themselves with such high intensity that it may pose a risk of photodamage on them [25–27]. Our approach aims to overcome these drawbacks: the microtool is pressed to the cell in a lateral direction, i.e., perpendicular to the optical axis and to the cell surface that allows for measuring its position and therefore the indentations more precisely, and due to the extended shape of the tool, the trapping foci are micrometers away from the living cells under study posing no risk to them. Our microtool has two functional parts: one that interacts with the optical trapping beams and one that consists of the probe that creates the indentation on the cell surface. Its optical actuation was achieved with holographic optical tweezers (HOT) able to move the structure with 6 degrees of freedom (translations and rotations) with a precision of a few tens of nanometers. The tool can be transported anywhere in a microchannel environment and its tip can be oriented towards any lateral direction so the direction of attack can be freely selected. The probe part in the presented experiments was a tip with a few hundreds of nanometers radius, but the fabrication method allows one to freely change the radius above this value. We performed the indentation experiment on adherent endothelial cells that were cultured on a hard vertical surface that is parallel to the optical axis and formed a confluent layer. Our results demonstrate that the microtool-based method provides a Young's modulus that fits in the range reported in the literature on this cell type.

## 2. Materials and Methods

### 2.1. Microtool Design and Fabrication

The microtools, shown in Figure 1, have two functional parts. The first is used to interact with the optical field and consists of four spheres, arranged at the corners of a square with a side length of 14 μm; these spheres are to be trapped with the HOT. The second is the probe part that creates the indentation on the cells surface. This part is a rod of 2 μm length, created in the plane of the spheres 14 μm away from them; we minimized the diameter of its apex for maximal sensitivity. The rods connecting the spheres and the tip formed an X-shape to minimize interference with the optical field and were slightly offset from the plane of the spheres and the tip. This offset ensured that in the recordings of the experiments these rods were out of focus, and therefore did not add extra features to the image processing when determining the precise position of the structure.
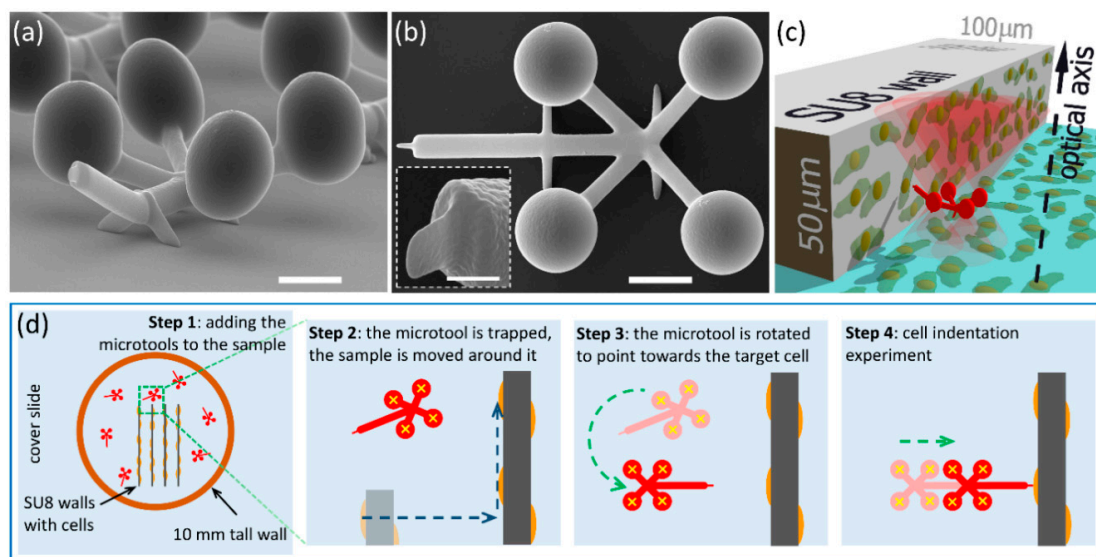
**Figure 1.** The polymerized microtool used for cell indentation experiments and the sample arrangement. Scanning electron microscopic images of the microtools: (**a**) side view and (**b**) top view (scale bars: 5 μm). It is visible that the tip together with the trapping spheres are at a different plane to the rods connecting them. The insert in (**b**) shows the side view of the microtool's tip (scale bar: 1 μm). (**c**) 3D schematic view of the experimental arrangement: cells are grown on a vertical wall polymerized from SU8 as well as on the glass substrate forming a confluent layer; the microtool (red structure) that is trapped and actuated with the optical tweezers (red cones) is approaching the cells on the wall with a translation that is perpendicular to the optical axis of the system. Panel (**d**) illustrates the sample assembly process with the microtools (red structures) after being pipetted into the sample well (Step 1) and their alignment towards the target cell (for details see Section 2.4); yellow crosses mark the trap beam positions, dashed blue arrows indicate sample stage movements (Step 2) and dashed green arrows the optical trap actuations (Steps 3 and 4).

The microtools were made of the photoresist SU-8 (formulation 2007) purchased from Micro Resist Technology GmbH (Berlin, Germany) together with the SU-8 developer (mr-Dev 600, Micro Resist Technology GmbH, Berlin, Germany). Their microfabrication was performed with two-photon polymerization (TPP) with the system described elsewhere [28]. Shortly, the beam of an ultrashort-pulsed laser (C-Fiber A, Menlo Systems GmbH, Martinsried, Germany, $\lambda = 795$ μm, 100 fs pulse length, 100 MHz repetition rate) was focused into a 20 μm thick photoresist layer supported by a microscope cover slide (type #1, 24 mm × 40 mm, Menzel-Glaser, TS Labor Kft, Budapest, Hungary); the focusing objective was a 100X Zeiss Achroplan, oil immersion (NA 1.25, Carl Zeiss Technika Kft, Budaörs, Hungary). The 3D scanning of the focus within the photoresist layer was carried out by a piezo stage (P-124 731.8L and P-721.10, Physik Instrumente GmbH, Karlsruhe, Germany). The illuminated SU-8 layers were processed with the standard protocol: post-exposure bake carried out at 95 °C for 10 min, development in mr-Dev 600 for 5 min 3 times, rinsing in ethanol for 5 min 3 times and finally drying with a stream of nitrogen. The microtools were removed from their support before the experiment by mechanical means in the aqueous solution of 0.5 m/m% bovine serum albumin; they were then pipetted together with this liquid and transferred to the sample containing the cells.

### 2.2. Cell Culturing

The cells were grown on vertical polymer surfaces (walls), which were parallel to the optical axis, as shown in Figure 1c. The walls were polymerized into SU-8 layers of about 50 μm thickness, supported by cover slides (type #1, 24 mm × 40 mm, Menzel-Glaser) using UV mask lithography. The UV light source was the 365 nm line of a mercury lamp (flood exposure source, model 97435, Newport, Irvine, CA, USA, dose: 340 mJ/cm$^2$). The such-created walls were ~5 mm long and 100 μm

wide, positioned at the center of the cover slides. A glass ring of 10 mm height was mounted around the walls using Norland optical adhesive, thereby creating a well for cell culturing. The hCMEC/D3 human microvascular cerebral endothelial cells were grown in this well, which was tilted 45 degrees to promote cell adhesion on the vertical parts of the walls. The cells were cultured in EBM-2 medium (Lonza, Switzerland) supplemented with EGM-2 Bulletkit (Lonza, Basel, Switzerland) and 2.5% fetal bovine serum (Sigma, St. Louis, MO, USA) for 3 days before the indentation experiments. The structures, removed from their support, were pipetted in between these walls into the cell culture medium together with about 5 μL liquid that did not alter the composition of the growth medium significantly. The focused beams (red cones in Figure 1c) for the optical trapping passed into the well through its cover slide support.

### 2.3. HOT Setup

The cell stiffness was measured with the tailor-made microtools described above. The microtools were actuated with a holographic optical trap (HOT) system that can create multiple trapping foci and move them in 3D with high precision, as demonstrated in [12]. In the present experiments, we created 4 trapping foci forming a square of 14 μm side length and moved them with their mutual positions unchanged. The HOT system is built on an inverted Nikon microscope (Eclipse TI, Nikon, Tokyo, Japan) with a continuous-wave fiber laser ($\lambda$ = 1070 nm, THFL-1P400-COL50, BKtel Photonics, Lannion, France) as a light source, an Olympus water immersion objective (UPlanSApo 60X, NA = 1.2) as a focusing element, a motorized microscope stage (ProScan, Prior Scientific, Fulbourn, UK) for sample translation and a spatial light modulator (PLUTO NIR, Holoeye, Berlin, Germany) to generate the multiple traps. The total optical power at the entrance of the objective pupil was 270 mW, which, considering the approximately 50% transmittance of the objective at 1070 nm, resulted in ~34 mW power for each trapping beam. The sample was observed with an EMCCD camera (Rolera EMC2, Qimaging, Surrey, BC, Canada).

### 2.4. Cell Indentation Experiment

The experimental arrangement is depicted in Figure 1c,d. Figure 1c shows the cells grown on the vertical wall polymerized onto a glass substrate, and the microtool approaching the cells in the direction which is perpendicular to the wall surface, to the cells surface and to the optical axis of the trapping objective, and parallel to the supporting glass surface. Figure 1d illustrates the sample assembly and microtool alignment procedure with the cells already present on the SU8 walls. First, the microtools, which were collected from their polymerization glass support, were pipetted into the well containing the cells (see Section 2.2). In the well, the cells were immersed in about 200–300 μL of Leibovitz's L-15 medium (Sigma) that kept them vital without $CO_2$ incubation for the approximately 2-h duration of the experiments. At this stage, the structures were scattered randomly on the bottom of the sample well.

For the measurement of the Young's modulus, the force that pushes the microtool to the target cell and the cell indentation need to be determined. For both values, the tool's position needs to be measured precisely. The force is calculated from the displacement of the microtool relative to the trapping foci. The indentation was determined relative to the case when it is pushed against a hard wall instead of a soft cell. The difference in the movements in these two cases provided the value of indentation, as described below. In both cases, the microtool was translated in a well-controlled manner: after taking hold of it with the optical trap, it was elevated from the substrate to about 5–15 μm above it by defocusing the objective and aligning it with the plane of its four spheres perpendicular to the optical axis. When elevated, the trap stayed fixed relative to the trapping objective and the sample stage was moved until a proper target cell arrived in the field of view (sample movement is shown by the blue dashed arrows on Figure 1d Step 2). Then, with a stationary sample stage, the microtool was rotated towards the target cell by moving the trapping focal spots, until the microtool's tip aligned with the normal of the wall's surface (with or without the cells on it) (Figure 1d Step 3 and Figure 2a,b).

After the microtool was oriented towards the cell, selected upon visual inspection, the cell's silhouette was brought into focus together with the tool's tip by the consecutive adjustments of the focusing objective and the trap position along the optical axis; this ensured that the point of attack on the cell was seen as a sharp contour. Then, the microtool approached the wall to about 2 μm, moving only the microscope stage (rough approach), and stopped. In this moment, the tool was situated at about 5–15 μm height from the supporting glass, which ensured that the trapping foci were only minimally, or not at all distorted by the bottom area of the cell-supporting wall. In step 4, the indentation experiment commenced, when the optical trap was moved in 10 nm steps towards the wall, using only the HOT (fine approach), and at each position a bright-field image of the microtool was recorded; this process resulted in an average speed of 0.05 μm/s. The trajectory of the tip of the microtool was parallel to the normal of the wall. Before making contact with the wall or the cell, the position of the microtool and the trap coincided. When the microtool reached the wall, the movement of the trapping foci continued as before for about an extra 1 μm, but the tool was retarded relative to the trap position. This retardation provides a force by which the microtool is pushed against the wall or the cell surface. Finally, the microtool was retracted and positioned to the next available cell. When more than one indentation experiment was carried out on the same cell, we probed the cell at points that were a few hundreds of nanometers away from each other. Altogether, 19 measurements were carried out on 6 cells with 4 manipulators.
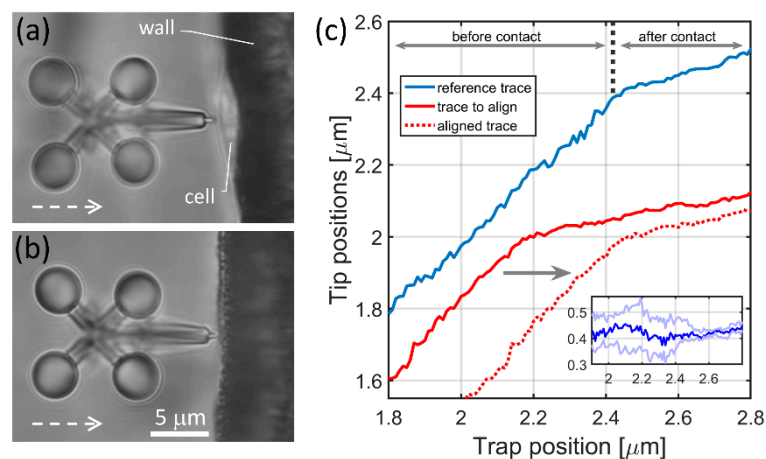


**Figure 2.** Cell indentation experiments and the resulted traces of the microtool's tip. Panels (**a**,**b**) show a typical snapshot of the cell indentation and the wall approaching experiments, respectively; the optical axis is perpendicular to the plane of the figure, the white dashed arrows indicate the direction of the microtool movement during the indentation experiment. The tip position was calculated by determining the positions of the four handle spheres on the image series taken during the indentation experiments. (**c**) shows tip positions from two cell indentation experiments as the function of the trapping beam position (solid blue and solid red traces). It also shows the result of the trace alignment procedure when the red trace is aligned to the blue one with the alignment procedure (dashed red). The inset in (**c**) shows differences of the red and blue traces during the alignment procedure (see main text).

*2.5. Data Analysis*

The position of each microtool during the approach of the cell was determined with a correlation-based method where the reference was its image at the very first position. The script was implemented in Matlab, using built-in image processing and 2D cross-correlation functions. The positions of the four trapping spheres were determined independently. First, a template image was chosen, which was the cropped image of the selected sphere on the very first frame. Then, this reference image was compared to all consecutive frames using Matlab's built-in *normxcorr2* function. This function resulted in a correlation matrix for each frame with the same size as the frame

itself. The maximum of this matrix provides the position on each frame where its similarity to the reference image is the largest; in other words, this maximum is the new position of the sphere on the frame. One must pay attention to the fact that *normxcorr2* provides this position only to one pixel size precision, which was 120 nm in our case. In order to find the position with sub-pixel precision, the values around the correlation matrix maximum value were fitted with a 2D Gaussian function, and the center of this Gaussian gave the new location of the sphere with sub-pixel precision. Next, the position of the microtool's tip was calculated from these sphere position data taking advantage of the fact that the tool is a rigid structure and that it moves in the focal plane. The reason why the image of the tip itself was not monitored is that after it makes a direct contact with the cell, the image becomes distorted and it cannot be used for cross-correlation. At the end of this process, the position of the tip was determined for all the frames and could be plotted as the function of the trap position, which changes between frames by 10 nm.

The precision of the correlation-based position determination method was found to be 5.5 nm FWHM as measured on surface-attached, non-moving microtools. For this, 2000 frames of the surface-attached microtool was recorded and analyzed with the correlation-based method; in theory, the measured positions of the four spheres should not change between frames. In reality, small fluctuations were measured partly due to residual mechanical vibrations and to the imprecision of the calculation of the correlation. The positions of the tip were determined along as well as perpendicular to the direction of the optical trap movement; only those attempts were eventually used in the analysis where the tip movement perpendicular to this direction is negligible (smaller than 50 nm) after the contact.

The result of the image processing is a microtool tip position vs. trapping focus position trace for each indentation experiment. These traces have two distinct ranges as shown in Figure 2c: the first one describes the movement before the contact the microtool makes with its target; in this range, the microtool follows the trap position precisely, so its slope is 1 (reference trace before 2.42 μm in Figure 2c). After the microtool makes contact with its target (a cell, a wall or a bead, see below), it lags behind the trap, so the slope of this range becomes less than 1 (reference trace after 2.42 μm in Figure 2c). Since the contact point did not fall to the same trap position in the consecutive experiments, the traces needed to be aligned. The cell indentation experiment series and the wall approach experiments resulted in two distinct sets of traces. The cell indentation traces were aligned to each other with one alignment procedure, so were the wall approach traces with a separate procedure. In each procedure, a reference trace was selected from the experiments (usually the first one), and the rest of the traces were aligned to it. The alignment was based on calculating the variance of the difference of two traces while one of them (red curve in Figure 2c) was shifted stepwise in respect to the other one that served as a reference (blue curve in Figure 2c) (the step size was 10 nm). The minimum of the calculated variances gave the amount of trace shift used for alignment. The inset in Figure 2c shows three of such difference traces: the dark blue is the case of minimum variance, while the other two have a variance 3 times larger. After aligning the cell and wall approach experiments, the traces from the wall experiments were averaged ($n = 9$), while those of the cell experiments were used individually later to calculate cell indentation and the displacement of the microtool.

### 2.6. Trap Stiffness Calibration

For the calculation of the Young's modulus, the force that the microtool exerted on the cell creating the measured indentation must be known. This force is calculated as the displacement of the microtool from the equilibrium position multiplied by the trap stiffness. The microtool's trap stiffness ($k_m$) was measured with an indirect method. Here, the microtool was pushed against a trapped 9 μm polystyrene bead of known trap stiffness ($k_b$) and the displacement of the microtool was compared to that of the bead (Figure 3). First, $k_b$ was determined by trapping the bead alone using the equation

$$\frac{1}{2}k_B T \; = \; \frac{1}{2}k_b\langle x^2\rangle \tag{1}$$

where $\left\langle x^2 \right\rangle$ is the variance of the bead fluctuation determined by video tracking (using 0.5 ms exposure time), $T$ is room temperature (295K) and $k_B$ is Boltzmann's constant [29]. Then, the microtool was pushed against the trapped bead and the following equation resulted in the trap stiffness of the microtool:

$$k_m = k_b \times \frac{\Delta x_b}{\Delta x_m} \tag{2}$$

where $\Delta x_b$ and $\Delta x_m$ are the displacements of the bead and the microtool, respectively. For this measurement, the tip of the microtool was slightly modified: instead of a sharp tip, it had a flat one; this modification was micrometers away from the trapped spheroids of the tool, so it did not affect the trap stiffness.
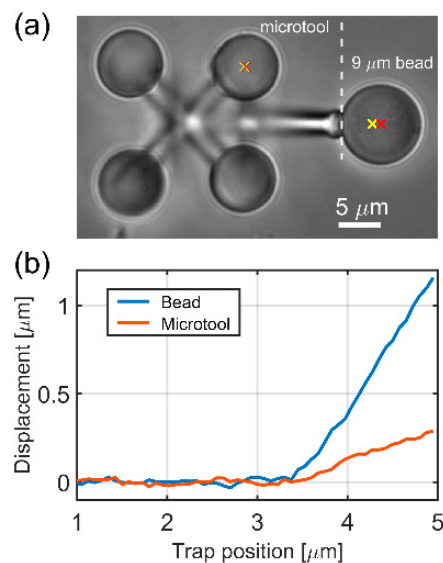


**Figure 3.** Trap stiffness calibration for the cell indenter microtool. Panel (**a**) shows the optical microscopic image of the tool (**left**) and the 9 μm bead (**right**) during the calibration experiment. The yellow crosses show the positions of two optical traps, one holding one of the spheroids of the microtool, the other holding the 9 μm bead. The red crosses show the center of one of the spheroids on the microtool and that of the bead. The distance of the yellow and red crosses gives the displacement values plotted on (**b**).

## 3. Results

An example for the polymerized microtools we used for the cell indentation experiments is shown in Figure 1. The four spheres used to hold the tool with the optical tweezers have 6.5 μm diameter and their centers form a 14 μm × 14 μm square. The apex of its tip has an ellipsoid shape with the smallest radius of 100 nm and a large one of 500 nm; this shape is inherited from the inherent shape of the basic building block of TPP. In our calculations, we take an average radius of 300 nm for the microtool tip. For the trap stiffness measurement, the tip was modified to a 2 μm × 2 μm flat end.

### 3.1. Trap Stiffness Calibration

In Figure 3a, the tip-modified microtool and a 9 μm bead are shown during the stiffness measurement. When the microtool is pushed against the bead in 50 nm steps, both the microtool and the bead are displaced from their equilibrium positions. Since the force that the microtool exerts on the bead and that the bead exerts on the microtool is equal, Equation (2) can be used to calculate $k_m$. Equation (1) resulted in a $k_b$ bead stiffness of 4.5 pN/μm. Figure 3b depicts the averaged bead and microtool displacements as the function of the trap position. From these curves, $k_m$ can be calculated for a range that starts about 0.5 μm after the contact point (between 4 and 5 μm); the obtained microtool stiffness value is 16.49 ± 2 pN/μm.

## 3.2. Endothelial Cells Young's Modulus

The Young's modulus was calculated according to the equation used in the literature for indentation experiments performed with AFM or optical tweezers (Hertz model):

$$F(d_z) = \frac{4E}{3(1-\nu^2)} R_b^{1/2} d_z^{3/2},$$ (3)

where $F$ is the force at which the indenter is pushed against the cell, $E$ is the Young's modulus, $R_b$ is the radius of the indenter surface, $d_z$ is the indentation and $\nu$ is the Poisson number (we chose 0.5) [21,22]. The indentations and the forces (in the form of displacement) were calculated from the microtool position traces as the function of the trap positions. Figure 4a shows representative raw microtool tip positions during the cell indentation experiments before their alignment. The individual traces illustrate that the microtools' movement changes radically after they made contact with the cells: they do not follow the movement of the trap but do not stop completely either. After the contact, the movement continues to be primarily a linear function of the trap position for at least another 500–800 nm of trap movement; in this regime, the tip moves less than 150 nm. In a few cases, the tip position suddenly increased after about 100 nm tip travel due to an occasional sideway slip on the cell membrane. Figure 4b shows one aligned tip position trace when pushed against a cell (green curve) and the average of the traces from the approaches of the hard SU8 walls (red curve). The tip position is meaningful mainly in the first 400 nm beyond the contact point, where only negligible slipping took place. In the case of the hard wall, the tips usually do not stop completely but a residual forward movement remains, which is due to the small sideway movements of the tip on the surface. We believe that these small slips also took place for the cell experiments, so the extra average forward movement observed at the walls was used as a "baseline" in the cell indentation experiments: the tip positions from the cell experiments were compared to this baseline. Figure 4c shows a typical experimental result of an approach of the hard wall. It is visible that the tip continued to move forward about 20 nm during the first 400 nm of trap position movement after the contact (between 2.43 and 2.83 μm), while it slipped sideways at an average of 50 nm.
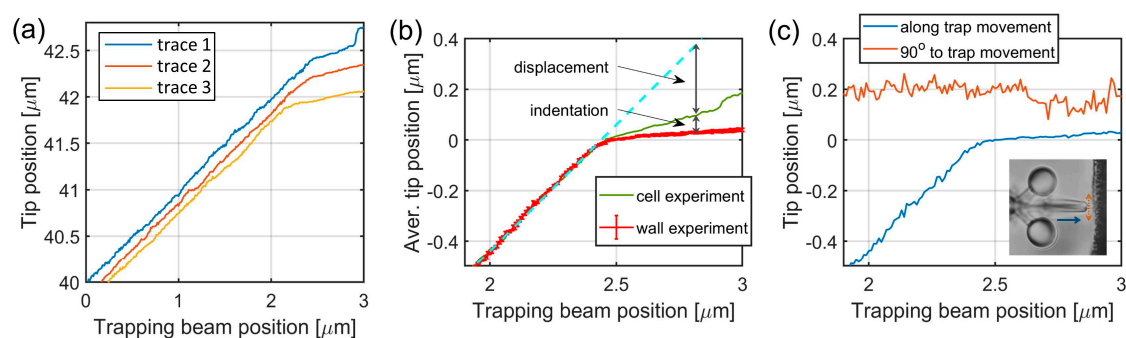


**Figure 4.** Tip position traces for the calculation of endothelial cell's Young's modulus. Panel (**a**) shows representative raw tip position traces as the function of the trap positions, before alignment, obtained from individual cell indentation experiments. After the alignment procedure, the tip positions (**b**) of the wall approach experiments were averaged for background (red curve), while the cell indentation traces (an example is shown by the green curve) were used individually to calculate indentation and displacement. The error bars on the red trace represent standard deviation. At each trapping beam position, the cell indentation was calculated as the difference between the green and red curves, and the microtool displacement as the difference between the green curve and the trapping beam position (dashed light blue curve). Panel (**c**) shows a tip position movement parallel (blue) and perpendicular (red) to the trap movement (that is, axis of the microtool) during the tool being pushed against a hard wall. The inset displays the tip movement along the trap progression (blue line) and perpendicular to it (red line).

The two position traces illustrated in Figure 4b were used to calculate the indentation and force values used in the Hertz model for each individual cell indentation experiment. The indentation is simply the difference between the tip positions when approaching the cell and when approaching the wall. The displacement was calculated by first fitting a straight line to the initial part of the cell approach trace (light blue dashed line in Figure 4b) and then taking the difference between this line and the tip position after the contact point. Figure 5a shows these two values, the cell indentation and the microtool displacement as the function of the trap position. The applied force is calculated from the displacement by multiplying it by the trap stiffness $k_m$. The displacement resulted in a force ranging from 1 to 5 pN, which is below the precision of an AFM. Both traces have a break at the contact point between 2.4 and 2.5 μm, but produce a large error of about 400 nm after the contact point. The displacement and indentation values can be measured reliably in the trap position range of 2.5–2.9 μm, therefore the Young's modulus can be regarded as reliable also only here. We obtained values ranging from about 220 up to about 1500 Pa (Figure 5b), although between the 2.5 and 2.6 μm trap positions (corresponding indentation: between 0.01 and 0.02 μm), the values could be determined with significant noise.
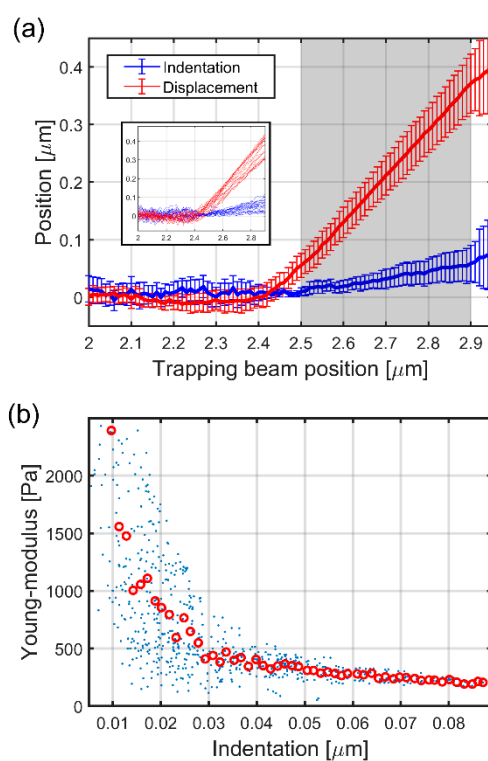


**Figure 5.** The measured indentation and displacement data and the Young's modulus calculated from them. The indentation (blue line) and displacement (red line) data on panel (**a**) are calculated from the aligned traces of the 19 cell indentation experiments as shown in Figure 4b; the error bars represent standard deviation. The shaded area highlights the reliable range for the two quantities. The inset shows the individual displacement traces (red) and indentation traces (blue) calculated separately for the 19 experiments. The Young's modulus as the function of indentation over the values highlighted in (**a**) is shown in panel (**b**). The blue dots represent all of the approximately 800 individual point pairs (40 trap positions × 19 experiments), while the red circles are their averages in 60 regions over the 0–0.09 μm indentation range.

## 4. Discussion

We have designed an optical tweezers-operated microtool specifically to measure the elasticity of adherent cells in closed microfluidic environments. In contrast to earlier optical trap-based cell indentation experiments, this tool approaches the target cells laterally which makes the determination

of its position easier even with simple bright-field video microscopy. In addition, in the trapped parts of the structures, the four spheroids are more than ten micrometers away from the probe tip, which ensures that the optical field does not cause photodamage to the cells. The analysis of the microtools' position during the indentation experiments revealed that they move in a straight and continuous way after making contact with the cell, and their position values yield the indentation and pushing force values in a straightforward manner. The sideways slip of the microtools' tip in contact with the cells could be readily detected and excluded from the evaluation based on its magnitude. Residual sideways tip movements could be compensated for with a control measurement using a hard wall without cells. The microtools were characterized with 16.5 pN/μm trap stiffness and pushing force in the 1–5 pN range, comparable to other optical trap-based elasticity measurements but well below that of an AFM. This force together with the 300 nm tip radius of the microtool yielded the measured indentation values of up to 90 nm. The operating force range can be easily extended to higher values with higher trapping laser power and smaller trapping sphere diameters.

We obtained Young's moduli in the range between 220 and 1500 Pa, depending upon the position of the trapping beam, consequently on the amount of indentation; the noise of the Young's modulus, however, remarkably increases with the decrease in the indentation. These values are comparable to those measured by AFM on bovine aortic endothelial cells (700–2.7 kPa [30]), on pulmonary artery endothelial cells (400–1500 Pa [31]), on human umbilical vein endothelial cells (HUVEC) (350–4000 Pa [21]) or by magnetic tweezers on HUVEC (400 Pa [32]). It is noticeable that the values for the AFM-derived Young's modulus can easily vary an order of magnitude across the literature for the same type of cell. For endothelial cells, values anywhere from ~200 to ~5000 Pa can be found; our measured Young's modulus falls to the lower regime with a few hundred Pa. The main reasons for this broad range can be found in the measurement conditions: mainly in the rate and amount of indentation, and in the shape of the object the indentation is realized with.

It was shown that increasing the indentation rate increases the apparent Young's modulus due primarily to viscous effects [20,33]. The typical loading rates used in an AFM measurement span from 100 pN/s [20] to tens [33] or hundreds of nN/s values (exerting 1 nN force with 0.5 kHz frequency of the AFM cantilever [34]). Our optical tweezers approach experiment lasts about 60 s, where during only the last 5–6 s does the tip actually hit the cell. Considering the averaged maximum of 60 nm indentation and that by the end of this period the force increases to an average of 6 pN, it yields an indentation rate as low as 0.01 μm/s and a loading rate of about 1 pN/s, which is orders of magnitude smaller than those of AFM. For Mathur and co-workers, the lower limit for viscous dissipation was at 0.25 μm/s probe velocity [33]. We are confident that at the observed low-indentation rate viscous effects do not play any role in measuring the Young's modulus in our experiments.

In the papers of Vargas-Pinto and Mathur [21,33], the authors also showed that the higher the indentation, the lower the Young's modulus, similarly to our results (Figure 5b). The amount of indentation, which for us was up to 90 nm, is in the lower regime of what was obtained with AFM or optical tweezers [21,24]; it is very likely that with this low value, we mainly measure the elastic properties of the cell membrane and not the complex characteristics of the underlying actin network. The measurement error of Young's modulus increases significantly below 30 nm indentation. It is believed that this noise is primarily due to thermal fluctuations and the increase in the relative error when using small indentation and force values in Equation (3). However, the larger $E$ for lower indentations is elsewhere argued to originate from the nonlinear elasticity of the cell [33]; it is beyond the scope of this paper to study the nonlinear phenomenon in detail. The third important parameter is the shape of the intender. Vargas-Pinto et al. reported on using AFM tips with radii of curvature from 20 nm to 5 μm for endothelial cell indentation [21]. They found that while the sharp tip yielded a value of 3.8 kPa for the Young's modulus, the 5 μm one yielded only 350 Pa for the same type of cell. Similarly, Harris and co-workers found that pyramidal sharp tips can measure double the Young's modulus of that measured with spherical ($r = 7.5$ μm) tips (800 vs. 400 Pa) on MDCK cells [35]. Chiou and co-workers also observed a more than two-fold increase in the Young's modulus value for

mouse fibroblast cells when they compared sharp pyramidal tips with flat top (diameter of 1.8 μm) and spherical (sphere $r$ = 2.5 μm) tips [36]. The tip of our microtool has a radius of 300 nm on average, which is much larger than that of the conical AFM ($r \approx 10$ nm) tips and comparable to those used for optical tweezers indentation ($r$ = 0.4–1.5 μm); this size also points towards measuring Young's moduli in the lower few hundreds of the Pa regime with our microtool.

In conclusion, the measurement of a cell's Young's modulus requires a careful approach in order to obtain reliable results. Even with one technique, one can measure very different values depending on the measurement parameters. The solution probably lies in what one actually wants to measure. If one is interested in the pure linear elastic properties of the cell, it is believed that the use of large radius of curvature indentation surfaces, small indentations (with small forces) and small loading rates is more appropriate to characterize specifically that. Optically micro-manipulated polymer structures should ideally operate in this regime.

**Conflicts of Interest:** The authors declare no conflict of interest.

## References

1. Chen, H.; Chandrasekar, S.; Sheetz, M.P.; Stossel, T.P.; Nakamura, F.; Yan, J. Mechanical perturbation of filamin A immunoglobulin repeats 20-21 reveals potential non-equilibrium mechanochemical partner binding function. *Sci. Rep.* **2013**, *3*, 1642. [CrossRef] [PubMed]

2. Oroszi, L.; Galajda, P.; Kirei, H.; Bottka, S.; Ormos, P. Direct measurement of torque in an optical trap and its application to double-strand DNA. *Phys. Rev. Lett.* **2006**, *97*, 058301. [CrossRef] [PubMed]

3. Simons, M.; Pollard, M.R.; Hughes, C.D.; Ward, A.D.; Van Houten, B.; Towrie, M.; Botchway, S.W.; Parker, A.W.; Kad, N.M. Directly interrogating single quantum dot labelled UvrA2 molecules on DNA tightropes using an optically trapped nanoprobe. *Sci. Rep.* **2015**, *5*, 18486. [CrossRef] [PubMed]

4. Aekbote, B.L.; Fekete, T.; Jacak, J.; Vizsnyiczai, G.; Ormos, P.; Kelemen, L. Surface-modified complex SU-8 microstructures for indirect optical manipulation of single cells. *Biomed. Opt. Express* **2016**, *7*, 45–56. [CrossRef] [PubMed]

5. Hu, S.; Xie, H.; Wei, T.; Chen, S.; Sun, D. Automated Indirect Transportation of Biological Cells with Optical Tweezers and a 3D Printed Microtool. *Appl. Sci.* **2019**, *9*, 2883. [CrossRef]

6. Maruo, S.; Takaura, A.; Saito, Y. Optically driven micropump with a twin spiral microrotor. *Opt. Express* **2009**, *17*, 18525–18532. [CrossRef]

7. Terray, A.; Oakey, J.; Marr, D.W.M. Microfluidic Control Using Colloidal Devices. *Science* **2002**, *296*, 1841–1844. [CrossRef]

8. Vizsnyiczai, G.; Lestyan, T.; Joniova, J.; Aekbote, B.L.; Strejckova, A.; Ormos, P.; Miskovsky, P.; Kelemen, L.; Bano, G. Optically Trapped Surface-Enhanced Raman Probes Prepared by Silver Photoreduction to 3D Microstructures. *Langmuir* **2015**, *31*, 10087–10093. [CrossRef]

9. Mártonfalvi, Z.; Bianco, P.; Naftz, K.; Ferenczy, G.G.; Kellermayer, M. Force generation by titin folding. *Protein Sci.* **2017**, *26*, 1380–1390. [CrossRef]

10. Barbot, A.; Decanini, D.; Hwang, G. On-chip Microfluidic Multimodal Swimmer toward 3D Navigation. *Sci. Rep.* **2016**, *6*, 19041. [CrossRef]

11. Vizsnyiczai, G.; Aekbote, B.L.; Buzas, A.; Grexa, I.; Ormos, P.; Kelemen, L. High accuracy indirect optical manipulation of live cells with functionalized microtools. In *Optical Trapping and Optical Micromanipulation Xiii*; Dholakia, K., Spalding, G.C., Eds.; SPIE: Bellingham, WA, USA, 2016; Volume 9922, p. 992216.

12. Vizsnyiczai, G.; Búzás, A.; Lakshmanrao Aekbote, B.; Fekete, T.; Grexa, I.; Ormos, P.; Kelemen, L. Multiview microscopy of single cells through microstructure-based indirect optical manipulation. *Biomed. Opt. Express* **2020**, *11*, 945–962. [CrossRef] [PubMed]

13. Būtaitė, U.G.; Gibson, G.M.; Ho, Y.-L.D.; Taverne, M.; Taylor, J.M.; Phillips, D.B. Indirect optical trapping using light driven micro-rotors for reconfigurable hydrodynamic manipulation. *Nat. Commun.* **2019**, *10*, 1215. [CrossRef] [PubMed]

14. Turlier, H.; Fedosov, D.A.; Audoly, B.; Auth, T.; Gov, N.S.; Sykes, C.; Joanny, J.F.; Gompper, G.; Betz, T. Equilibrium physics breakdown reveals the active nature of red blood cell flickering. *Nat. Phys.* **2016**, *12*, 513. [CrossRef]

15. Bente, K.; Codutti, A.; Bachmann, F.; Faivre, D. Biohybrid and Bioinspired Magnetic Microswimmers. *Small* **2018**, *14*, 1704374. [CrossRef] [PubMed]

16. Sarkar, R.; Rybenkov, V.V. A Guide to Magnetic Tweezers and Their Applications. *Front. Phys.* **2016**, *4*. [CrossRef]

17. Sitters, G.; Kamsma, D.; Thalhammer, G.; Ritsch-Marte, M.; Peterman, E.J.G.; Wuite, G.J.L. Acoustic force spectroscopy. *Nat. Methods* **2015**, *12*, 47–50. [CrossRef]

18. Shishkin, I.; Markovich, H.; Roichman, Y.; Ginzburg, P. Auxiliary Optomechanical Tools for 3D Cell Manipulation. *Micromachines* **2020**, *11*, 90. [CrossRef]

19. Hayakawa, T.; Fukada, S.; Arai, F. Fabrication of an On-Chip Nanorobot Integrating Functional Nanomaterials for Single-Cell Punctures. *IEEE Trans. Robot.* **2014**, *30*, 59–67. [CrossRef]

20. Nawaz, S.; Sanchez, P.; Bodensiek, K.; Li, S.; Simons, M.; Schaap, I.A.T. Cell Visco-Elasticity Measured with AFM and Optical Trapping at Sub-Micrometer Deformations. *PLoS ONE* **2012**, *7*, e45297. [CrossRef]

21. Vargas-Pinto, R.; Gong, H.; Vahabikashi, A.; Johnson, M. The Effect of the Endothelial Cell Cortex on Atomic Force Microscopy Measurements. *Biophys. J.* **2013**, *105*, 300–309. [CrossRef]

22. Dy, M.C.; Kanaya, S.; Sugiura, T. Localized cell stiffness measurement using axial movement of an optically trapped microparticle. *J. Biomed. Opt.* **2013**, *18*. [CrossRef] [PubMed]

23. Ndoye, F.; Yousafzai, M.S.; Coceano, G.; Bonin, S.; Scoles, G.; Ka, O.; Niemela, J.; Cojoc, D. The influence of lateral forces on the cell stiffness measurement by optical tweezers vertical indentation. *Int. J. Optomechatron.* **2016**, *10*, 53–62. [CrossRef]

24. Yousafzai, M.S.; Coceano, G.; Mariutti, A.; Ndoye, F.; Amin, L.; Niemela, J.; Bonin, S.; Scoles, G.; Cojoc, D. Effect of neighboring cells on cell stiffness measured by optical tweezers indentation. *J. Biomed. Opt.* **2016**, *21*, 57004. [CrossRef] [PubMed]

25. Ayano, S.; Wakamoto, Y.; Yamashita, S.; Yasuda, K. Quantitative measurement of damage caused by 1064-nm wavelength optical trapping of Escherichia coli cells using on-chip single cell cultivation system. *Biochem. Biophys. Res. Commun.* **2006**, *350*, 678–684. [CrossRef] [PubMed]

26. Liang, H.; Vu, K.T.; Krishnan, P.; Trang, T.C.; Shin, D.; Kimel, S.; Berns, M.W. Wavelength dependence of cell cloning efficiency after optical trapping. *Biophys. J.* **1996**, *70*, 1529–1533. [CrossRef]

27. Rasmussen, M.B.; Oddershede, L.B.; Siegumfeldt, H. Optical tweezers cause physiological damage to Escherichia coli and Listeria bacteria. *Appl. Environ. Microbiol.* **2008**, *74*, 2441–2446. [CrossRef] [PubMed]

28. Vizsnyiczai, G.; Kelemen, L.; Ormos, P. Holographic multi-focus 3D two-photon polymerization with real-time calculated holograms. *Opt. Express* **2014**, *22*, 24217–24223. [CrossRef] [PubMed]

29. Neuman, K.C.; Block, S.M. Optical trapping. *Rev. Sci. Instrum.* **2004**, *75*, 2787–2809. [CrossRef]

30. Ohashi, T.; Ishii, Y.; Ishikawa, Y.; Matsumoto, T.; Sato, M. Experimental and numerical analyses of local mechanical properties measured by atomic force microscopy for sheared endothelial cells. *Bio-Med. Mater. Eng.* **2002**, *12*, 319–327.

31. Pesen, D.; Hoh, J.H. Micromechanical Architecture of the Endothelial Cell Cortex. *Biophys. J.* **2005**, *88*, 670–679. [CrossRef]

32. Feneberg, W.; Aepfelbacher, M.; Sackmann, E. Microviscoelasticity of the Apical Cell Surface of Human Umbilical Vein Endothelial Cells (HUVEC) within Confluent Monolayers. *Biophys. J.* **2004**, *87*, 1338–1350. [CrossRef] [PubMed]

33. Mathur, A.B.; Collinsworth, A.M.; Reichert, W.M.; Kraus, W.E.; Truskey, G.A. Endothelial, cardiac muscle and skeletal muscle exhibit different viscous and elastic properties as determined by atomic force microscopy. *J. Biomech.* **2001**, *34*, 1545–1553. [CrossRef]

34. Coceano, G.; Yousafzai, M.S.; Ma, W.; Ndoye, F.; Venturelli, L.; Hussain, I.; Bonin, S.; Niemela, J.; Scoles, G.; Cojoc, D.; et al. Investigation into local cell mechanics by atomic force microscopy mapping and optical tweezer vertical indentation. *Nanotechnology* **2016**, *27*, 065102. [CrossRef] [PubMed]

35. Harris, A.R.; Charras, G.T. Experimental validation of atomic force microscopy-based cell elasticity measurements. *Nanotechnology* **2011**, *22*, 345102. [CrossRef]

36. Chiou, Y.W.; Lin, H.K.; Tang, M.J.; Lin, H.H.; Yeh, M.L. The Influence of Physical and Physiological Cues on Atomic Force Microscopy-Based Cell Stiffness Assessment. *PLoS ONE* **2013**, *8*. [CrossRef]

# Optically Manipulated Microtools to Measure Adhesion of the Nanoparticle-Targeting Ligand Glutathione to Brain Endothelial Cells

Tamás Fekete,*,§ Mária Mészáros,§ Zsolt Szegletes, Gaszton Vizsnyiczai, László Zimányi, Mária A. Deli, Szilvia Veszelka,* and Lóránd Kelemen*

ACCESS | Metrics & More | Article Recommendations | SI Supporting Information

**ABSTRACT:** Targeting nanoparticles as drug delivery platforms is crucial to facilitate their cellular entry. Docking of nanoparticles by targeting ligands on cell membranes is the first step for the initiation of cellular uptake. As a model system, we studied brain microvascular endothelial cells, which form the anatomical basis of the blood–brain barrier, and the tripeptide glutathione, one of the most effective targeting ligands of nanoparticles to cross the blood–brain barrier. To investigate this initial docking step between glutathione and the membrane of living brain endothelial cells, we applied our recently developed innovative optical method. We present a microtool, with a task-specific geometry used as a probe, actuated by multifocus optical tweezers to characterize the adhesion probability and strength of glutathione-coated surfaces to the cell membrane of endothelial cells. The binding probability of the glutathione-coated surface and the adhesion force between the microtool and cell membrane was measured in a novel arrangement: cells were cultured on a vertical polymer wall and the mechanical forces were generated laterally and at the same time, perpendicularly to the plasma membrane. The adhesion force values were also determined with more conventional atomic force microscopy (AFM) measurements using functionalized colloidal probes. The optical trapping-based method was found to be suitable to measure very low adhesion forces ($\leq 20$ pN) without a high level of noise, which is characteristic for AFM measurements in this range. The holographic optical tweezers-directed functionalized microtools may help characterize the adhesion step of nanoparticles initiating transcytosis and select ligands to target nanoparticles.

**KEYWORDS:** functionalized microtool, optical tweezers, targeted nanoparticle, brain endothelial cell, atomic force microscopy, adhesion force, live cell measurements
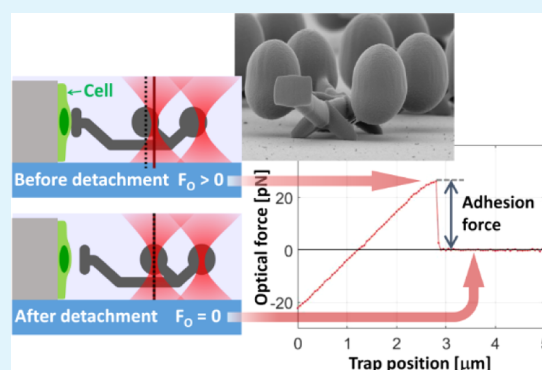
## INTRODUCTION

Functionalization of nanoparticles (NPs) with targeting ligands is crucial to facilitate the tissue/organ-specific cellular entry of these novel drug delivery platforms.[1] Functionalized nanocarriers are also protected against removal from the circulation by the kidneys and the reticuloendothelial system of the liver and spleen.[2] The blood–brain barrier (BBB) is the major obstacle that prevents potential neuropharmaceuticals to reach their targets in the central nervous system.[3] Thus, designing targeted NPs to increase the brain entry of drugs across the BBB, called as Trojan horse mechanism, was the main focus of NP research in the last decade.[4] A wide variety of ligands or antibodies specific to BBB receptors[5−9] or carriers[10−13] were tested on cell culture models and in animals as promising targeting molecules to elevate the efficiency of BBB crossing. Among them, the tripeptide glutathione (GSH) is one of the most successful BBB-specific targeting ligands.[14] The transporter(s) of GSH at the brain microvasculature has not been

identified; it is assumed that it belongs to sodium-dependent carrier-mediated transport systems.[14] Liposomes targeted with glutathione attached to a polyethylene glycol linker (PEG-GSH) and loaded with doxorubicin[15,16] and methylprednisolone[17] have been tested in pilot clinical studies.

Targeting ligands initialize the docking of NPs to the cell surface, which is the first step of the endocytic mechanisms.[18] Docking of NPs to the membrane of cells initiates dynamic physicochemical interactions between the NPs and the cells.[19] The adhesion of the targeting molecules on the surface of NPs to their specific cellular receptors or carriers leads to

conformational changes and invaginations in the plasma membrane. These will lead to the formation of clathrin-, caveolin-, or noncoated vesicles that help NPs enter the cells via different endocytic pathways.[20] The intracellular fate of NPs will be determined by several biological factors and will ultimately lead to (retrograde) exocytosis, degradation in lysosomes, or transcytosis.[21,22] Therefore, characterization of this adhesion step is important for understanding how the transcytosis of NPs begins, and measurements of this initial docking can be novel tools to select ligands to target NPs.

The force that builds up during the adhesion step depends on the type and properties of targeting ligands and the characteristics of their interactions with their plasma membrane receptors.[23,24] The interaction between the NP-targeting ligand and the cells is classically characterized with atomic force microscopy (AFM).[25] Here, either the AFM tip itself (sharp or large diameter spherical) is labeled with the targeting molecule, or functionalized NPs are attached to the tip and adhesion is measured between the cell surface and the functionalized tip. For targeted NPs, molecular recognition force spectroscopy provides a tool to characterize the effect of ligand type and density on the adhesion probability and unbinding force between the targeted NPs and cells.[25] In general, the binding force between the ligand or targeted NPs and the cells measured by AFM is in the range of 20−60 pN.[26−28] It must be noted that the sensitivity of the AFM technique limits it to measure forces above ~10 pN,[29] which makes the force values close to this range less reliable and the ones below it unmeasurable.

An optical trap (OT), on the other hand, can measure forces in the 0.1−100 pN range with great accuracy,[30] thus completing the force range of AFM and allowing to observe weaker interactions. OT has become an important tool in single-cell studies, and various measurement arrangements are used. The membrane properties of surface-adhered cells are commonly probed with microbeads actuated with optical tweezers in an axial direction since the apical membrane is perpendicular to the optical axis of the system when the cells are cultured on a glass substrate.[31−33] The optical forces, however, are about a factor of 5 times smaller in the axial direction than in the lateral direction.[30] Recently, we introduced an alternative arrangement to probe cell elasticity using task-specific complex microtools prepared by the technique of two-photon polymerization and actuated by holographic optical tweezers (HOT).[34] The new experimental arrangement enabled us to measure mechanical forces acting on cultured live cells perpendicular to the cell membrane but with the optical probe moving perpendicular to the optical axis. The cells in this arrangement were grown on walls with surfaces parallel to the optical axis (vertical walls) enabling their approach in a lateral direction (Figure 1). The method allows exerting higher optical force on the probe and a more accurate position determination. Furthermore, using micro-tools, we can keep the potentially harmful intense trapping beam even tens of micrometers away from the probed cells, a distance much larger than with microbeads. We successfully used this arrangement to probe endothelial cell stiffness and obtained Young's modulus values comparable to those measured with AFM and axially executed OT measurements.

Here, we report the application of this method to study the adhesion force between brain endothelial cells and GSH, a reference targeting ligand of vesicular NPs. We characterized the binding of glutathione to living brain endothelial cells with
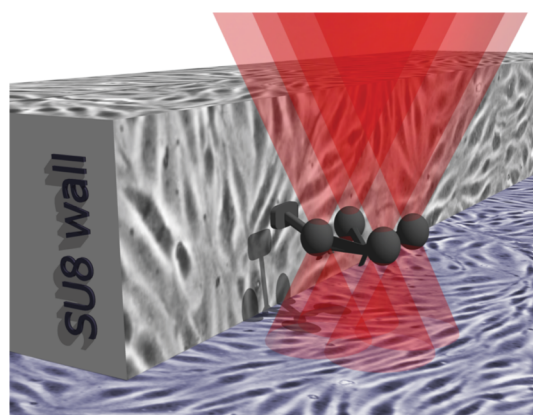


**Figure 1.** Schematic drawing of a novel method to measure the adhesion force between living brain endothelial cells and artificial surfaces of nanoparticles functionalized with the targeting ligand. The cells are grown on the walls of a block polymerized out of SU-8 photoresist. The microtool (dark-gray structure) held and translated with multibeam optical tweezers (represented as red cones) probes the cells situated on the vertical walls. The axes of the cones are parallel to the optical axis of the system.

GSH-coated polymer microtools. We measured the binding probability and the adhesion forces of functionalized micro-structures to cultured human and rat brain endothelial cells. We compared the results of the OT-based technique with AFM measurements and found that the observed values are in accordance with the force ranges reported in the literature for ligand−receptor interactions.

## ■ RESULTS AND DISCUSSIONS

Based on our recently developed optical tweezers method, the major aims of this study were (i) to directly measure and characterize the specific adhesion forces between the targeting ligand GSH and the membrane of living brain capillary endothelial cells via optically actuated microtools and (ii) to compare the HOT method with AFM measurements. To complement the biophysical measurements and validate the efficiency of NP targeting, we also tested the uptake of NPs labeled with PEG-GSH or PEG linker on cultured brain endothelial cells.

**Uptake of Targeted Vesicular Nanoparticles.** We prepared vesicular nanoparticles, the so-called niosomes, from nonionic surfactants and cholesterol as detailed in our previous investigations.[11,12] Niosomes are biodegradable, stable, and nonexpensive vesicular NPs with versatile applications.[35] Niosomes were functionalized with PEG-GSH as a targeting ligand (Figure 2a). The PEG linker was used in the control group. The cargo of the NPs was a fluorescent biomolecule, bovine serum albumin labeled with Evans blue dye (EBA; 67 kDa). The average diameters of the nanovesicles were 100.97 and 122.80 nm for the control (N-PEG) and targeted (N-PEG-GSH) groups, respectively. We measured a relatively narrow size distribution by dynamic light scattering, indicated by polydispersity index values below 0.18 in both groups (Figure 2b). The zeta potential (characterizing the surface charge density) of both groups was slightly negative, with N-PEG-GSH nanovesicles displaying a more negative value (−6.19 mV). These data indicate that our niosomes have optimal physicochemical properties to facilitate brain drug delivery.[36]
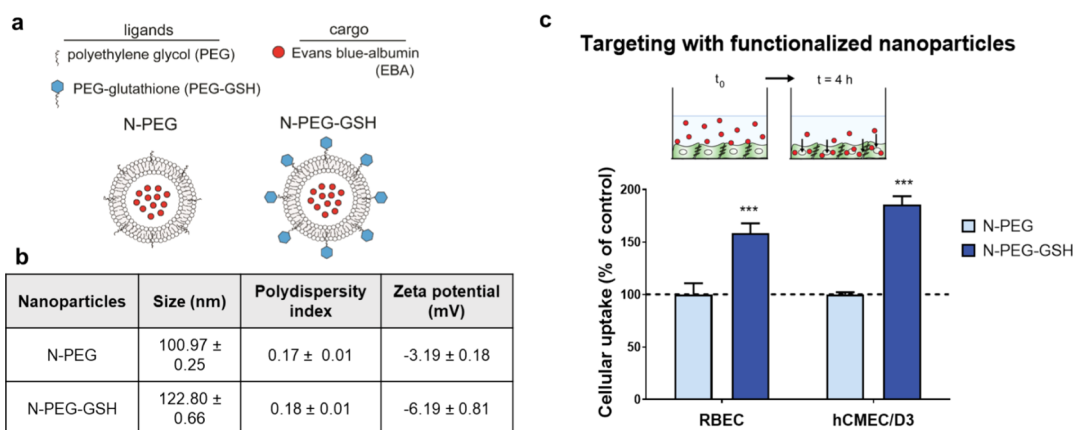
**Figure 2.** (a) Schematic drawing of PEGylated (N-PEG)- and PEGylated glutathione (N-PEG-GSH)-targeted vesicular nanoparticles loaded with Evans blue-albumin (EBA) cargo. (b) Main physicochemical properties of nanoparticles. (c) Uptake of EBA-loaded N-PEG and N-PEG-GSH nanoparticles in primary RBEC and hCMEC/D3. Values presented are means ± SD. Statistical analysis: ANOVA followed by Bonferroni posttest; ***$p < 0.001$; $n = 6$ for each group.
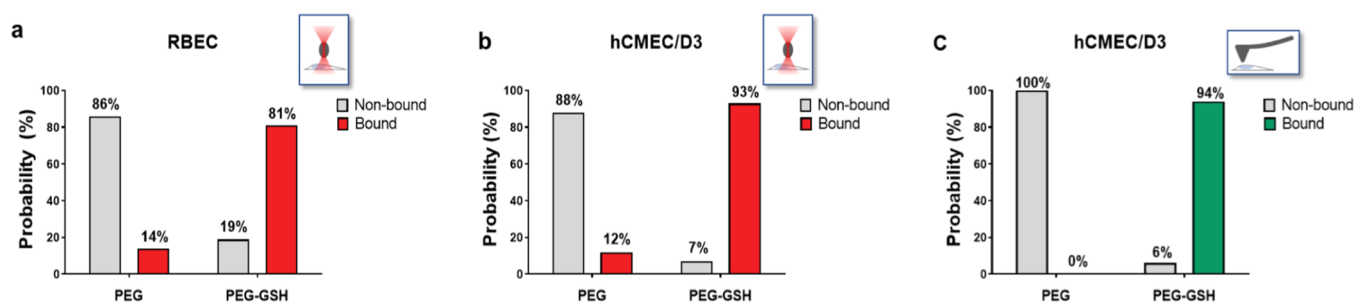


**Figure 3.** Binding probability of PEGylated (PEG) and glutathione-functionalized (PEG-GSH) SU-8 ellipsoids (a) to cultured primary RBEC and (b) to hCMEC/D3 ($N_{RBECPEG} = 118$, $N_{RBECPEG-GSH} = 159$, $N_{hCMEC/D3PEG} = 41$, and $N_{hCMEC/D3PEG-GSH} = 64$). (c) Binding probability of sharp functionalized atomic force microscope tip to hCMEC/D3 cells; $N_{PEG} = 42$ and $N_{PEG-GSH} = 124$.

Using well-characterized culture models of the BBB,[37] an increase in the uptake of the targeted N-PEG-GSH niosomes was seen in both primary rat brain endothelial cells (RBEC) and human cerebral microvascular endothelial cells (hCMEC/D3) (158 and 186%, respectively) compared to the non-targeted N-PEG group (Figure 2c).

These results confirm that PEG-GSH is an effective targeting ligand, which can significantly elevate cargo delivery in the brain endothelial cells, in agreement with our previous studies[11,12] and literature data.[38,39]

**Confirmation of the Presence of GSH on SU-8 Surfaces.** The surface coverage of GSH on differently functionalized SU-8 blocks was verified by fluorescence and confocal microscopy (Figure S1). We used the amine-reactive CY5 dye that can bind to the primary amine of GSH. Negative controls were the PEGylated and acid-treated SU-8 surfaces; positive controls were PEG-bisamine-treated SU-8 surfaces. For all samples, fluorescence intensities were determined from the middle, homogeneous section of each block image in the field of view. The pixel intensity values on the wide-field fluorescent images were first corrected with the background intensity measured on the glass surface next to the SU8 blocks and then averaged; the averaged intensities corresponding to the same kind of treatment were normalized with the positive control's values. On the confocal microscopy images, the background was negligible; so, the intensity values were just averaged and normalized. With both microscopy methods, the GSH-functionalized SU-8 blocks showed significantly higher

fluorescence than the acid-treated or PEGylated ones but noticeably smaller than the PEG-bisamine-treated ones. The positive control images indicate that the CY5 dye preferentially binds to surface amine groups.

The integrated fluorescent intensity of the image of a single CY5 molecule resulted in a 200 ± 40 pixel intensity unit ($n = 71$) (see Supporting Information, Figure S1j). The measured fluorescence intensity for each pixel (imaging an area of 100 nm × 100 nm in the sample) on the GSH-coated layer was 6700 ± 350 ($n = 7$) and on the PEGylated sample 1800 ± 220 ($n = 21$). Integrating these pixel intensity values over a square micrometer and dividing the result by the integrated intensity of a single CY5 gives a surface coverage value of 2500 ± 770 molecule/$\mu$m2. Assuming that every GSH binds one CY5 fluorophore, this results in about 2500 molecules of GSH over every square micrometer on the SU8 surface. The higher fluorescence of the GSH-functionalized surfaces as compared to the PEGylated ones demonstrates that GSH was immobilized on the SU-8 surface with the PEG-maleimide linker.

**Binding of GSH-Functionalized Surfaces to the Plasma Membrane of Living Brain Endothelial Cell Monolayers.** Before measuring the binding force between PEG-GSH-functionalized surfaces and cell membranes, we carried out experiments with simple polymerized ellipsoids on two types of brain endothelial cell monolayers, the rat primary RBEC and the human hCMEC/D3, to shed light on the binding probability between the two functionalizations, namely
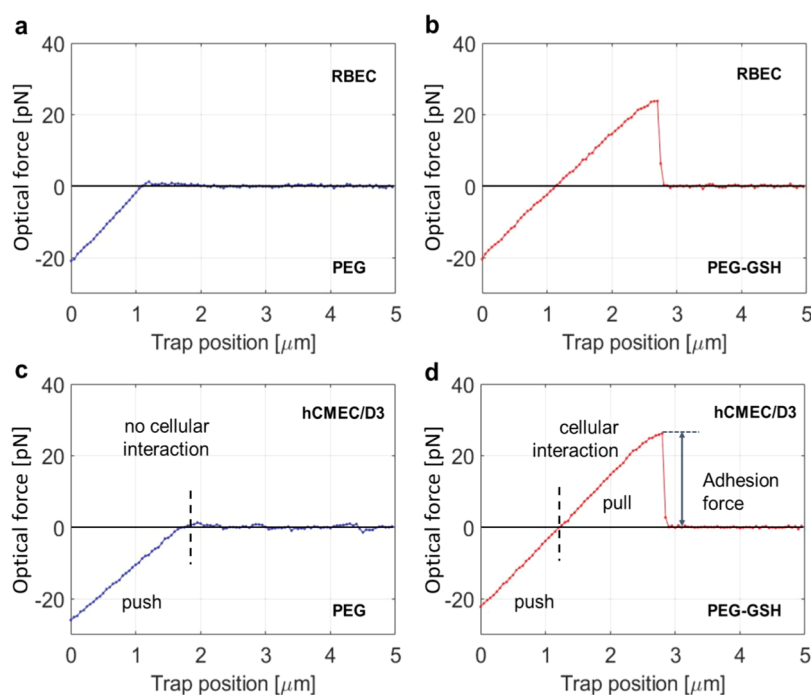
**Figure 4.** Representative optical force curves measured on brain endothelial cells with two kinds of surfaces. In the left column, force curves obtained with PEGylated (PEG) microtools on (a) RBEC and (c) hCMEC/D3 cell monolayers are shown. In the right column, two curves measured with glutathione-functionalized (PEG-GSH) microtools are shown for (b) RBEC and (d) hCMEC/D3 cells; all measurements were done with 50 nm step size. Vertical dashed lines mark the trap position where the retracted structure detaches from the cell without adhesion (c) and when the pushing force turns to pulling force in case of adherence (d). The graphs show a strong interaction between the microtool and the cells when GSH was present.

PEG-GSH versus PEG (Figure 3a,b). The expected outcome of this experiment was that PEG-GSH-coated SU-8 structures bind to these cells with a significantly higher probability than PEGylated ellipsoids. The probability was expressed as the percentage of the number of binding events relative to the total number of trials. We carried out these measurements with our HOT setup, using cells grown on a horizontal glass surface rather than on the vertical SU-8 walls, like in the adhesion force experiments. For both cell types, we performed at least two series of binding attempts on different cultures and different days.

A clear distinction was observed between the binding probabilities of the GSH-functionalized ellipsoids relative to the control, PEGylated structures; in the case of primary endothelial cells, when GSH was present, the ellipsoids bound to the cells with 81% probability as compared to 14% in the absence of the cell-targeting ligand. In the case of the hCMEC/D3 cell line, the GSH-promoted binding event reached a 93% probability compared to the 12% value in the control group without GSH. Similar results were obtained with the AFM measurements where PEGylated, sharp tip AFM cantilevers showed no binding to hCMEC/D3 cells, while the GSH-coated ones gave 94% binding probability ($N_{PEG}$ = 42, $N_{PEG-GSH}$ = 124). These results indicate that the surface of both human and rat brain endothelial cells preferentially binds GSH-coated surfaces. The increased docking may explain the higher cellular entry observed in our present experiments (Figure 2c) and uptake and transcytosis across the BBB models.[11,12,38]

**Adhesion Force Measurements.** After we demonstrated that the GSH-coating increased the binding probability of SU-8 structures and sharp tip AFM cantilevers to brain endothelial cells, we carried out adhesion measurements with our HOT setup to quantify the binding force. For these tests, optically actuated microtools with flat contact surfaces were used on cells that were grown on vertical SU-8 cell-supporting walls. At least two individual experiment series were run with each cell type on different days and cell cultures. The key step of these experiments is the retraction of the microtools by stepping the trapping focuses after they were pushed against the cell surface. These retractions were carried out with two different step sizes: 50 and 250 nm. The reason for this was to check if the retraction speed has any influence on the adhesion force. The time between the steps was kept constant due to technical reasons [fixed spatial light modulator (SLM) frame rate].

Representative adhesion curves are shown in Figure 4, where a significant difference could be observed between the traces recorded with GSH-coated microtools and those obtained with the PEGylated tools. It is clearly visible on the curves that at the very beginning of the retraction (trap position = 0 $\mu$m), the microtool is pushed against the cells with <30 pN optical force, which slowly and linearly decreases as the microtool is pulled back. At a certain trap position, the pushing force switches to pulling force if adhesion is present (Figure 4b,d), otherwise the microtool just detaches from the cell surface and no pulling force acts on the cell membrane (Figure 4a,c). In the case of adhesion, the cell membrane is pulled by the microtool up to a certain trap position, where their bond ruptures and they detach from each other returning the optical force to zero. The adhesion force is defined as the optical force at the rupture position. Interestingly, there is no apparent correlation between the magnitude of the adhesion force and that of the initial pushing force at zero trap position (see Figures S2 and S3).
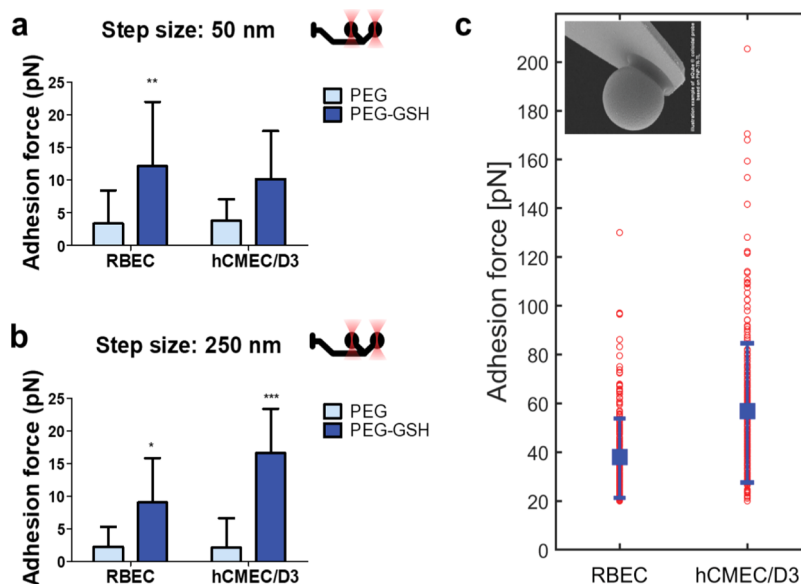
D

**Figure 5.** Adhesion force between the PEGylated (PEG) or glutathione-functionalized (PEG-GSH) surface of microtools and RBEC or hCMEC/D3 measured with (a) 50 and (b) 250 nm step size. Values presented are means ± SD. Statistical analysis: ANOVA followed by Bonferroni posttest; *$p < 0.05$; **$p < 0.01$; ***$p < 0.001$ compared to PEG groups in each column; for 50 nm step size: $N_{RBECPEG} = 16$, $N_{RBECPEG-GSH} = 14$, $N_{hCMEC/D3PEG} = 11$, and $N_{hCMEC/D3PEG-GSH} = 17$ and for 250 nm step size: $N_{RBECPEG} = 16$, $N_{RBECPEG-GSH} = 18$, $N_{hCMEC/D3PEG} = 24$, and $N_{hCMEC/D3PEG-GSH} = 10$. (c) Adhesion force between PEG-GSH-functionalized colloidal probes and the surface of RBEC or hCMEC/D3, as measured with AFM. Red circles represent individual measurements ($N = 247$ for both cell types), blue squares are their means, and blue lines are the SD.

Figure 5 summarizes the adhesion forces obtained with the peptide targeting-ligand-coated and with the PEGylated microtools on brain endothelial cells using two step sizes. The average adhesion force was always significantly higher when GSH was present than when it was omitted, and the ratio of the average measured adhesion forces between the two functionalization groups could be as high as 8. In the case of the GSH-coated structures, the difference between the 50 nm step size values and those recorded with 250 nm step size was not found to be statistically significant. When the smaller step size was used (Figure 5a), the average adhesion force for GSH-functionalized microtools was 12.1 ± 9.5 pN ($N = 14$) on RBEC cells and 10.2 ± 7.2 pN ($N = 17$) on hCMEC/D3 cells, whereas in the case of the PEGylated microtools, that is, our control group, it was 3.4 ± 4.9 pN ($N = 16$, RBEC) and 3.8 ± 3.2 pN ($N = 11$, hCMEC/D3). With 250 nm step size (Figure 5b), we measured 9 ± 6.6 pN adhesion force for RBEC cells ($N = 18$) and 16.4 ± 6 pN for hCMEC/D3 ($N = 10$) cells when the targeting ligand GSH was present, while for PEGylated microtools, the adhesion forces were only 2.2 ± 3 pN ($N = 16$, RBEC) and 2 ± 4.3 pN ($N = 24$, hCMEC/D3). The large standard deviation values are due to the inclusion of the zero adhesion force values in the overall calculation.

We also performed adhesion experiments with GSH-functionalized AFM cantilevers where instead of a sharp tip, a spherical probe with a 5 μm radius was attached to the end of the cantilever (Figure 5c). The contact area of this probe is comparable to that of our optically actuated microtool. The applied loading force was 100 pN, the dwell time toward the surface was 1 s, and the retraction speed was varied between 0.5 and 5 μm/s. The average of the adhesion forces measured with AFM is 3–6 times larger than those measured with the HOT (for RBEC: 38 ± 18 pN, for hCMEC/D3: 57 ± 28 pN, $N = 247$ for both cases). The possible reasons for this could be (i) that the larger force, almost an order of magnitude higher,

with which the sphere is pushed against the cell by the AFM cantilever (10–30 pN for HOT, 100 pN for AFM) is generating a larger number of bonds and (ii) that the detection level of the AFM is about 10 pN and only those measurements were taken into account, which resulted in an adhesion force larger than this value. In accordance with our observations, an interaction force of 20–60 pN was also measured by AFM between the carbon nanotubes targeted with folic acid and T24 cancer cells, depending on the loading rate.[27] The fact that the optical trapping-based method yields adhesion force values in the same range as the more standard AFM, reassures us that it is an effective tool to characterize ligand binding to cell membranes. Moreover, it has the additional benefit of higher sensitivity, being capable of measuring in the 1–10 pN range.

Although, GSH proved to be an effective targeting ligand of NP-aided drug uptake, little is known about the details of GSH-aided adhesion to the cell membrane. To our knowledge, our optical micromanipulation-based method is the first to measure the adhesion force between a GSH-coated surface and living brain endothelial cells. The optical trap has already helped in measuring the ligand−receptor binding force on cells, such as the Notch1 protein and Delta-like 1 (Dll1) protein binding[40] or claudin on epithelial-like human breast adenocarcinoma MCF-7 cells and its ligand, *Clostridium perfringens* enterotoxin (c-CPE).[41] Shergill and co-workers used Dll1-expressing cell lines and microbeads coated with the ligand-binding domain of the Notch1 protein to measure the adhesion force in an arrangement where the beads approached the cells with a lateral movement a few micrometers above the substrate. The measured typical rupture forces were in the range of 0–40 pN, and it was determined that a single bond is broken with 19 pN force on average. Reisenberg and co-workers measured the adhesion between MCF-7 cells expressing claudin-3, -4, and -7 and c-CPE-coated microbeads held 10 μm above the glass surface with optical tweezers and

made lateral attachment tests on the cells; the measured rupture forces fell between 5 and 30 pN. Our results for the adhesion forces of the GSH-coated surfaces toward brain endothelial cells are in the 10−15 pN range, which fits in the force range of the above ligand-binding experiments. Furthermore, the interaction was also shown to be specific because without GSH, the average nonspecific adhesion force was just 2−4 pN. This value of the adhesion force suggests a single bond rupture event. In our functionalization protocol of the SU-8 microtools, PEG-maleimide binds GSH covalently by the thiol group of its cysteine. From this, we can assume that the tripeptide's cysteine is not playing a role in the adhesion that precedes the uptake of the GSH-targeted niosomes.

The above ligand-binding OT experiments,[40,41] similarly to ours, used arrangements where the trapped probe beads move laterally, which permits to achieve larger forces and the bead position can be measured more precisely. In these experiments, however, the cells extend several micrometers above the substrate, which is necessary for being tested with the lateral motion of simple microbeads. Our approach, with cells grown on vertical walls and using extended microtools, involves two main improvements: first, flat cells can also be measured with the lateral movement of the microtool, and second, the intense trapping laser focus can be moved away from the cells even by tens of micrometers to prevent photodamage. Adhesion force measurements are the most meaningful when the cell membrane is approached from the direction of its normal, which, in the case of flat cells, is the normal of the supporting substrate too. Brain endothelial cells have a maximum of 1.5−2 $\mu$m thickness in the perinuclear region when cultured on a flat substrate,[42] which makes such an approach impossible with lateral movement on a horizontal substrate. The requirement to move the trapped microtool laterally and at the same time along the normal of the support naturally suggested the proposed arrangement with the endothelial cells cultured on a vertical wall (parallel to the optical axis) and the microtool moving horizontally toward this support. The presented adhesion force measurement method can easily be utilized for other types of cells with heights smaller than a few micrometers or even for model membranes. The only requirement is that the surface of the wall needs to be biocompatible, which supports cell culturing.

A promising way to further investigate GSH binding in the future is the removal of the cells' glycocalyx to expose membrane receptors or transporters in higher numbers, as well as to study the importance of surface charge in the docking process. We have successfully manipulated and measured the negative brain endothelial surface charge on cell layers cultured in a lab-on-a chip device,[43] which is known to affect BBB permeability. Indeed, we have demonstrated that making brain endothelial surface charge more positive by neuraminidase enzyme treatment or cationic lipid treatment increased the targeted nanoparticle uptake.[11] In these future experiments, the number of bonds is expected to increase, and the optical forces may not be strong enough to break them. If this happens, the lower surface coverage of the ligand molecule needs to be used or the interaction area of the probe part of the microtool needs to be reduced with a minor structural modification to limit the number of ligand−receptor bonds to only a few. Furthermore, our proof-of-concept measurement method can be extended in the future to increase the number of binding tests with the modification of the measurement protocol without significantly increasing measurement time. Finally, with the slight change of

the microtool coating protocol, namely using different functional PEG linkers, a wide range of ligands can be attached to it and characterized with the perspective of interaction with live cells.

## CONCLUSIONS

We reported for the first time GSH binding forces to brain endothelial cells using a novel HOT-based adhesion force measurement method. This method uses optically actuated microtools prepared specifically for this task with two-photon polymerization that are safer than trapped microbeads to use on the tested cells. This laser microfabrication method allows an easy way to change the geometry of the tool if the measurement methodology changes. We used our special cell-culturing method introduced earlier, where the tested cells were grown on photopolymerized walls that are parallel to the optical axis of the optical trapping system. This arrangement allowed us to measure adhesion forces on flat cells by approaching them with lateral movement of the trapped microtool. The measured force values fall into the 10−15 pN range and show definite specificity toward glutathione: without GSH, the adhesion forces are significantly, 3−8 times, smaller. These adhesion forces coincide with those found in the literature for other ligand−receptor pairs measured reliably with optical tweezers. The throughput of this novel measurement can be extended in the future that may help differentiate between single and multiple binding events and to select novel BBB targeting ligands based on the strength of the binding interaction.

## MATERIALS AND METHODS

**Materials and Reagents.** All reagents were purchased from Sigma-Aldrich Kft. Hungary (part of Merck Life Science), unless otherwise indicated.

**Preparation of Targeted Vesicular Nanoparticles.** For the synthesis of PEGylated glutathione (PEG-GSH), 13.5 mg of glutathione (0.044 mM) was reacted with 100 mg of N-[(3-maleimide-1-oxopropyl) aminopropyl polyethyleneglycol-carbamyl]-distearylphosphatidyl-ethanolamine (DSPE-PEG-MAL, 0.035 mM, SUNBRIGHT, NOF Europe, Belgium) in 0.1 M ammonium acetate for a day under nitrogen.[11] Vesicular nanoparticles, niosomes, were prepared from nonionic surfactants as described in our previous papers,[11,12] with minor modifications. Nonionic surfactants Span 60 (sorbitane monostearate) and Solulan C24 (cholesteryl-poly-24-oxyethylene-ether, Chemron Co., USA), as well as cholesterol, were dissolved in hot chloroform and ethanol (1:2) in a round-bottom flask. In the case of targeted nanovesicles (N-PEG-GSH, Figure 2a), PEG-GSH was added to the hot mixture at a concentration of 5% (w/w) of the total lipid. For the control, that is, PEGylated nanovesicles (N-PEG, Figure 2a), DSPE-PEG-MAL was added to the lipid mixture [5% (w/w) of total lipid] before the dissolving step. The removal of organic solvents from the samples by a vacuum pump yielded a thin lipid-film layer. The dry lipid film was hydrated with phosphate-buffered saline (PBS; KCl 2.7 mM, KH$_2$PO$_4$ 1.5 mM, NaCl 136 mM, Na$_2$HPO$_4$ × 2 H$_2$O 6.5 mM; pH 7.4) containing Evans blue-bovine serum albumin complex (EBA, 67 kDa; 0.167 mg/mL EB, 10 mg/mL BSA). The mixture was heated at 45 °C in a water bath and sonicated for 25 min. The suspension was forced through a polycarbonate filter (Whatman filter, 13 mm, 100 nm pore size) by the lipid extrusion technique (high-pressure thermobarrel extruder, Lipex Biomembranes Inc. USA) to yield vesicles. The non-entrapped cargo was removed by ultracentrifugation (123,249 g, 6 h, 4 °C); the pelleted nanoparticles were resuspended in phenol red-free DMEM/HAM's F-12 medium (Gibco, USA).

**Characterization of Targeted Vesicular Nanoparticles.** Particle size, polydispersity index (PDI), and zeta potential of
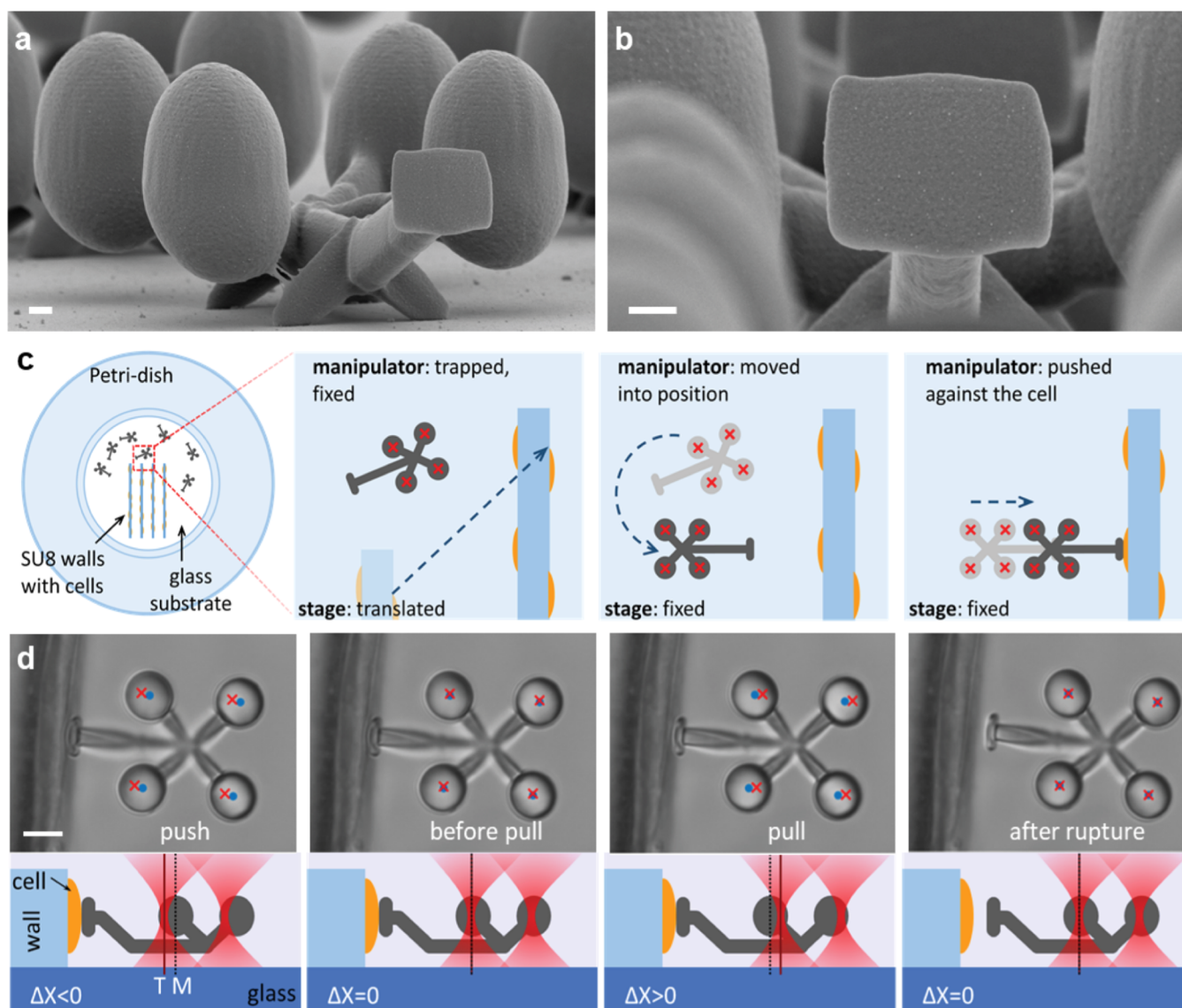
**Figure 6.** (a) Scanning electron microscopy (SEM) image of the microtool used for the experiments. Scale bar: 1 $\mu$m. (b) SEM image of the contact surface of the microtool. Scale bar: 1 $\mu$m. (c) Schematics of the sample used in the experiments and the sequence of microtool alignment for adhesion measurement; for details, see main text. (d) Image sequence from the record of a typical adhesion experiment (the retraction process). The red crosses show the trap positions, and the blue dots mark the centers of the microtool's spherical handles; scale bar: 5 $\mu$m. Below each image, a corresponding schematic side view drawing shows the relative positions of the trapping beam and the microtool. The dark red line shows trap position ($T$) and the black dotted line that of the manipulator sphere's center ($M$).

niosomes were measured by dynamic light scattering (Malvern Zetasizer Nano ZS, UK). Before measurements, samples were diluted in PBS to a final concentration of 2 mg/mL. Means were calculated from the average of at least 3 × 13 measurements per sample.

**Cell Culture.** *Primary Rat Brain Endothelial Cells.* Isolation and culture of primary RBEC were performed according to the method described in our previous studies.[44,45] After isolation, the brain microvessels were seeded onto culture dishes (Corning Costar, USA) coated with collagen type IV (100 $\mu$g/mL) and fibronectin (25 $\mu$g/mL) and were cultured in DMEM/HAM's F-12 (Gibco, USA) supplemented with 15% plasma-derived bovine serum (PDS, First Link, UK), 10 mM HEPES, 100 $\mu$g/mL heparin, 5 $\mu$g/mL insulin, 5 $\mu$g/mL transferrin, 5 ng/mL sodium selenite (ITS, Pan Biotech, Germany), 1 ng/mL basic fibroblast growth factor (bFGF, Roche, Switzerland), and 50 $\mu$g/mL gentamicin. During the first 3 days of culture, the medium of RBEC also contained 3 $\mu$g/mL puromicin to eliminate P-glycoprotein negative, contaminating cell types.[37] After the first 3 days of RBEC cultures, the amount of PDS was decreased from 15 to 10% in the culture medium.

*Human Cerebral Microvascular Brain Endothelial Cell Line.* The human brain endothelial cell line, hCMEC/D3, was purchased from Merck Millipore (cat. no. SCC066). Cultures of hCMEC/D3 (passage number ≤35) were grown in MCDB 131 medium (Pan-Biotech, Germany) supplemented with 5% fetal bovine serum (Sigma, Darmstadt, Germany), GlutaMAX (100×, Life Technologies, USA), lipid supplement (100×, Life Technologies, USA), 10 mM HEPES, 5 $\mu$g/mL insulin, 5 $\mu$g/mL transferrin, 5 ng/mL sodium selenite supplement (ITS; 100×, Pan-Biotech, Germany), 100 $\mu$g/mL heparin, 10 $\mu$g/mL ascorbic acid, 550 nM hydrocortisone, 1 ng/mL bFGF (Roche, Switzerland), and 50 $\mu$g/mL gentamicin. Before each experiment, the culture medium of the hCMEC/D3 cells was supplemented with 10 mM LiCl for 24 h to improve barrier properties.[37]

**Cellular Uptake of Functionalized Nanovesicles.** For quantification of cellular uptake, RBEC and hCMEC/D3 cells were seeded into 24-well plates (Corning Costar, USA) at the concentration of 3 × $10^4$ cells/well. Confluent monolayers were treated with 10 mg/mL N-PEG or N-PEG-GSH nanoparticles diluted

in the respective culture medium of each cell type at 37 °C for 4 h. After incubation, cells were washed 3 times with ice-cold PBS supplemented with 0.1% BSA, once with an acid-stripping buffer (glycine 50 mM, NaCl 100 mM, pH 3) to remove cell surface-associated nanovesicles, and once with PBS. Finally, the cells were lysed in distilled water containing 10 mg/mL Triton X-100 detergent, and the fluorescent signal of EBA cargo was quantified with a spectrofluorometer (Horiba Jobin Yvon Fluorolog 3, USA) at 584 nm excitation and 663 nm emission wavelengths.

**Preparation of Cell-Supporting Vertical Walls.** To grow cells on a vertical surface, we must use an appropriate supporting structure and coat it with adhesion promoters to increase the cell density and cell confluency. We used UV-mask-lithography to make approximately 100 $\mu$m tall, 100 $\mu$m wide, and 5 mm long walls out of the SU-8 photopolymer (MicroChem, USA) as supporting structures over the center of a circular 24 mm diameter cover slip (VWR, USA) according to the standard SU-8 process flow. An SU-8 layer was first spin-coated onto the cover slip, which was then illuminated through the mask with a UV photolithography flood exposure source ($\lambda$ = 365 nm, dose: 5000 mJ/cm$^2$, model 97435, Newport, USA) baked at 100 °C for 10 min and developed in PGMEA (Micro Resist Technology GmbH, Germany). The coverslip with the SU-8 wall on it was mounted onto a 35 × 10 mm cell-growing Petri dish (Greiner Bio GmbH, Germany) that had a 20 mm hole at its bottom, using Norland 68 (Norland Ltd, USA) optical glue. The Petri dish equipped with the cover slide and the SU-8 walls (Figure 6c) was coated with growth factor-reduced Matrigel (Corning Costar, USA). The RBEC and hCMEC/D3 endothelial cells were seeded on and around the wall region (1.5 × 10$^5$ cells/cm$^2$) and cultured for 2 days in the respective medium of each cell type.

**Preparation of the SU-8 Microstructures.** The following structures were fabricated using our two-photon-polymerization (TPP) system[46] out of SU-8 photopolymer: (i) simple blocks of 60 $\mu$m by 60 $\mu$m by 5 $\mu$m to fluorescently visualize GSH immobilization on SU-8 surface; (ii) ellipsoids (short axis: ~4 $\mu$m, long axis ~10 $\mu$m) to functionalize them with the targeting ligand, GSH, and with PEG-maleimide as the control to test our coating protocols with simple binding experiments on different cell types; and (iii) purpose-designed microtool with four spheres, a well-defined contact interface with an area of approximately 15 $\mu$m,[2] and their connecting rods for the adhesion force measurements (Figure 6). The structures were polymerized into an approximately 20 $\mu$m thick SU-8 layer covering a glass cover slide. The illumination light source was an ultrashort-pulsed laser (C-Fiber A, Menlo Systems GmbH, Martinsried, Germany). After illumination, the structures were baked and developed according to the standard SU-8 process flow. The blocks were polymerized with 9 mW laser power, the ellipsoids with 6 mW, and the microtools with 3 mW; the applied scan speed varied between 1 and 100 $\mu$m/s for various parts of the structures. After development, the ellipsoids and the microtools were functionalized as described below, removed from the substrate with gentle mechanical agitation, collected from the surface with a pipette, and finally injected into the sample space to the proximity of the cultured cells.

The ellipsoids and the microtools were actuated with HOT in the sample. The ellipsoid requires one trapping focus to move, while the microtool needs four of them, where each focus traps one of its spheres. The microtool, when trapped, can be moved anywhere in the sample space, and its contact interface can also be pointed toward the required direction, preferentially the target cell. SU-8 was ideal for optical manipulation because it has a relatively high refractive index (1.59), ensuring strong trapping; it is biocompatible but it can be functionalized with oxidative processes to coat its surface with covalently bonded ligands of interest.

**Functionalization of the SU-8 Microstructures.** The covalent modifications of the SU-8 surfaces were carried out by the following steps. In the first acid treatment step, the substrate with the microstructures was immersed into the aqueous solution of 0.1 M ammonium-cerium(IV)-nitrate and 1 M HNO$_3$ (AnalytiCals Ltd.) for 30 min at room temperature (RT), and then it was rinsed with MilliQ water and dried. In the following PEGylation step, 100 $\mu$L of amino-PEG-maleimide (Nanosoft polymers Ltd, USA) dissolved in ethanol (0.1 mg/mL) was dropped onto the structures for a 45 min incubation at RT. To coat the surface with GSH, we immersed the PEGylated sample into a slightly alkaline (pH = 7.5) PBS solution of 100 mM GSH for 60 min at RT (GSH-functionalization step); the tripeptide GSH binds to the maleimide on the PEG-maleimide linker through its cysteine in the middle. We also coated some of the acid-treated, 60 $\mu$m by 60 $\mu$m by 5 $\mu$m SU-8 blocks with PEG-bisamine instead of PEG-maleimide; the treatment was carried out with the same concentrations and incubation conditions as in the case of PEG-maleimide. After GSH incubation, the samples were thoroughly washed with PBS and kept in it until the start of the experiment, which usually took place within less than 1 hour.

To visualize the presence of GSH on the functionalized SU-8 surface, we used an amine-reactive CY5 dye (Abcam Ltd, USA # ab146454) that can bind to GSH through its primary amine group. The sample with the 60 $\mu$m × 60 $\mu$m × 5 $\mu$m SU-8 blocks was incubated with 150 $\mu$L of 0.01 mg/mL CY5 dye dissolved in a 1:1 mixture of H$_2$O/DMSO for 30 min at 4 °C in the dark. Then, we washed them in a 1:1 H$_2$O/DMSO mixture for 5 min, in a 20:1 H$_2$O/DMSO mixture for the same time, and then in Milli-Q water, and the blocks were finally dried. The fluorescence of the surface of the blocks was observed with wide-field and confocal fluorescence microscopy. The positive control for GSH staining was the PEG-bisamine-treated surface since it has only amine groups on its surface, while the acid-treated and the PEGylated samples were used as negative controls to visualize the nonspecific staining of the CY5 dye.

The GSH surface coverage measurement was based on the comparison of the integrated intensity of single CY5 molecules and that of the uniformly fluorescent CY5 layer bound to the GSH on the SU8 blocks. First, 1.5 $\mu$L of 1 ng/mL amine-reactive CY5 solution in ultrapure water was dropped onto an ethanol-cleaned cover slide, and the droplet was covered with another cover slide creating an about 5 $\mu$m thin liquid layer. From this very dilute solution, the molecules adhered to the surface such that they were separated enough to be imaged individually. The single CY5 molecules adhered to the clean glass surface (see the Supporting Information, Figure S1i), and the uniform CY5 layer bound to the functionalized SU8 surfaces (see the Supporting Information, Figure S1a–d) were imaged with our wide-field fluorescent microscopy setup, using the same illumination and observation conditions: the light source was a metal halide lamp (Lumen 200S, Prior Scientific, Inc., USA), and the images were recorded with a CMOS camera (ORCA-Flash4.0 V3, type num.: C13440-20CU, Hamamatsu Corp., Japan). The number of fluorescent molecules over a unit area was calculated by dividing the integrated intensity of the uniformly fluorescent layer over the unit area with the integrated intensity of a single CY5 molecule. The fluorescence measured over the PEGylated samples was used as the background; the emission by CY5 on the GSH-coated samples was corrected with this background value. Assuming that every glutathione molecule binds a fluorophore, the corrected amount of CY5 directly results in the surface coverage of the GSH.

**Holographic Optical Micromanipulation Setup.** Our HOT system (see Figure S4) is built around a Nikon Eclipse TI fluorescence microscope body. The trapping beams originated from a continuous wave fiber laser ($\lambda$ = 1070 nm, BKtel Photonics) and a UPlanSApo 60X, NA = 1.2, a water immersion objective (Olympus) was used to focus the trapping beams. For multiple focal spot generation and their translation in 3D, a spatial light modulator (SLM) (Pluto NIR, Holoeye) was included in the optical system. This device splits the original laser beam into several beams and individually manipulates the trapping foci with 6 degrees of freedom in real-time.[46] The microtools, prepared for the adhesion measurements, were designed with four spheres on them; therefore, four trapping foci at the corners of a square were generated with the SLM and used to trap and maneuver the tool in the sample space. The trapping beam power was 270 mW for the four beams measured at the back aperture of the objective. The orientation toward the cells and the precise movement of the microtool was observed and recorded with an EMCCD camera (Rolera EMC2, Qimaging, Surrey,

BC, Canada). The trapping experiments were carried out inside a temperature-controlled sample holder, which was able to keep the temperature at 37 °C for the whole duration of the experiments. The serum content of the cell culture medium was decreased to 1% 2 h before the start of the adhesion force measurements.

**Ellipsoid Binding Experiments.** The ellipsoid binding experiments were carried out in Matrigel-coated Petri dishes with a glass bottom (diameter: 3.5 cm; Greiner Bio-One, Germany). The RBEC and hCMEC/D3 cells were seeded at the concentration of $1.5 \times 10^5$ cells/cm$^2$ and were cultured for 2 days in the respective medium of cell types. A cell-ellipsoid binding attempt was carried out as follows: an individual ellipsoid was first picked up by the optical tweezers and lifted to about 5 $\mu$m above the glass substrate. Then, the ellipsoid was brought above a target cell by not moving the optical trap but translating the microscope stage to locate the cell. Finally, the ellipsoid was pushed toward the cell's surface from above; with cells grown on a horizontal plane, the ellipsoids were pushed toward the cells by translating the trap position downward along the optical axis. After holding the ellipsoid in this position for 10 s, the trap position was slowly moved upward to remove the ellipsoid from the cell, during which the ellipsoid either could be detached from the cell (no-binding event) or could not (binding event). Then, the numbers of no-binding and binding events for the GSH-coated and PEGylated structures were compared for the two cell types (Figure 3).

**Stiffness Calibration of the Microtool.** In order to measure the binding forces $F_B$ with the optical trap, we had to determine the stiffness of the trapped microtools ($k_{str}$) along their symmetry axis, that is, the direction in which they exert force on the cells. During the adhesion measurements, the displacement $\Delta X_{str}$ of the microtool from the equilibrium trap positions is measured and from that $F_B$ can be calculated: $F_B = k_{str} \times \Delta X_{str}$. We determined the trap stiffness for the microtool indirectly with 6 $\mu$m latex beads of known trap stiffness ($k_{bead}$). By pushing the microtool against the trapped bead, the displacements of the bead and the microtool ($\Delta X_{bead}$ and $\Delta X_{str}$, respectively) could be measured and $k_{str}$ was calculated from the following equation: $k_{bead} \times \Delta X_{bead} = k_{str} \times \Delta X_{str}$. The measured $k_{bead}$ stiffness of the 6 $\mu$m bead was 4.9 pN/$\mu$m on average, which was determined from its fluctuation within a single steady trap.[30] This value resulted in an average stiffness of $k_{str} = 25.8$ pN/$\mu$m for the microtools.

**Adhesion Force Measurements with the Microtool.** The procedure of the experiment is illustrated in Figure 6. The mutual position of the cells and the microtools (Figure 6a,b) was changed either by moving the microtool with the optical tweezers or by moving the sample with the motorized microscope stage (Figure 6c). First, the microtools were placed in the Petri dish, which already contained the cells in growth media, and then the target cell was localized. Next, a structure was picked up with the optical trap, carried to the chosen cell by moving the sample stage, and then turned in position by moving the optical traps: its contact surface and the cell membrane were parallelized, and both were brought into focus. Next, the microtool approached the cell by slowly moving it with the optical tweezers until the contact surface touched the cell; this event was determined visually by monitoring the faintly visible trapping focal spots. Then, the microtool was pushed against the cell with about 10–20 pN force by advancing the four trapping beams.

This was the point where the adhesion force measurement procedure, illustrated in Figure 6d, actually began. When the microtool was pushed to the chosen cell's surface, the displacement of the trapped sphere from its equilibrium position ($\Delta X$) was considered negative. After waiting for 10 s in this position, we pulled the structure back by 5 $\mu$m with 50 nm or 250 nm steps with the optical tweezers. During this retraction, a bright-field image was taken of the microtool after each step, resulting in 100 and 20 images for the 50 and 250 nm step size, respectively. At the beginning of the retraction, the microtool did not move but the still negative $\Delta X$ slowly increased. If there was no adhesion between the microtool and the cell, $\Delta X$ first became zero, and then the microtool separated from the cell and followed the trapping foci ($\Delta X$ did not increase any more). If there was any adhesion, $\Delta X$ became positive and a considerable

pulling force was exerted on the microtool by the optical trap. Eventually, when the optical force exceeded the adhesion force, the microtool separated from the cell and the centers of the spheres returned to the trap positions ($\Delta X$ becomes zero). Next, either the same microtool was used to test another cell (maximum of 3 cells per microtool) or another microtool was trapped and used on the next cell. All experiments were repeated at least 2 times on different days and the number of parallel measurements in each experiment was 6–10.

**Atomic Force Microscopy Measurements.** Brain endothelial cells were seeded on a Matrigel-coated circular 24 mm diameter coverslip for AFM measurements. The RBEC and hCMEC/D3 cells ($1.5 \times 10^5$ cells/cm$^2$) were cultured for 2 days in their respective culture media. The serum content of the culture media was decreased to 1% 2 h before the start of the experiments. The coverslips with the cells were mounted inside the lid of a Petri dish for support. A droplet of the medium was placed over the cell layer, and the AFM cantilever was immersed in it. All AFM measurements were carried out with an Asylum Research MFP-3D head and controller in the contact mode (Oxford Instruments Asylum Research). The driver program of MFP-3D (version 16.12.214) was written in IGOR Pro Software (version 6.38B01, Wavemetrics). The typical dwell time before retraction was 1 s, the loading force was 100 pN, and the retraction speed was 0.5–5 $\mu$m/s. The actual spring constants for each cantilever in liquid were determined by the thermal fluctuation technique[47−49] after the measurements. Data analysis was done using the IGOR Pro Software.

*Cell-Binding Measurements with Sharp-Tipped Cantilevers.* As a preliminary experiment, we did adhesion probability measurements with sharp silica-tipped AFM cantilevers with a nominal spring constant of 30 pN/nm (Bruker, MSCT-D). The AFM probes were incubated in 2% (v/v) APTES ((3-aminopropyl)triethoxysilan) dissolved in isopropanol (Molar Chemicals Ltd.) for 1.5 h at room temperature to create free primary amine groups on their surface.[50−52] This was followed by glutaraldehyde incubation (1% in Milli-Q water, 5 min),[53,54] which enables the binding of the PEG linker's amine group to the amine group of APTES. Afterward, the amino-PEG-maleimide linker was attached to the AFM tip's surface via incubating the cantilevers in 10 mg/mL ethanol solution for 20 min; the AFM tip, prepared up to this point, was used as a negative control and is referred to as the PEGylated tip. As the last step, the cantilevers were immersed in freshly made 100 mM GSH solution in PBS for 20 min to obtain GSH-covered AFM tips.

*Adhesion Force Measurements with Colloidal Probes.* For force measurements, borosilicate colloidal probes with 10 $\mu$m diameter were used on triangular cantilevers with a nominal spring constant of 10 pN/nm (NovaScan). The functionalization of these spherical tipped cantilevers was done by the same protocol as mentioned in the previous section.

**Statistical Analysis.** The adhesion force data were calculated from the images recorded during the optical tweezers experiments with the following steps. First, on all images recorded during a single adhesion experiment, a circle was fitted to all four spheres of the microtool's image, yielding the center for each sphere. The average position of the four centers was then calculated, and its component in the direction of the movement of the trap was plotted as the function of the trapping focus position. After the detachment of the structures from the cell in each individual experiment, the averaged center position coincided with the trapping beam position and grew linearly with it (gray dots in Figure S2e, Supporting Information). Next, a straight line was fitted to this linearly increasing section, extrapolated until the zero-trap position, and the averaged sphere positions were subtracted from it, yielding the $\Delta X$ values (red dots in Figure S2e, Supporting Information). The optical force was then calculated simply by multiplying the $\Delta X$ values with the trap stiffness of the microtool (25.8 pN/$\mu$m). The adhesion force is the amplitude of the sudden drop in the optical forces graph (Figure 4d). Statistical analyses were performed using GraphPad Prism 8 software (Graph-Pad Software, USA). Values were compared using ANOVA followed by Bonferroni posttest. Differences were considered to be statistically significant at $p < 0.05$.

## ■ AUTHOR INFORMATION

### Corresponding Authors

**Tamás Fekete** − *Institute of Biophysics, Biological Research Centre, Eötvös Loránd Research Network (ELKH), Szeged 6726, Hungary; Doctoral School in Multidisciplinary Medicine, University of Szeged, Szeged 6720, Hungary;* ⓞ orcid.org/0000-0002-1557-845X; Email: Fekete.Tamas.5@stud.u-szeged.hu

**Szilvia Veszelka** − *Institute of Biophysics, Biological Research Centre, Eötvös Loránd Research Network (ELKH), Szeged 6726, Hungary;* Email: szilvia.veszelka@brc.hu

**Lóránd Kelemen** − *Institute of Biophysics, Biological Research Centre, Eötvös Loránd Research Network (ELKH), Szeged 6726, Hungary;* ⓞ orcid.org/0000-0001-7772-2165; Email: kelemen.lorand@brc.hu

### Authors

**Mária Mészáros** − *Institute of Biophysics, Biological Research Centre, Eötvös Loránd Research Network (ELKH), Szeged 6726, Hungary*

**Zsolt Szegletes** − *Institute of Biophysics, Biological Research Centre, Eötvös Loránd Research Network (ELKH), Szeged 6726, Hungary*

**Gaszton Vizsnyiczai** − *Institute of Biophysics, Biological Research Centre, Eötvös Loránd Research Network (ELKH), Szeged 6726, Hungary;* ⓞ orcid.org/0000-0003-3245-3736

**László Zimányi** − *Institute of Biophysics, Biological Research Centre, Eötvös Loránd Research Network (ELKH), Szeged 6726, Hungary;* ⓞ orcid.org/0000-0002-5101-2023

**Mária A. Deli** − *Institute of Biophysics, Biological Research Centre, Eötvös Loránd Research Network (ELKH), Szeged 6726, Hungary;* ⓞ orcid.org/0000-0001-6084-6524

Complete contact information is available at:
https://pubs.acs.org/10.1021/acsami.1c08454

### Author Contributions

§T.F. and M.M. contributed equally to this manuscript. T.F. prepared and functionalized the polymer microtools and performed the adhesion force measurements with them. M.M. and S.V. prepared the nanoparticles and performed all cell culture experiments. T.F., M.M., S.V., M.D., and L.K designed the experiments. Z.S. carried out the AFM measurements. L.K., T.F., M.M., and S.V. analyzed the data. L.K., T.F., M.M., S.V., L.Z., and M.D. wrote the paper. L.K., L.Z., S.V., and M.D supervised the work.

### Notes

The authors declare no competing financial interest.

## ■ REFERENCES

(1) Angioletti-Uberti, S. Theory, Simulations and the Design of Functionalized Nanoparticles for Biomedical Applications: A Soft Matter Perspective. *npj Comput. Mater.* **2017**, *3*, 48.

(2) Masserini, M. Nanoparticles for Brain Drug Delivery. *ISRN. Biochem.* **2013**, *2013*, 238428.

(3) Banks, W. A. From Blood-Brain Barrier to Blood-brain Interface: New Opportunities for CNS Drug Delivery. *Nat. Rev. Drug Discovery* **2016**, *15*, 275−292.

(4) Kreuter, J. Mechanism of Polymeric Nanoparticle-Based Drug Transport Across the Blood-brain Barrier (BBB). *J. Microencapsulation* **2013**, *30*, 49−54.

(5) Ulbrich, K.; Hekmatara, T.; Herbert, E.; Kreuter, J. Transferrin- and transferrin-receptor-antibody-modified nanoparticles enable drug delivery across the blood-brain barrier (BBB). *Eur. J. Pharm. Biopharm.* **2009**, *71*, 251−256.

(6) Ulbrich, K.; Knobloch, T.; Kreuter, J. Targeting the Insulin Receptor: Nanoparticles for Drug Delivery Across the Blood-Brain Barrier (BBB). *J. Drug Targeting* **2011**, *19*, 125−132.

(7) Loureiro, J. A.; Gomes, B.; Fricker, G.; Cardoso, I.; Ribeiro, C. A.; Gaiteiro, C.; Coelho, M. A. N.; Pereira, M. d. C.; Rocha, S. Dual Ligand Immunoliposomes for Drug Delivery to the Brain. *Colloids Surf., B* **2015**, *134*, 213−219.

(8) Johnsen, K. B.; Moos, T. Revisiting Nanoparticle Technology for Blood-Brain Barrier Transport: Unfolding at the Endothelial Gate Improves the Fate of Transferrin Receptor-Targeted Liposomes. *J. Controlled Release* **2016**, *222*, 32−46.

(9) Topal, G. R.; Mészáros, M.; Porkoláb, G.; Szecskó, A.; Polgár, T. F.; Siklós, L.; Deli, M. A.; Veszelka, S.; Bozkir, A. ApoE-Targeting Increases the Transfer of Solid Lipid Nanoparticles with Donepezil Cargo across a Culture Model of the Blood-Brain Barrier. *Pharmaceutics* **2021**, *13*, 38.

(10) Gromnicova, R.; Davies, H. A.; Sreekanthreddy, P.; Romero, I. A.; Lund, T.; Roitt, I. M.; Phillips, J. B.; Male, D. K. Glucose-Coated Gold Nanoparticles Transfer Across Human Brain Endothelium and Enter Astrocytes In Vitro. *PLoS One* **2013**, *8*, No. e81043.

(11) Mészáros, M.; Porkoláb, G.; Kiss, L.; Pilbat, A.-M.; Kóta, Z.; Kupihár, Z.; Kéri, A.; Galbács, G.; Siklós, L.; Tóth, A.; Fülöp, L.; Csete, M.; Sipos, Á.; Hülper, P.; Sipos, P.; Páli, T.; Rákhely, G.; Szabó-Révész, P.; Deli, M. A.; Veszelka, S. Niosomes Decorated With Dual Ligands Targeting Brain Endothelial Transporters Increase Cargo Penetration Across the Blood-Brain Barrier. *Eur. J. Pharm. Sci.* **2018**, *123*, 228−240.

(12) Porkoláb, G.; Mészáros, M.; Tóth, A.; Szecskó, A.; Harazin, A.; Szegletes, Z.; Ferenc, G.; Blastyák, A.; Mátés, L.; Rákhely, G.; Deli, M. A.; Veszelka, S. Combination of Alanine and Glutathione as Targeting Ligands of Nanoparticles Enhances Cargo Delivery into the Cells of the Neurovascular Unit. *Pharmaceutics* **2020**, *12*, 635.

(13) Woods, S.; O'Brien, L. M.; Butcher, W.; Preston, J. E.; Georgian, A. R.; Williamson, E. D.; Salguero, F. J.; Modino, F.; Abbott, N. J.; Roberts, C. W.; D'Elia, R. V. Glucosamine-NISV Delivers Antibody Across the Blood-Brain Barrier: Optimization for Treatment of Encephalitic Viruses. *J. Controlled Release* **2020**, *324*, 644−656.

(14) Gaillard, P. J. BBB Crossing Assessment and BBB Crossing Technologies in CNS Drug Discovery. *Drug Discovery Today: Technol.* **2016**, *20*, 1−3.

(15) Birngruber, T.; Raml, R.; Gladdines, W.; Gatschelhofer, C.; Gander, E.; Ghosh, A.; Kroath, T.; Gaillard, P. J.; Pieber, T. R.; Sinner, F. Enhanced Doxorubicin Delivery to the Brain Administered Through Glutathione PEGylated Liposomal Doxorubicin (2B3-101) as Compared with Generic Caelyx,/Doxil-A Cerebral Open Flow Microperfusion Pilot Study. *J. Pharm. Sci.* **2014**, *103*, 1945−1948.

(16) Gaillard, P. J.; Appeldoorn, C. C. M.; Dorland, R.; van Kregten, J.; Manca, F.; Vugts, D. J.; Windhorst, B.; van Dongen, G. A. M. S.; de Vries, H. E.; Maussang, D.; van Tellingen, O. Pharmacokinetics, Brain Delivery, and Efficacy in Brain Tumor-Bearing Mice of Glutathione Pegylated Liposomal Doxorubicin (2B3-101). *PloS One* **2014**, *9*, No. e82331.

(17) Kanhai, K. M. S.; Zuiker, R. G. J. A.; Stavrakaki, I.; Gladdines, W.; Gaillard, P. J.; Klaassen, E. S.; Groeneveld, G. J. Glutathione-PEGylated Liposomal Methylprednisolone in Comparison to Free Methylprednisolone: Slow Release Characteristics and Prolonged Lymphocyte Depression in a First-in-Human Study. *Br. J. Clin. Pharmacol.* **2018**, *84*, 1020−1028.

(18) Donahue, N. D.; Acar, H.; Wilhelm, S. Concepts of Nanoparticle Cellular Uptake, Intracellular Trafficking, and Kinetics in Nanomedicine. *Adv. Drug Delivery Rev.* **2019**, *143*, 68−96.

(19) Zhang, S.; Gao, H.; Bao, G. Physical Principles of Nanoparticle Cellular Endocytosis. *ACS Nano* **2015**, *9*, 8655−8671.

(20) Manzanares, D.; Ceña, V. Endocytosis: The Nanoparticle and Submicron Nanocompounds Gateway into the Cell. *Pharmaceutics* **2020**, *12*, 371.

(21) Vilella, A.; Ruozi, B.; Belletti, D.; Pederzoli, F.; Galliani, M.; Semeghini, V.; Forni, F.; Zoli, M.; Vandelli, M.; Tosi, G. Endocytosis of Nanomedicines: The Case of Glycopeptide Engineered PLGA Nanoparticles. *Pharmaceutics* **2015**, *7*, 74−89.

(22) Toth, A. E.; Holst, M. R.; Nielsen, M. S. Vesicular Transport Machinery in Brain Endothelial Cells: What We Know and What We Do not. *Curr. Pharm. Des.* **2020**, *26*, 1405−1416.

(23) Yuan, H.; Li, J.; Bao, G.; Zhang, S. Variable Nanoparticle-Cell Adhesion Strength Regulates Cellular Uptake. *Phys. Rev. Lett.* **2010**, *105*, 138101.

(24) Tietjen, G. T.; Bracaglia, L. G.; Saltzman, W. M.; Pober, J. S. Focus on Fundamentals: Achieving Effective Nanoparticle Targeting. *Trends Mol. Med.* **2018**, *24*, 598−606.

(25) Lamprecht, C.; Hinterdorfer, P.; Ebner, A. Applications of Biosensing Atomic Force Microscopy in Monitoring Drug and Nanoparticle Delivery. *Expert Opin. Drug Delivery* **2014**, *11*, 1237−1253.

(26) Oliveira, H.; Rangl, M.; Ebner, A.; Mayer, B.; Hinterdorfer, P.; Pêgo, A. P. Molecular Recognition Force Spectroscopy: a New Tool to Tailor Targeted Nanoparticles. *Small* **2011**, *7*, 1236−1241.

(27) Lamprecht, C.; Plochberger, B.; Ruprecht, V.; Wieser, S.; Rankl, C.; Heister, E.; Unterauer, B.; Brameshuber, M.; Danzberger, J.; Lukanov, P.; Flahaut, E.; Schütz, G.; Hinterdorfer, P.; Ebner, A. A Single-Molecule Approach to Explore Binding, Uptake and Transport of Cancer Cell Targeting Nanotubes. *Nanotechnology* **2014**, *25*, 125704.

(28) Gomes, C. P.; Lopes, C. D. F.; Leitner, M.; Ebner, A.; Hinterdorfer, P.; Pêgo, A. P. Atomic Force Microscopy as a Tool to Assess the Specificity of Targeted Nanoparticles in Biological Models of High Complexity. *Adv. Healthcare Mater.* **2017**, *6*, 1700597.

(29) Neuman, K. C.; Nagy, A. Single-Molecule Force Spectroscopy: Optical Tweezers, Magnetic Tweezers and Atomic Force Microscopy. *Nat. Methods* **2008**, *5*, 491−505.

(30) Neuman, K. C.; Block, S. M. Optical Trapping. *Rev. Sci. Instrum.* **2004**, *75*, 2787−2809.

(31) Nawaz, S.; Sánchez, P.; Bodensiek, K.; Li, S.; Simons, M.; Schaap, I. A. Cell Visco-Elasticity Measured with AFM and Optical Trapping at Sub-Micrometer Deformations. *Plos One* **2012**, *7*, No. e45297.

(32) Vargas-Pinto, R.; Gong, H.; Vahabikashi, A.; Johnson, M. The Effect of the Endothelial Cell Cortex on Atomic Force Microscopy Measurements. *Biophys. J.* **2013**, *105*, 300−309.

(33) Falleroni, F.; Torre, V.; Cojoc, D. Cell Mechanotransduction with Piconewton Forces Applied by Optical Tweezers. *Front. Cell. Neurosci.* **2018**, *12*, 130.

(34) Grexa, I.; Fekete, T.; Molnár, J.; Molnár, K.; Vizsnyiczai, G.; Ormos, P.; Kelemen, L. Single-Cell Elasticity Measurement with an Optically Actuated Microrobot. *Micromachines* **2020**, *11*, 882.

(35) Abdelkader, H.; Alani, A. W. G.; Alany, R. G. Recent Advances in Non-Ionic Surfactant Vesicles (Niosomes): Self-Assembly, Fabrication, Characterization, Drug Delivery Applications and Limitations. *Drug Delivery* **2014**, *21*, 87−100.

(36) Saraiva, C.; Praça, C.; Ferreira, R.; Santos, T.; Ferreira, L.; Bernardino, L. Nanoparticle-Mediated Brain Drug Delivery: Overcoming Blood-Brain Barrier to Treat Neurodegenerative Diseases. *J. Controlled Release.* **2016**, *235*, 34−47.

(37) Veszelka, S.; Tóth, A.; Walter, F. R.; Tóth, A. E.; Gróf, I.; Mészáros, M.; Bocsik, A.; Hellinger, É.; Vastag, M.; Rákhely, G.; Deli, M. A. Comparison of a Rat Primary Cell-Based Blood-Brain Barrier Model With Epithelial and Brain Endothelial Cell Lines: Gene Expression and Drug Transport. *Front. Mol. Neurosci.* **2018**, *11*, 166.

(38) Geldenhuys, W.; Wehrung, D.; Groshev, A.; Hirani, A.; Sutariya, V. Brain-Targeted Delivery of Doxorubicin Using Glutathione-Coated Nanoparticles for Brain Cancers. *Pharm. Dev. Technol.* **2015**, *20*, 497−506.

(39) Maussang, D.; Rip, J.; van Kregten, J.; van den Heuvel, A.; van der Pol, S.; van der Boom, B.; Reijerkerk, A.; Chen, L.; de Boer, M.; Gaillard, P.; de Vries, H. Glutathione Conjugation Dose-Dependently Increases Brain-Specific Liposomal Drug Delivery in Vitro and in Vivo. *Drug Discovery Today: Technol.* **2016**, *20*, 59−69.

(40) Shergill, B.; Meloty-Kapella, L.; Musse, A. A.; Weinmaster, G.; Botvinick, E. Optical Tweezers Studies on Notch: Single-Molecule Interaction Strength is Independent of Ligand Endocytosis. *Dev. Cell* **2012**, *22*, 1313−1320.

(41) Riesenberg, C.; Iriarte-Valdez, C. A.; Becker, A.; Dienerowitz, M.; Heisterkamp, A.; Ngezahayo, A.; Torres-Mapa, M. L. Probing Ligand-Receptor Interaction in Living Cells Using Force Measurements with Optical Tweezers. *Front. Bioeng. Biotechnol.* **2020**, *8*, 598459.

(42) Hellinger, É.; Veszelka, S.; Tóth, A. E.; Walter, F.; Kittel, Á.; Bakk, M. L.; Tihanyi, K.; Háda, V.; Nakagawa, S.; Dinh Ha Duy, T.; Niwa, M.; Deli, M. A.; Vastag, M. Comparison of Brain Capillary Endothelial Cell-Based and Epithelial (MDCK-MDR1, Caco-2, and VB-Caco-2) Cell-Based Surrogate Blood-Brain Barrier Penetration Models. *Eur. J. Pharm. Biopharm.* **2012**, *82*, 340−351.

(43) Kincses, A.; Santa-Maria, A. R.; Walter, F. R.; Dér, L.; Horányi, N.; Lipka, D. V.; Valkai, S.; Deli, M. A.; Dér, A. A Chip Device to Determine Surface Charge Properties of Confluent Cell Monolayers by Measuring Streaming Potential. *Lab Chip* **2020**, *20*, 3792−3805.

(44) Nakagawa, S.; Deli, M. A.; Kawaguchi, H.; Shimizudani, T.; Shimono, T.; Kittel, Á.; Tanaka, K.; Niwa, M. A New Blood-Brain Barrier Model Using Primary Rat Brain Endothelial Cells, Pericytes and Astrocytes. *Neurochem. Int.* **2009**, *54*, 253−263.

(45) Barna, L.; Walter, F. R.; Harazin, A.; Bocsik, A.; Kincses, A.; Tubak, V.; Jósvay, K.; Zvara, Á.; Campos-Bedolla, P.; Deli, M. A. Simvastatin, Edaravone and Dexamethasone Protect Against Kainate-Induced Brain Endothelial Cell Damage. *Fluids Barriers CNS* **2020**, *17*, 5.

(46) Aekbote, B. L.; Fekete, T.; Jacak, J.; Vizsnyiczai, G.; Ormos, P.; Kelemen, L. Surface-Modified Complex SU-8 Microstructures for Indirect Optical Manipulation of Single Cells. *Biomed. Opt. Express.* **2016**, *7*, 45−56.

(47) Hutter, J. L.; Bechhoefer, J. Calibration of atomic-force microscope tips. *Rev. Sci. Instrum.* **1993**, *64*, 1868−1873.

(48) Butt, H.-J.; Jaschke, M. Calculation of Thermal Noise in Atomic Force Microscopy. *Nanotechnology* **1995**, *6*, 1−7.

(49) Florin, E.-L.; Rief, M.; Lehmann, H.; Ludwig, M.; Dornmair, C.; Moy, V. T.; Gaub, H. E. Sensing Specific Molecular Interactions

with the Atomic Force Microscope. *Biosens. Bioelectron.* **1995**, *10*, 895−901.

(50) Riener, C. K.; Stroh, C. M.; Ebner, A.; Klampfl, C.; Gall, A. A.; Romanin, C.; Lyubchenko, Y. L.; Hinterdorfer, P.; Gruber, H. J. Simple Test System for Single Molecule Recognition Force Microscopy. *Anal. Chem. Acta.* **2003**, *479*, 59−75.

(51) Ebner, A.; Hinterdorfer, P.; Gruber, H. J. Comparison of Different Aminofunctionalization Strategies for Attachment of Single Antibodies to AFM Cantilevers. *Ultramicroscopy* **2007**, *107*, 922−927.

(52) Aekbote, B. L.; Jacak, J.; Schütz, G. J.; Csányi, E.; Szegletes, Z.; Ormos, P.; Kelemen, L. Aminosilane-Based Functionalization of Two-Photon Polymerized 3D SU-8 Microstructures. *Eur. Polym. J.* **2012**, *48*, 1745−1754.

(53) Ebner, A.; Wildling, L.; Zhu, R.; Rankl, C.; Haselgrübler, T.; Hinterdorfer, P.; Gruber, H. J. Functionalization of Probe Tips and Supports for Single-Molecule Recognition Force Microscopy. In *STM and AFM Studies on (Bio)molecular Systems: Unravelling the Nanoworld*; Samorì, P., Ed.; Springer: Berlin, Heidelberg, 2008; pp 29−76.

(54) Wildling, L.; Unterauer, B.; Zhu, R.; Rupprecht, A.; Haselgrübler, T.; Rankl, C.; Ebner, A.; Vater, D.; Pollheimer, P.; Pohl, E. E.; Hinterdorfer, P.; Gruber, H. J. Linking of Sensor Molecules with Amino Groups to Amino-Functionalized AFM Tips. *Bioconjugate Chem.* **2011**, *22*, 1239−1248.